Self-assembled Nanomaterials for Chemotherapeutic Applications

DISSERTATION

Presented in Partial Fulfillment of the Requirements for the Degree Doctor of Philosophy in the Graduate School of The Ohio State University

By

Aileen Shieh

Graduate Program in Chemistry

The Ohio State University

2016

Dissertation Committee:

Professor Dr. Jonathan R. Parquette, Advisor

Professor Dr. Jovica Badjic

Professor Dr. Thomas J. Magliery

Abstract

The self-assembly of short designed peptides into functional nanostructures is becoming a growing interest in a wide range of fields from optoelectronic devices to nanobiotechnology. In the medical field, self-assembled peptides have especially attracted attention with several of its attractive features for applications in drug delivery, tissue regeneration, biological engineering as well as cosmetic industry and also the antibiotics field.

We here describe the self-assembly of peptide conjugated with organic chromophore to successfully deliver sequence independent micro RNAs into human non-small cell lung cancer cell lines. The nanofiber used as the delivery vehicle is completely non-toxic and biodegradable, and exhibit enhanced permeability effect for targeting malignant tumors. The transfection efficiency with nanofiber as the delivery vehicle is comparable to that of the commercially available RNAiMAX lipofectamine while the toxicity is significantly lower.

We also conjugated the peptide sequence with camptothecin (CPT) and observed the self-assembly of nanotubes for chemotherapeutic applications. The peptide scaffold is non-toxic and biodegradable, and drug loading of CPT is high, which minimizes the issue of systemic toxicity caused by extensive burden from the elimination of drug carriers. In addition, the peptide assembly drastically increases the solubility and stability of CPT under physiological conditions in vitro, while active CPT is gradually released from the

peptide chain under the slight acidic tumor cell environment. Cytotoxicity results on human colorectal cancer cells and non-small cell lung cancer cell lines display promising anti-cancer properties compared to the parental CPT drug, which cannot be used clinically due to its poor solubility and lack of stability in physiological conditions. Moreover, the peptide sequence conjugated with 5-fluorouracil formed a hydrogel with promising topical chemotherapeutic applications that also display increased stability and controlled release of the active drug in vitro.

Acknowledgments

I would like to express my appreciation and special thanks to my advisor, Professor Dr. Jonathan Parquette. You have been a tremendous mentor for me, and have encouraged me through the adversities of my research career. I would never have made it this far without your encouragement and kindness. I would also like to thank my committee members Professor Dr. Jovica Badjic and Professor Dr. Thomas Magliery, for taking the time to serve on both my candidacy and final defense examination.

I would especially like to thank collaborator Dr. Hui-Lung Sun for providing advice and guidance with my biological experiments, without your help, I would still be fiddling with commercial protocols today.

To all my friends and colleagues who have had to listen to my unending vents all these years, thank you.

Last but not least, I cannot begin to express how grateful I am to my parents for all the sacrifices you have made on my behalf, and the unconditional love and support you have given me while I strive towards my goal.

Vita

2006 .....Affiliated Senior High School of Normal Taiwan University

2010.....B.S. Biochemistry, Ohio State University

2010 to present .....Ph.D. Candidate, Department of Chemistry & Biochemistry, The Ohio State University

Publications

[1] Sun, Y., Kaplan, J. A., Shieh, A., Sun, H. L., Croce, C. M., Grinstaff, M. W., and Parquette, J. R. (**2016)** Self-assembly of a 5-fluorouracil-dipeptide hydrogel, *Chem Commun* 52, 5254-5257.

[2] Sun, Y., Shieh, A., Kim, S. H., King, S., Kim, A., Sun, H. L., Croce, C. M., and Parquette, J. R. (**2016**) The self-assembly of a camptothecin-lysine nanotube, *Bioorg. Med. Chem. Lett.* 26, 2834-2838.

[3] Kim, S. H., Kaplan, J. A., Sun, Y., Shieh, A., Sun, H. L., Croce, C. M., Grinstaff, M. W., and Parquette, J. R. (**2015**) The self-assembly of anticancer camptothecin-dipeptide nanotubes: a minimalistic and high drug loading approach to increased efficacy, *Chemistry* 21, 101-105.

Fields of Study

Major Field: Chemistry

Table of Contents

List of Figures

Chapter 1: Assisted miRNA Delivery in Lung Cancer

Background

The Central Dogma was a term enunciated by Francis Crick in 1958, and for decades the transfer of genetic information from DNA to RNA and from RNA to protein has been the central keystone of molecular biology (**Figure 1**).[1] RNA in the Central Dogma is more accurately referred to as messenger RNA (mRNA), or coding RNA, with the information necessary for the translation of protein.

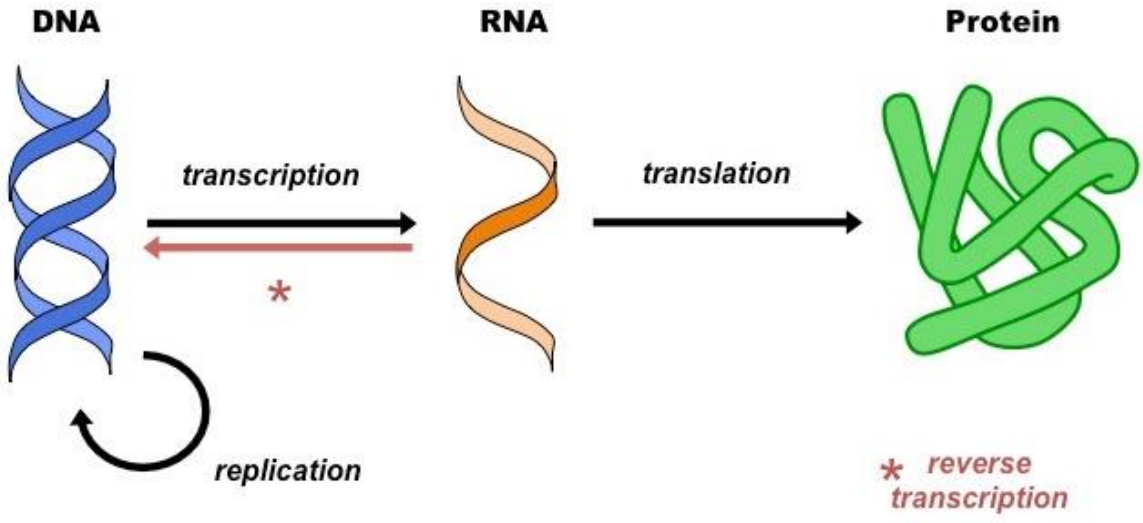

Figure 1. The Central Dogma of Molecular Biology.

In 1997, the discovery of introns, which are segment of the RNA that are transcribed from DNA but do not serve the function of coding protein, was a big surprise in the history of molecular biology, as it was not expected at the time that the genes of higher organisms would be consist of both coding and non-coding sequences.[2-4] However, introns, or non-coding RNA, were dismissed at the time of discovery as genomic debris, and assumed to simply be degraded once transcribed.[5] A few years later, roles of RNA other than translating protein began to emerge and very quickly there was increasing evidence that catalytic RNA existed in both animals and plants, in introns and elsewhere, and play a variety of roles crucial in the survival of organisms, including post-transcriptional regulation of mRNA.[6-8]

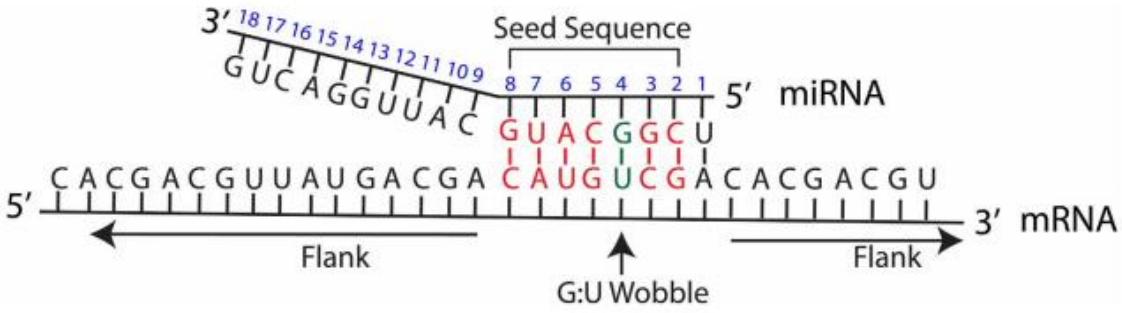

Figure 2. Schematic overview of miRNA and mRNA target interaction with miRNA 'seed' region. miRNA position shown in blue and seed sequence is 2-8 nucleotides from 5' end. Flank refers to the mRNA sequence on either side of the region corresponding to the miRNA seed sequence.[9]

In 1993, Ambros and colleagues reported the first evidence of small regulatory RNAs of ~22 nucleotides, *lin-4* and *let-7,* that were responsible for regulating the timing of *Caenorhabditis elegans* development.[10, 11] These microRNAs (miRNAs) were thought of at that time to be exclusive to nematodes, but *let-7* was soon discovered to be conserved in humans too.[12] Conservation across species imply that a sequence has been maintained by evolution despite mutation and speciation; in molecular biology, conservation of sequence is a good indication for function.[13] It also became evident that miRNAs are involved in nearly all developmental and pathological regulations, and that many, if not most, protein-coding mRNAs are targets for miRNA regulation.[14, 15] In addition, a single miRNA can regulate large numbers of mRNAs, and mRNAs often contain multiple target sites for miRNAs in their 3' untranslated region (3'UTR).[16, 17] A major reason a miRNA is capable of large numbers of mRNA targets is because miRNA only needs to be partially complementary to its target. The target recognition site between miRNA and mRNA typically occurs at the 3' untranslated region (3'UTR) of the mRNA and the seed region (nucleotides 2-8 from the 5' end) of the miRNA (**Figure 2**).

miRNA biogenesis is extremely diverse and has previously been extensively studied and reviewed[18, 19]; however, due to the exact reason of its diversity the complete mechanism and its function *in vivo* is yet to be fully delineated. The rest of this chapter is devoted to discussing the assisted delivery of miRNA in humans, therefore, the rest of the background would be dedicated to briefly discussing the known biogenesis of miRNA pertaining to the subject of interest.

The biogenesis of miRNA (**Figure 3**) is under tight temporal and spatial regulation, and abnormalities in regulation often lead to many human diseases. Following transcription in the nucleus, miRNA precursor, pri-miRNA (primary miRNA), consisting of an imperfectly paired stem with a terminal loop is excised by enzyme Drosha. Drosha is a member of the RNase III enzyme family and it excises the stem-loop of pri-miRNA to form pre-miRNA (precursor miRNA).[20] The pre-miRNA in animals is exported from the nucleus by Exportin5 (EXP5) to the cytosol before the terminal loop is excised by Dicer enzyme to create a mature miRNA duplex of approximately 19-22 base pairs in length.[20] Mature miRNA duplex then combines with Argonaute (Ago) protein to form the RNA-induced silencing complex (RSIC). Within the complex, the mature miRNA duplex is rapidly unwound, and one of the strands is retained while the other one is lost. The mechanism for selecting the retained strand is not yet fully understood, but it has been suggested that the selection is based on the relative thermodynamic stability of the duplex's ends. The less stable the 5' terminus of the strand the more likely it is to be retained.[21] This rule, however, is not absolute and exceptions are frequently observed[22]. Nomenclature-wise, the more commonly associated strand is called the guide strand, or simply the miRNA strand, while the other strand is designated the passenger strand, or the miRNA* strand. Either strand can form stable complexes with Ago proteins. The RISC complex is led by the miRNA as an adaptor to specifically recognize and regulate particular mRNAs. The recognition between miRISC to mRNA usually occurs in the 3'UTR region, although exceptions exist[23]. The silencing mechanism of miRNA occurs through multiple mechanisms, including mRNA degradation, translational repression,

inhibition of translation, co-translational protein degradation, and premature termination of translation[24-27]. The degree of miRNA to mRNA complementarity in the seed region has been considered a key element in determining the regulatory mechanism. In general, high levels of complementarity between miRISC and mRNA often leads to the endonucleolytic cleavage and subsequent degradation of mRNA by the DICER in the RISC complex, while lesser complementarity leads to regulatory inhibition.[28]

The term RNA interference (RNAi) refers to the process in which RNA interferes with the expression of genes and regulates the corresponding proteins through gene silencing mechanism, and the study of RNAi has been widely applied to the study of cancer therapy. In fact, since its discovery in 1998, RNAi has revolutionized basic and clinical research.[29] In 2004, just six years after the discovery of RNAi, the first clinical trial of small-interfering RNA (siRNA) was initiated, and in 2013, the first miRNA clinical trial was initiated.[30] Now in 2016, more than 20 RNAi-based therapeutics are currently in clinical trials, and several of these are Phase III trials.[31]

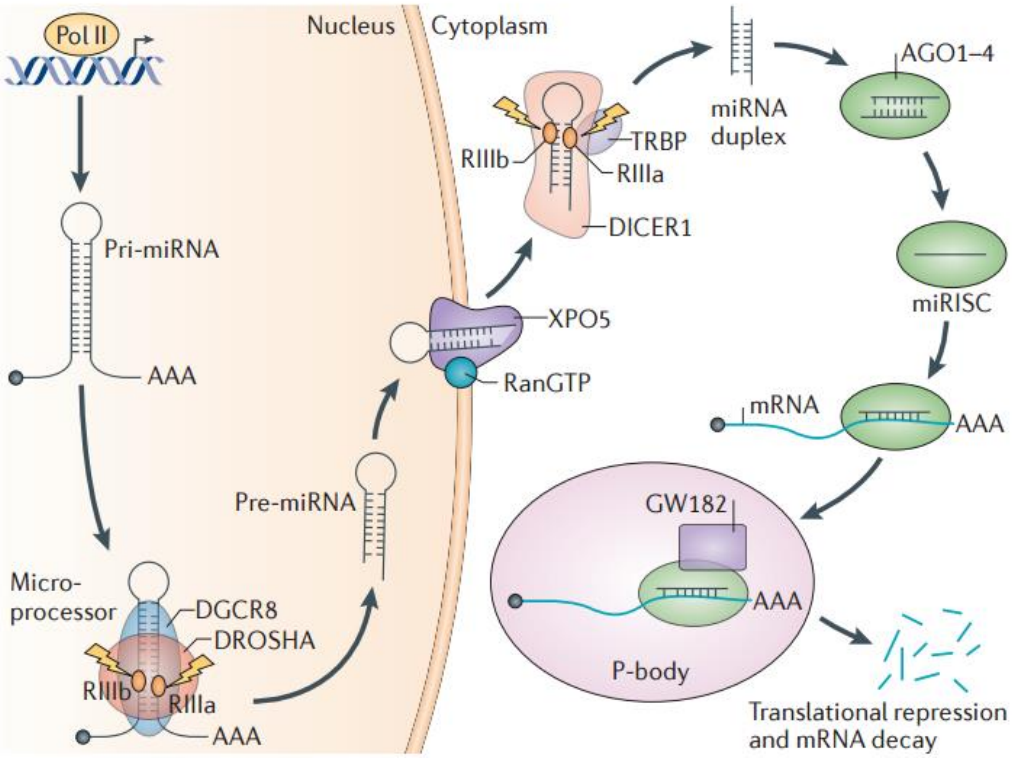

Figure 3. Overview of miRNA biogenesis pathway. miRNA genes are transcribed as primary miRNAs (pri-miRNAs) by RNA polymerase II (Pol II) in the nucleus. The long pri-miRNAs are cleaved by processors including DROSHA and others to produce precursor miRNAs (pre-miRNAs) that are about 60-70 nucleotides long. The pre-miRNAs are then exported out of the nucleus and into the cytoplasm by exportin 5 (XPO5). In the cytoplasm, DICER1, a ribonuclease III enzyme, excises off the end loop of the pre-miRNA and produces the mature miRNA duplex, which then complements with Argonaute (AGO) protein to form the miRISC complex. The complex is led by the guide strand of the miRNA to target mRNA by sequence complementary binding and mediates gene suppression by targeted mRNA degradation and translational repression in processing bodies (P-bodies).[32]

Chapter 1.1: Nanofiber Assisted miRNA Delivery into Lung Cancer Cells

Introduction

In 2012 there were 14 million new cancer cases and 8.2 million cancer-related deaths worldwide. In the United States, that number translates to about 1,685,210 new cancer cases and about 569,490 cancer deaths in 2016 according to an estimation made by National Cancer Institute[33]. The major treatment for localized and metastasized cancer is chemotherapy, either with or without combination with other forms of therapy. However, despite recent advances in the diagnostics and treatment of cancer, it is still a leading cause of death around the world. Conventional therapy suffers limitations such as lack of tumor selectivity, poor aqueous solubility, and acquired drug resistance[34]. Nanotherapeutics is the application of nanotechnology in medicine that is rapidly progressing to address several limitations of conventional drug delivery system, and although the field is relatively new, it has found many applications in cancer biology and made a broad impact on healthcare.[35, 36]

Nanotherapeutics is a multidisciplinary field that takes advantage of the nanomaterial's unique properties to ultimately increase patient outcome and quality of life, many examples such as liposomal aggregates, protein nanoparticles, polymer-drug conjugates and inorganic nanoparticles have been extensively studied for clinical translation.[37] More recently, nucleic acid therapeutics such as gene therapy agents and RNA interference has also been gaining popularity.[37-39] RNA interference (RNAi) is a mechanism for gene silencing by promoting the degradation of messenger RNA

(mRNA), and such mechanism possess the ability in targeting cancer-related genes via small interfering RNAs (siRNAs) and microRNAs (miRNAs).[40, 41]

Compared with conventional small molecule therapeutics, siRNAs and miRNAs offer versatility as they can be designed to affect any gene of interest; they also have the ability to target "non-druggable" targets. For example, some disease-related proteins lack an enzymatic function or have a conformation not accessible to conventional drugs or small molecule compounds, have been successfully targeted by RNAi approach *in vivo.*[42-44]

Clinical trials of siRNA and miRNA-based therapy have already been initiated, and although siRNA and miRNA share many similarities in terms of length (19-22 nucleotides) and physiochemical properties, the most unwavering distinction between miRNA and siRNA has been whether or not they silence their own expression.[24] Almost all siRNA silence the same locus from which they were derived, and their capacity to strike at their encoding DNA and RNA makes their production a constant struggle against themselves. siRNA requires complete complementarity between the target and itself, making it highly specific to just one target. siRNA is often considered as a defender of genome integrity in response to foreign or invasive nucleic acid such as viruses, transposons, and transgenes.[45] In contrast, most miRNA do not silence their own loci but silence other genes, and a single miRNA can regulate large numbers of mRNAs, and mRNAs often contain multiple target sites for miRNAs in their 3' untranslated region.[16, 17] miRNA also requires partial complementarity to its target, just a few nucleotides in the 2-8 nucleotide "seed region" in the 5' end of the miRNA is required for its target

recognition. Since miRNA can regulate multiple cancer-related genes simultaneously, using miRNA as a therapeutic approach plays an important role in discovering novel cancer treatment and will be the focus for the rest of the report.

It is now clear that non-coding RNAs provide important opportunities for development of future genetic based therapeutics through the phenomenon of RNA interference, which is the ability to target disease-related genes and silence gene expression after the introduction of sense-antisense RNA pairs. [40, 41] miRNAs have been shown to regulate many physiological development and disease processes, and because of their crucial role in regulation, abnormalities with the expression of miRNA often contribute to pathogenesis of most, perhaps all, human malignancies such as cancer[46] and many other diseases,[47] including pluripotency,[48] epithelial-mesenchymal transition and metastasis,[49] diabetes,[50] and neural plasticity and memory.[51]

miRNA-based cancer-therapy possess several difficulties. Naked miRNA is unable to pass through cell membranes and are also rapidly degraded by ubiquitous nucleases present in nature, in fact, small RNA molecules such as siRNA and miRNA have a half-life of less than one hour in serum.[52-54] The rise of targeted miRNA delivery through nano-carriers to achieve specific, efficient and safe systemic delivery is crucial in miRNA-based therapy. Ideally, the carrier should be non-toxic, targets tumor and protects RNA before it reaches target.[55]

Delivery systems is currently and will continue to be the key to bring miRNA therapy into the clinic. Systemic delivery is an attractive option, because it provides access to all tissues irrigated by blood vessels through simple administration (oral or

intravenous).[56] However, systemic delivery is set back from poor biodistribution and other challenges *in vivo,* such as passing through the cell membrane and reaching the cytoplasm of target cells. Both viral and non-viral carriers are implemented to overcome the hurdles in targeting tumor cells and cellular penetration. With viral vectors such as lentiviruses, adenoviruses, and adeno-associated viruses, miRNA can be delivered to cell nuclei for function.[57-59] However, compared with viral carriers, synthetic nanoparticle vehicles possess considerable advantage due to their less toxic nature, simple manufacturing, modification and analysis, lower immunogenicity and tolerance for size of cargo.[60-62] Non-viral delivery methods that have been extensively studied include cationic[63] and neutral liposomes,[64] polyethyleneimines,[65] and atelocollagens.[66] Cationic liposomal carriers can interact and counterbalance the negatively charged nucleic acids, resulting in slight net positive charge complexes that facilitates cellular uptake, protect miRNA from degradation by serum nucleases and increase circulation half-life when systemically delivered.[67] However, positively charged carriers have been reported to have several negative consequences upon administration *in vivo*, including interferon responses and dose-dependent toxicity, etc.[67, 68] Neutral liposomes were developed to overcome these side-effects, and have been reported to show enhanced accumulation of miRNA in tumors without the adverse effects associated with cationic lipid carriers.[64, 69]

Drug targeting strategies have frequently been divided into two categories, “active” and “passive”.[70] Active targeting is used to describe specific interactions between an attachment on the drug/drug carrier, usually an antibody or carrier protein or a ligand, and

the target cell membrane with the receptor for the attachment.[70] Active targeting is also called ligand based targeting since it is usually employed through specific ligand receptor interactions. In order to achieve high specificity, the receptors should be highly expressed on target/tumor cells, but not on normal healthy cells.[70, 71] One of the two qualities important for the active targeting system is the specificity with which the ligand recognizes the receptors and the other is the capacity to deliver the required dose of drug for the required period of time.[70, 71] With active targeting the drug is concentrated in the tissue of interest while the amount of drug taken up by the remaining tissues should be minimized, which would improve efficacy and reduce side effects. However, this strategy has two associated problems, one is that tumors tend to shed antigens which would circulate and the delivery system would attach to these widely dispersed antigen molecules, the other problem is that the antigens may not be expressed homogenously, which would decrease antibody-antigen specificity.[70] It is also important to note that due to the antibody-antigen specificity, the drug/drug carrier is designed specifically to recognize one target, therefore, due to the mutable nature of cancer cells, it is relatively easy for the target cells to mutate and gain resistance to the treatment.[72] In accordance with these drawbacks, studies have also shown that the presence of the tumor-targeting ligand do not always result in increased accumulation of the drug/drug carrier in target tumors, suggesting that "active targeting" does not automatically translate into effective and efficient delivery into target tumor cells.[73-75]

Passive targeting, on the other hand, takes advantage of the intrinsic physiochemical properties of the drug carrier complex, such as the size and charge of the

complex, so that it escapes the body defense system and accumulates in the target tumor areas with leaky vasculature; commonly referred to as enhanced permeation and retention (EPR) effect.[70] EPR effect is attributed to the unique vascular characteristics of tumor tissue and the lack of an effective lymphatic drainage system in the solid tumors.[76] Since passive targeting is the result of the physical properties of the tumor and the drug carrier complex, drug resistance is not as easily induced as compared with active targeting. In addition, clinically speaking, tumors are classified as a conglomerate of cells with multiple histological and genetic profiling, which means cell membrane expression levels of ligands and other proteins would be different throughout the tumor; in which case passive targeting would be a more viable practice than active targeting.[77] In light of these considerations, we employ passive targeting strategies in our drug-carrier molecule design.

Results and Discussion

In this study, we report non-toxic, biodegradable peptide vehicles for sequence independent miRNA targeted delivery into lung cancer cells. The tetra-peptides conjugated with coumarin, Fmoc-KFKK(DAC)-NH_2 (**K**) and Fmoc-EFEK(DAC)-NH_2 (**E**) (**Figure 4**) , self-assembles into nanofibers with diameters in the 30-60nm range in PBS (pH7.4) (**Figure 5**). The mechanism of self-assembly has previously been reviewed,[78] in short, the coumarin and Fmoc group in these peptides drive self-assembly via hydrophobic effects and π-π stacking interactions, while lysine and glutamic acid provide enough electrostatic repulsion to prevent non-specific aggregate of the compounds.

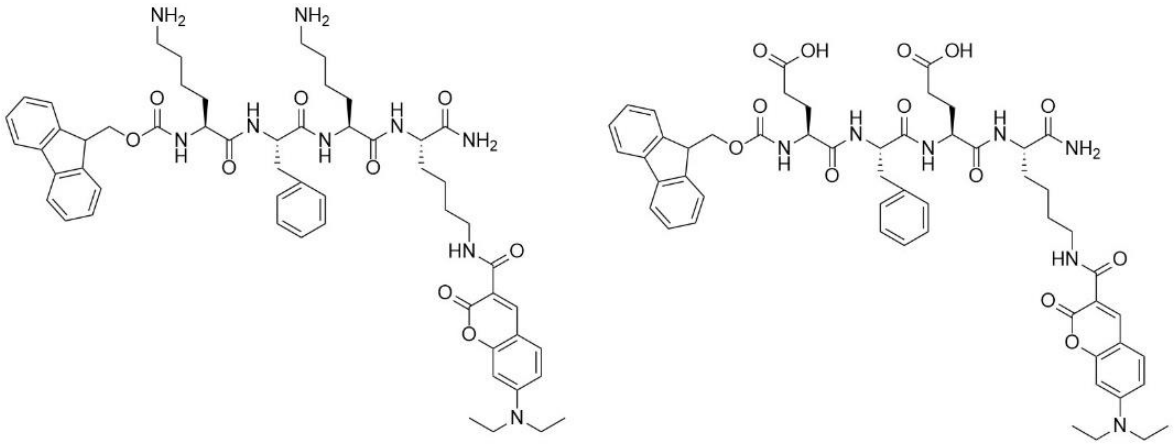

Figure 4. Structural design of compounds **K** (left, side chains positively charged at physiological pH) and **E** (right, side chains negatively charged at physiological pH).

Binding Efficiency of miRNA with K and E

The binding efficiency between peptide carrier and miRNA were studied using ethidium bromide agarose gel and the locality of miRNA on the nanofiber was visualized with transmission electron microscopy (TEM). It should be noted that the interaction between miRNA and the carrier is mainly based on electrostatic interaction; given that miRNA is negatively charged, positively charged **K** has a much better binding efficiency as compared with negatively charged **E** (**Figure 6**). In addition, the amount of miRNA bound to nanofibers is also miRNA concentration dependent during the process where miRNA and nanofibers are mixed together for binding to occur (data not shown).

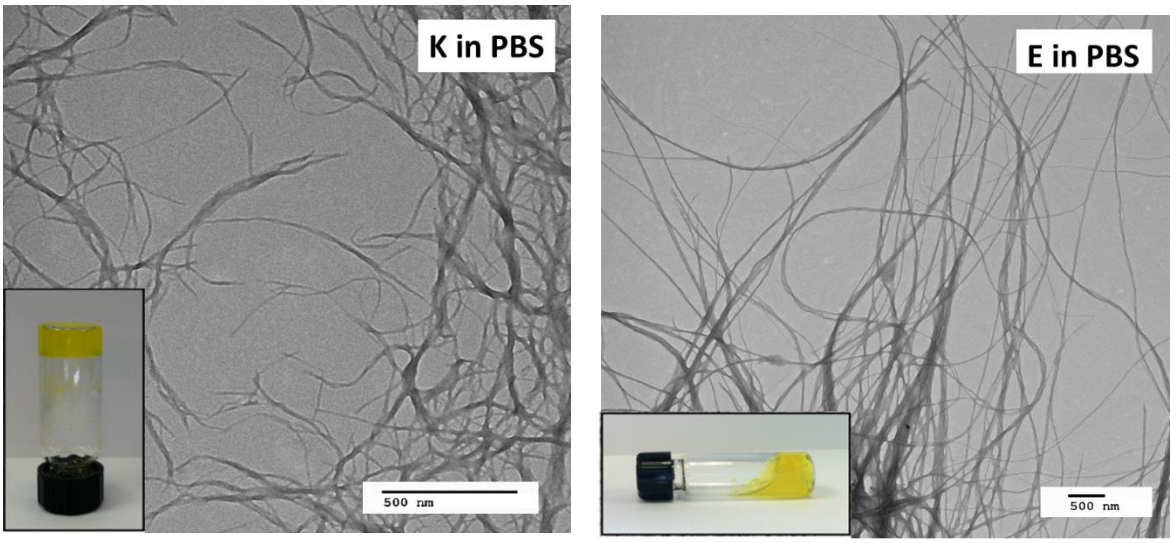

Figure 5. TEM images of **K** (left) and **E** (right) in PBS at pH 7.4. Samples prepared by aging the compounds at 10mM for 16 h at pH 7.4 and 24°C, then diluting to 0.5mM prior to imaging with Technai G2 Spirit instrument at 80 kV. Sample was applied to copper grid for 2 mins and negative stained with 2% wt uranyl acetate for 1 min.

K and **E** were previously aged at 10mM in sterile PBS (pH7.4) for 16 h at r.t. to allow nanofibers to form, the solution was then diluted and miRNA was added to the solution for binding between the two to occur (0.5mM **K** or **E** with 0.5nmol miRNA either hsa-let-7a or hsa-miR-16). After 4 h of incubation ambient temperature, the solution was ultracentrifuged at 80,000 rpm, and unbound miRNA along with **K** and **E** that did not form nanofibers were expected to remain in solution while nanofibers would pellet at the bottom. The pellet would also include miRNA that was bound to the nanofiber. The pellet was resuspended and the concentration of miRNA bound to nanofibers was determined with Nanodrop (UV at 260 nm), and further experiments were carried out following this separation procedure unless otherwise noted.

Ethidium bromide agarose gel confirms the presence of intact miRNA in the resuspended nanofiber pellet. Negative controls were also carried out with only the nanofibers and only miRNA ultracentrifuged at 80,000 rpm and 'pellets' resuspended. In the case where only miRNA was ultracentrifuged, no pellet was observed but the ultracentrifuge tube was still rinsed with water and run on ethidium bromide agarose gel to confirm the miRNA band observed in other columns were not pseudo positive bands from residual miRNA on the walls of the tube (**Figure 6**).

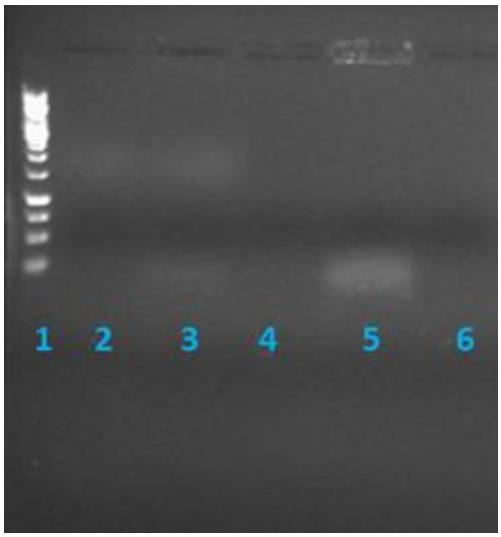

Figure 6. Binding efficiency between **K** and **E** and miRNA were visualized with ethidium bromide gel. **K** has a higher binding efficiency than **E** with let-7a as shown on the gel from left to right 1) 1kb marker; 2) **E**; 3) **E** with let-7a; 4) **K**; 5) **K** with let-7a; 6) negative control with let-7a to show the bands for 2 and 4 were not from residual let-7a on the walls of centrifuge tube.

TEM images of miRNA's interaction with **K** was visualized with hsa-miR-16-biotin (Sigma Aldrich) and streptavidin conjugated colloidal gold (5nm, from Cytodiagnostics).[79] From the images we are able to visualize miRNA binding along the surface of the nanofibers (**Figure 7)**.

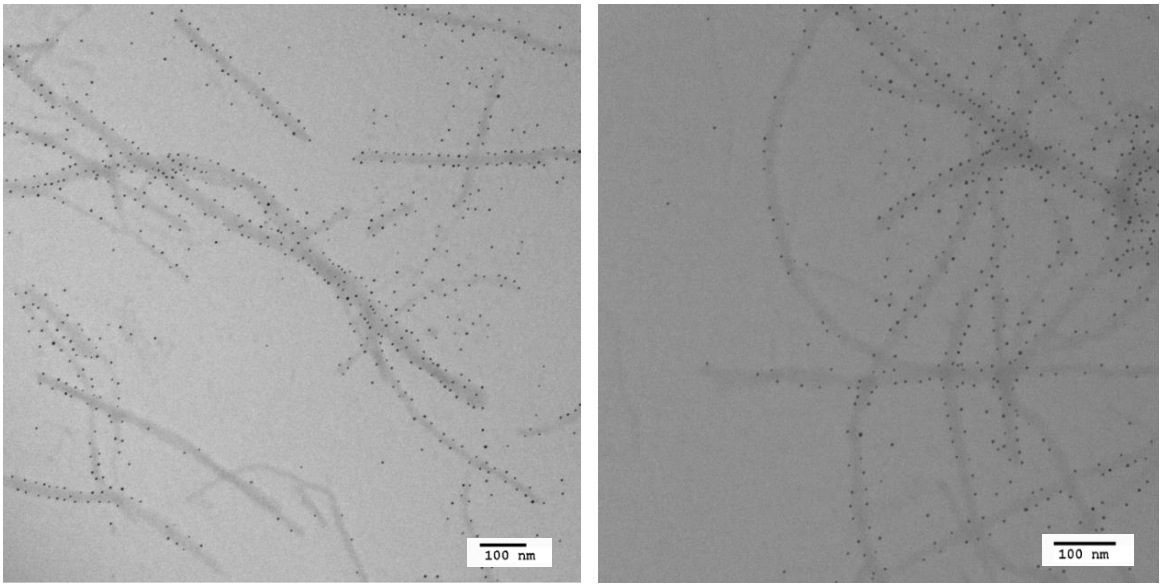

Figure 7. TEM images of hsa-miR-16-biotin binding with **K**, visualized on carbon-coated grid with streptavidin conjugated colloidal gold (5nm). The images show that the miRNA binds along the surface of the fiber, suggesting electrostatic interaction between the two.

Intracellular Uptake and Cytotoxicity of K and E

A major limitation to most conventional anticancer chemotherapeutic agents is their lack of selectivity.[80] Nanoscale drug carriers have been exploited to facilitate passive accumulation in tumor via the enhanced permeability and retention (EPR) effect.[81] EPR is the property by which nanomaterials of up to 400nm are able to accumulate effectively and selectively in tumor or inflamed tissue much more than they do in normal tissues.[82, 83] This is a phenomenon caused by the leaky vasculature and the poorly formed lymphatic drainage system accompanied with the rapid growth of

malignant tumors.[84] Although leaky vasculatures as large as 2000nm has been report between adjacent endothelial cells[85], molecules that are too large may also have trouble passing through blood capillaries. EPR was a phenomenon noticed as early as 1986[86] and documented in humans during a clinical trial carried out in Israel from 1991 to 1994 for DOXIL, a liposomal doxorubicin conjugate.[87] We hypothesize our nanofibers would be selective towards tumors through EPR effect due to the size of **K** and **E**, which exceeds the lower size limit on delivery vehicle to escape the 10nm diameter threshold for first-pass elimination by the kidney.[88]

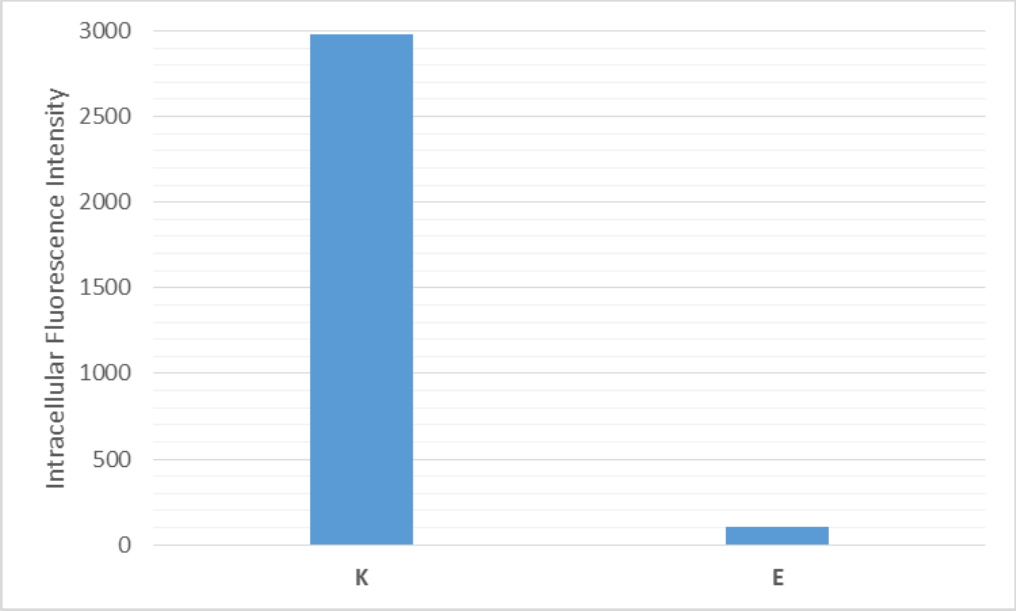

Figure 8. Flow cytometric analysis of **K** and **E** in A549 (NSCLC) showing intracellular accumulation of **K** significantly greater than that of **E**, by roughly 30 fold after 4 h incubation at 30 μM. Cells were resuspended in HBSS and kept on ice before subjected to flow cytometer (BD FACS Aria III), excitation wavelength = 355 nm and emission wavelength detected at 425-475 nm. Bifurcated gate was used on the control untreated cells population to calculate statistics above threshold values as fluorescence intensity (uptake).

Passive targeting is in essence the result of physiochemical properties of the carrier-drug conjugate, in addition to EPR effect, the charge of the conjugate is also essential in determining the uptake efficiency into cancer cells.[88] It has been shown that positively charged molecules exhibit greater uptake by cells than that of a neutral or

negatively charged molecule.[89] We performed flow cytometry and confirmed our positively charged compound **K** has an uptake greater than negatively charged **E** by roughly 30 fold (**Figure 8**). In addition, although neither compounds displayed toxicity in normal experimental conditions used in this report (~2-15 nM, 48-36 h), when we greatly exaggerated the concentrations and incubation time (30 μM, 96 h), **E** showed a 70% survival rate while **K** had a >90% survival rate (**Figure 9**).

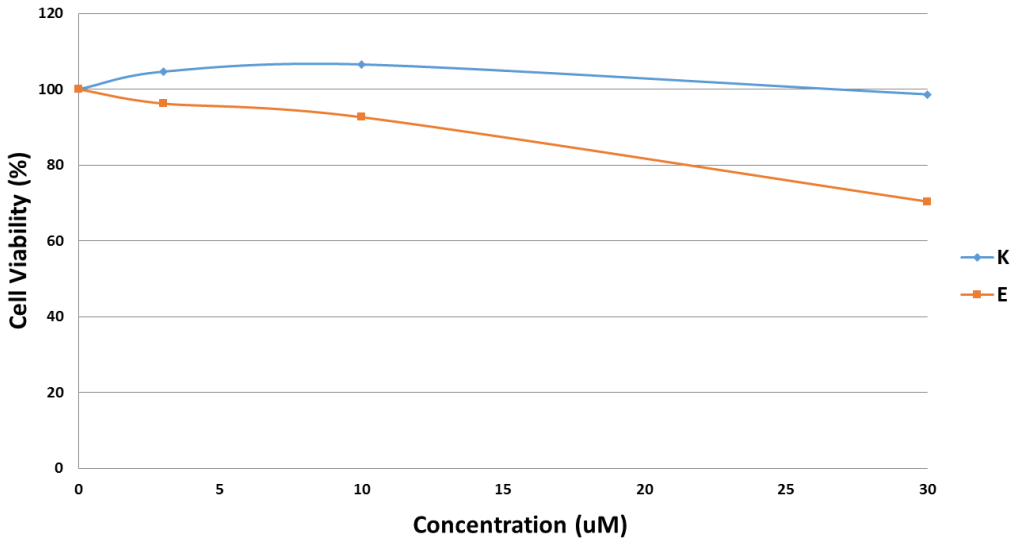

Figure 9. Cytotoxicity analysis with MTT assays of **K** and **E** in A549 (NSCLC) showing that both scaffolds are non-toxic carriers even at unrealistically high concentrations at 30 μM and 96 h incubation time where normal experimental conditions are about 100 fold less concentrated and 24-48 h less.

Figure 10 displays intracellular nanofiber distribution of **K** and **E** in A549. The concentration for confocal microscopic analyses was carried out at 200uM and the cells in **E** shows a slight morphology change due to suspected higher toxicity of **E**, while for **K** the cell morphology is still typical for A549 at 200uM.

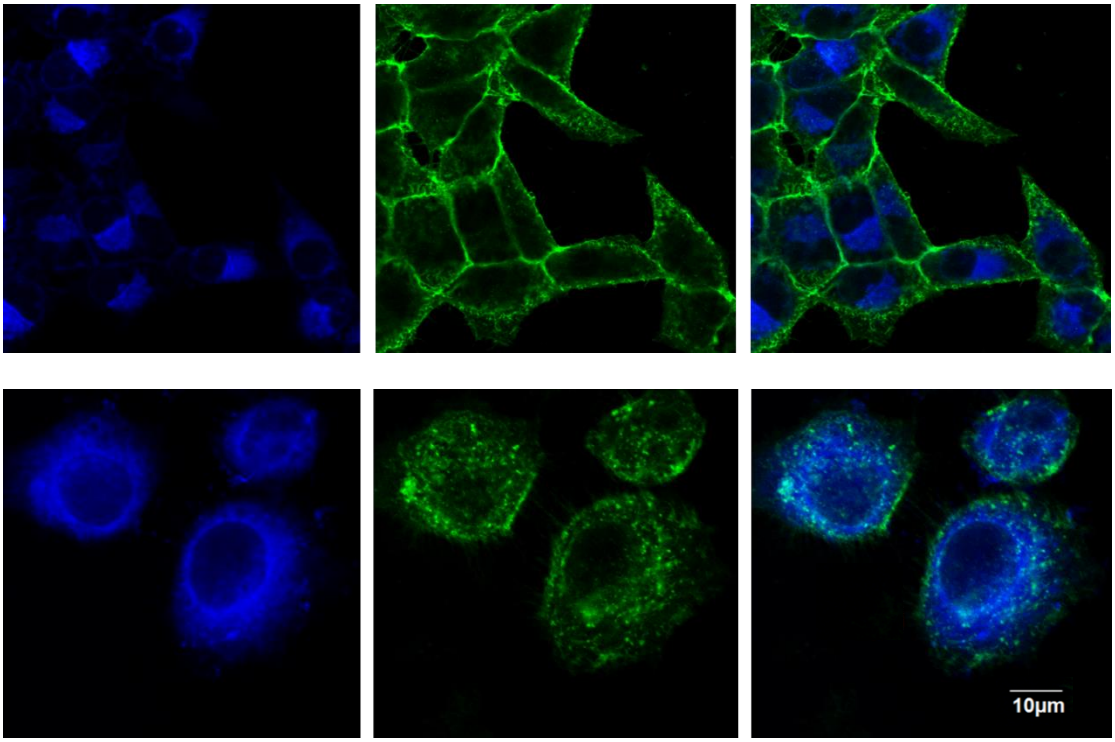

Figure 10. Confocal fluorescence microscopy analyses of the distribution of **K** (top) and **E** (bottom) in A549 shows the accumulation of the carriers in the cytoplasm, but not so much in the nucleus. The carrier is shown in blue (excitation of coumarin at 405nm), and the cell membrane is shown in green (Wheat Germ Agglutinin dye 488nm).

miRNA Delivery Efficiency with K and E

miRNA delivery efficiency was determined by RT-qPCR[90] and visualized using confocal microscopy. Although the binding efficiency between miRNA and **K** is greater than that of **E**, in the qPCR experiments the concentration of miRNA are determined *via* UV and equal amounts of miRNA are added to each experimental conditions for evaluative comparison.

RT-qPCR is to date the most powerful tool to amplify and detect trace amount of miRNA of interest. It is highly sensitive and specific, and also largely reproducible.[91] In this method,[91, 92] the accumulation of miRNA through PCR is detected by fluorescent signal and the Ct (cycle threshold) is defined as the number of cycles of PCR required for the fluorescent signal to cross the threshold. Ct levels are inversely proportional to the amount of target miRNA available in the sample (lower Ct value indicate higher amount of miRNA in sample, and vice versa). Taking the difference between Ct levels for two samples will give relative miRNA abundance levels in the sample. However, the amount of miRNA in a sample is effected by cell abundance, miRNA extraction methods, and other experimental errors. Therefore, the samples are normalized by also quantifying a constantly expressed gene (a reference gene or housekeeping gene) in the cells. The fold change is then expressed as $2^{-\Delta\Delta Ct}$.[92]

The RT-qPCR experiment was carried out in cell line 293T, a popular cell line of choice for many preliminary studies.[93] In our case we are developing a viable new method for transfection, and this cell line is appropriate due to its ease of reproduction and maintenance, and receptiveness to transfection using a wide variety of methods.[93, 94]

The efficiency of let-7a with **K** as the delivery vehicle was 2-3 fold better than our positive control – commercially available RNAiMAX Lipofectamine,[95] while the delivery of let-7a with **E** was negligible and close to our negative control – the cells without any additives. It is important to note that the efficiency of naked let-7a internalization on its own without a vehicle was also comparable to our negative control, suggesting the delivery efficiency observed by other means of carriers is a direct consequence of the delivery capacity of the carriers (**Figure 11**).

Although lipofectamine have been implemented as the go-to reagent for delivery of exogenous DNA/RNA into cells for over two decades, the detail interaction between carrier and cargo and the precise delivery mechanism for this commercially available reagent remain largely elusive.[96, 97] It is widely accepted that lipofectamine takes advantage of its cationic lipid physiological pH that is able to associate with negatively charged miRNA, and the complex enters the cell through endocytotic pathways.[96, 98] Without direct binding with miRNA, although the transfection efficiency is good with lipofectamine, quantitatively the result varies greatly from trial to trial. In addition, lipofectamine exhibits systemic toxicity to cells[99-101] and the reagent must be removed from the cells within 16 h of transfection, or a decrease in cell survival and change in cell morphology is observed. With **K**, direct binding occurs with miRNA, and excess compound **K** which did not form nanofibers and unbound miRNA are removed from solution prior to transfection, ensuring only effective carrier vehicle is present in the solution. As a result the standard deviation between trials for **K** is significantly smaller

than for lipofectamine. **K** is also completely non-toxic to cells at transfection concentrations (**Figure 9**), and does not have to be removed from the culture dish.

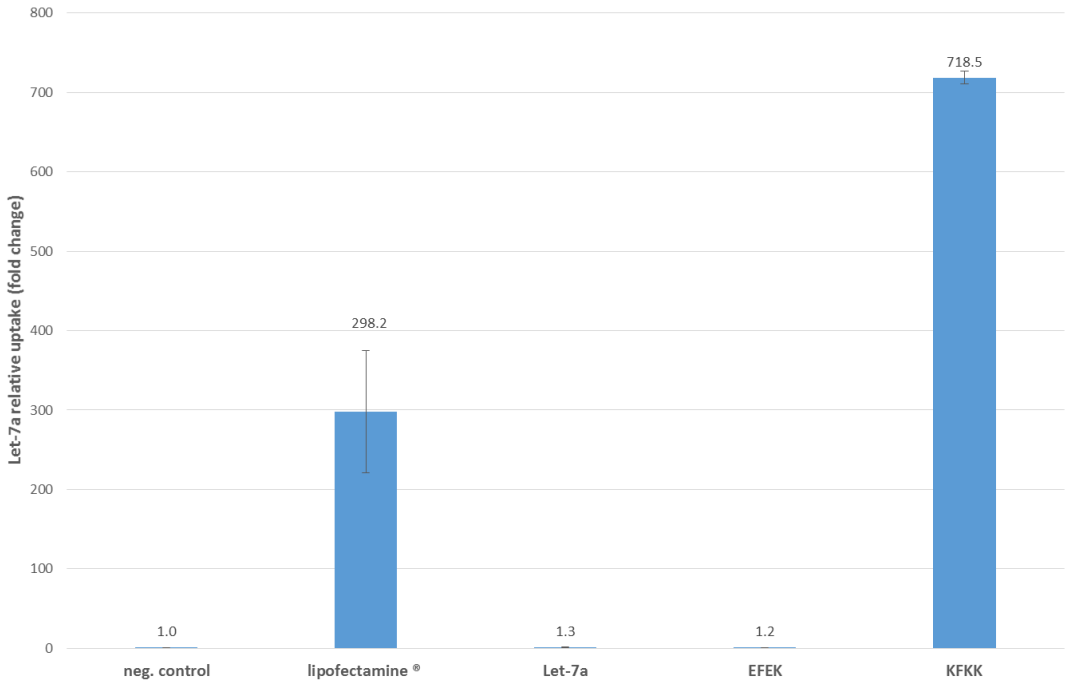

Figure 11. Transfection efficiency in 293T as measured by ΔΔCt qPCR, fold value is displayed and is calculated as $2^{-\Delta\Delta CT}$. The efficiency is higher for **K** than it is for positive control lipofectamine by 2-3 folds, standard deviation (shown as error bars) between trials is also significantly smaller. Negative control (without any additives), let-7a without carrier, and carrier **E** all had around baseline transfection efficiency, suggesting successful transfection is due to the carriers lipofectamine and **K**.

Experiments were also carried out in non-small cell lung cancer (NSCLC) cell lines A549 and H460 (**Figure 12**). In both cases, **K** had a delivery efficiency roughly comparable to that of lipofectamine. In A549 lipofectamine is roughly better than H460 by 1.4 fold, while in H460 both vehicles showed similar transfection efficiency. We attribute the discrepancy in transfection efficiency between cell lines to the fact that there are many factors influencing transfection efficiency such as cell type, cell health and viability, confluency in the culture dish, etc. [102] Carrier **E** along with naked let-7a had negligible delivery capability and comparable with the negative control.

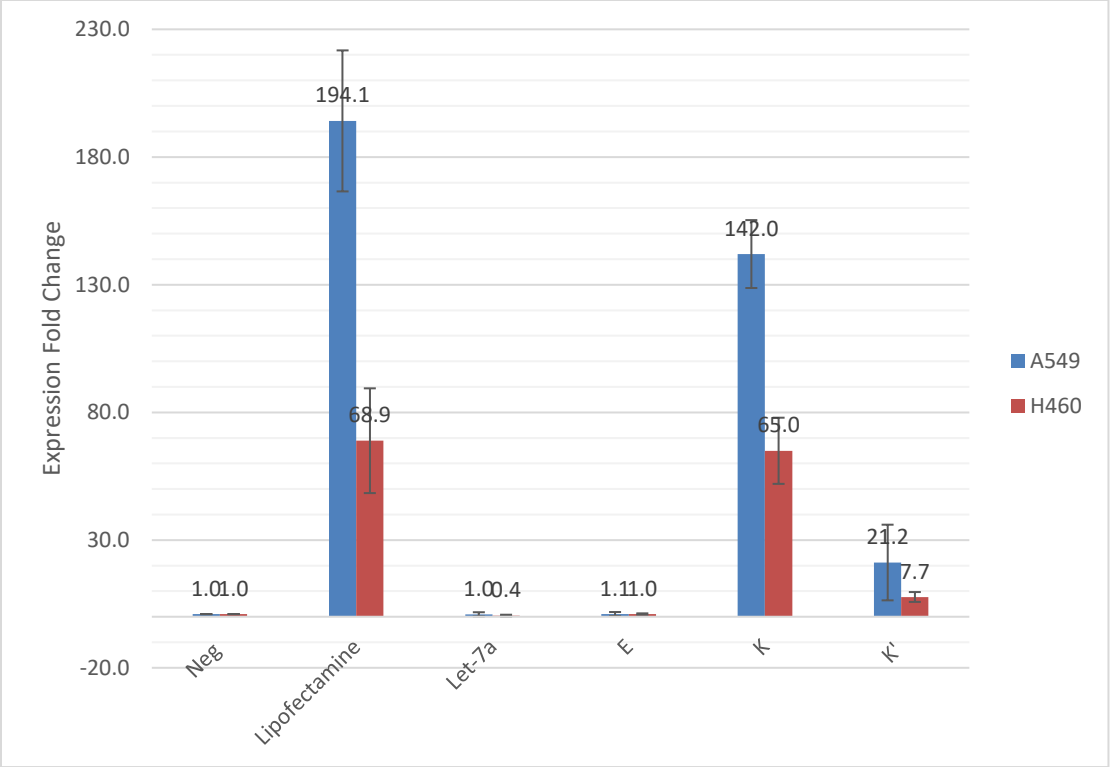

Figure 12. Transfection efficiency in non-small cell lung cancer cell lines A549 (blue) and H460 (orange) using different carrier vehicle show that the efficiency using commercially available lipofectamine and using compound **K** are roughly comparable in both cell lines. **K'** designation indicates no preformation of the nanofibers prior to adding the material and miRNA to the cells. **K'** is roughly 10-15% as effective as **K**, suggesting fully formed nanofiber and fully bound miRNA is crucial in achieving optimal delivery efficiency.

Co-localization of **K** and hsa-mir-16-cy5 as seen in confocal microscopy confirms the notion that **K** assisted miRNA delivery is through direct binding between the two

instead of surfactant effect (**Figure 13)**. In fact, the nanofiber structure must be present in order for **K** to be a successful vehicle for miRNA delivery. During our experimental procedure, the nanofibers were pre-formed prior to binding with miRNA, and the unformed compound and unbound miRNA was removed from the solution. In the case where the unformed and unbound material was included in the transfection procedure, the delivery effectiveness was greatly reduced to about 10-15% of the completely formed and bound carrier-miRNA solution (**Figure 12**). This data suggests miRNA are required to be bound to fully formed nanofibers in order for successful transfection to occur, and that the mechanism of transfection is not through surfactant effect and significantly differs from that of lipofectamine.

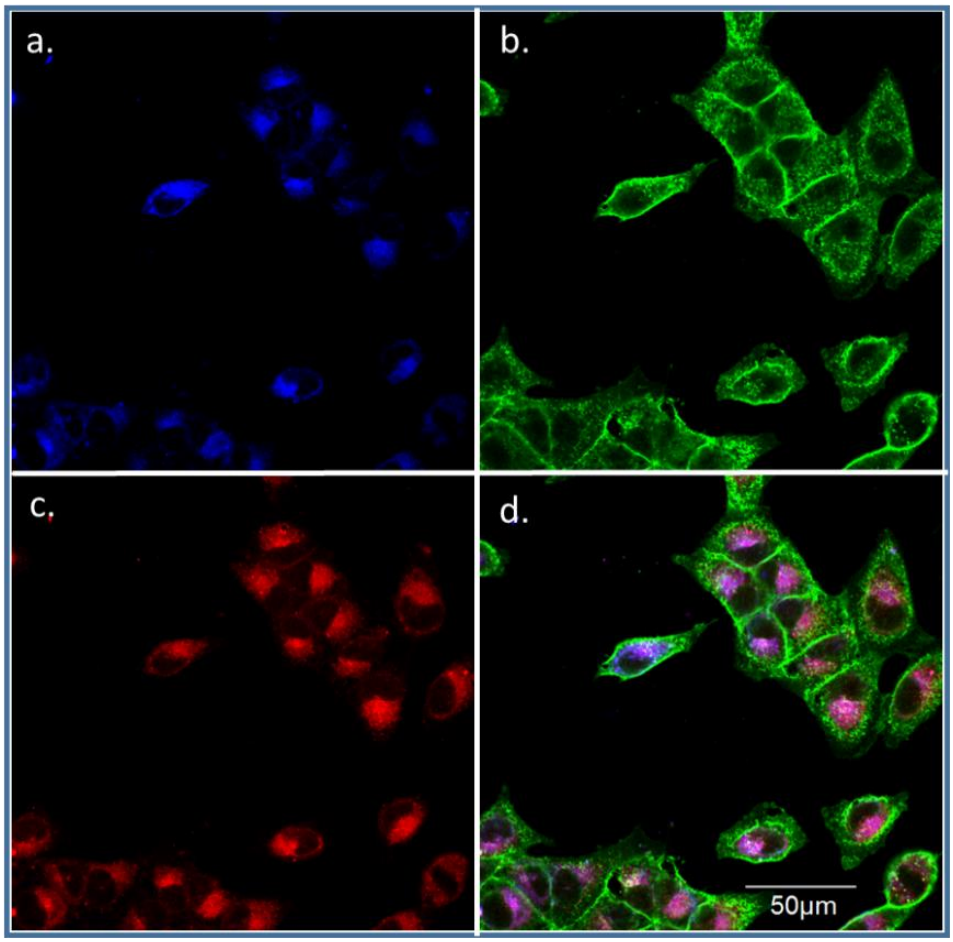

Figure 13. Confocal fluorescence microscopy analysis where a) Compound **K**, coumarin excitation at 405nm, b) membrane dye at 488nm, c) hsa-mir-16-cy5 localization within the cells at 633nm, d) Overlap of a, b, and c showing co-localization of **K** with hsa-mir-16-cy5 in A549, suggesting tight binding between the carrier and the miRNA. .

Hsa-miR-16 Downregulates Target Cyclin E1

Cyclin E1 is a positive regulator of the cell cycle that controls the transition of cells from G1 to S phase, it is also a known downstream target for hsa-miR-16[103, 104]. We built

a stable cell line with an engineered plasmid containing the Cyclin E1 gene sequence and luciferase promoter using A549 (**Figure 14**). When miR-16 targets the Cyclin E1 gene sequence, the luciferase promoter sequence is also silenced and will not be expressed. The luciferase fluorescence can therefore measure any interaction between the miRNA and its downstream target, serving as an indication for miR-16 function after transfection. (**Figure 15**) Using the stable cell line we were able to show that when hsa-miR-16 was delivered with carrier **K**, the target was successfully downregulated by 15%. Although with lipofectamine the downregulation of Cyclin E1 was about 80%, we believe the electrostatic interaction between **K** and miR-16 is strong, and the amount of miR-16 available for downstream target may not be available immediately after transfection. This may provide an opportunity for slow release of miRNA if the pharmacokinetics between **K** and miRNA is better understood *in vivo*. In addition, it should be noted that upon cellular uptake and endosomal escape stage for carrier-miRNA complex, cationic formulations generally have better performance over neutral or anionic formulations,[105] suggesting that the low efficiency observed in the luciferase assay is not the consequence of the inability for carrier-miRNA complex to escape the endosome.

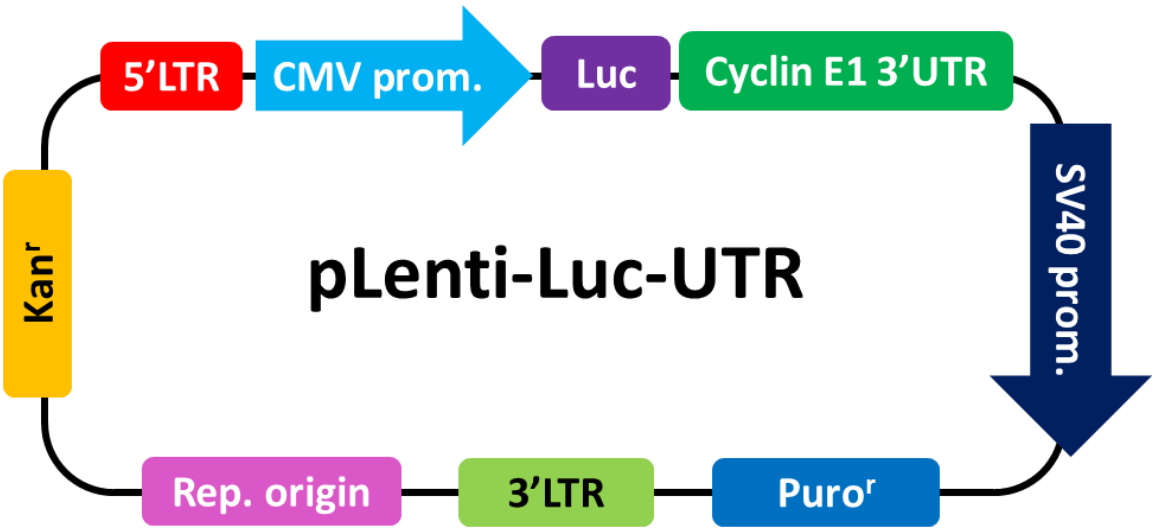

Figure 14. (vector illustration *adapted from amb product website*) Stable Cell Line plasmid design. Luciferase promoter is located in front of miR-16 downstream target Cyclin E1 3'UTR, and so when miR-16 interacts with its target, luciferase expression would be inhibited. The cells expressing the plasmid are puromycin resistant, providing a mean of selection for successfully infected cells.

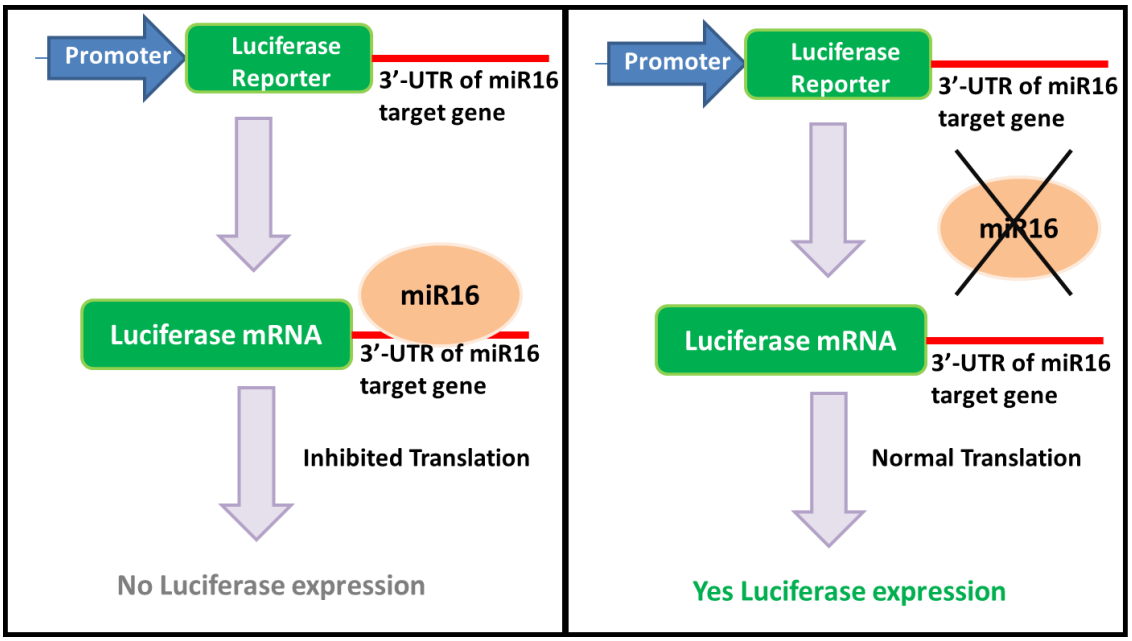

Figure 15. 3'UTR of miR-16 target gene, Cyclin E1, serves as the recognition site. When it interacts with miR-16 (left), the sequence is silenced and the translation of luciferase is inhibited, and results in no luciferase expression for detection. When miR-16 is not present to inhibit the 3'UTR of Cyclin E1 (right), luciferase is expressed normally and luciferase fluorescence is detected.

Materials and Method

Synthesis of DAC-COOH

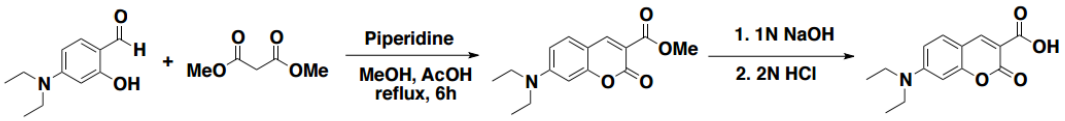

A solution of 4-methoxysalicylaldehyde (193.25 mg, 1 mmol) and dimethyl malonate (158.5 mg, 1.2 mmol) in MeOH (1 mL) was prepared. Piperidine (0.01 mM, 0.1 mmol) with catalytic amount of glacial acetic acid (1 drop) was added to the reaction mixture. After 3 hours reflux, 2 mL H2O was added to the mixture and cooled to 0 °C. 1N NaOH (aq) solution was added to the reaction mixture to form the yellow solid. The reaction mixture was refluxed for 20 min with a vigorous stirring. After cooling down this reaction vessel to r.t., 2N HCl (aq) solution was added in order to acidify the solution. The orange crude solid was collected by a filtration, washed by 50% cold ethanol (10 mL), and recrystallized with ethanol to obtain the bright orange crystalline product. (206 mg, 79 %) 1 H(400 MHz, CDCl3) δ 8.63 (1 H, s), 7.45 (1 H, d, J = 9.0), 6.73 (1 H, s), 6.52 (1 H, s), 3.50 (4 H, q, J = 7.1), 1.27 (7 H, t, J= 7.1); 13C NMR (100 MHz, CDCl3) δ 165.56, 164.52, 158.05, 153.81, 150.26, 131.98, 110.97, 108.55, 105.44, 96.82, 45.37, 12.40; ESI-MS calculated for C14H15NO4 [M+H] + 262.1079, found 262.1042.

Synthesis of Coumarin Compounds K and E

The protected tetrapeptides were manually prepared using Fmoc/t-Bu solid-phase peptide synthesis on rink amide resin (loading 0.59 mmol/g). Amide-coupling steps were accomplished with standard techniques for all amino acids: Fmoc-amino acid, 1,3-diisopropylcarbodiimide (DIC), and 1- hydroxybenzotriazole (HOBt) (300 mol percent each relative to resin) in 1:1 DMF/DCM for 1.5 h. A solution of 20 % piperidine in DMF was used for Fmoc removal and 2% TFA in dichloromethane was used for Mtt group deprotection. The final DAC-tetrapeptide conjugates were cleaved from the resin by the treatment with TFA/water/triethylsilane (95 / 1 / 4) at room temperature for 2 h. The crude peptides were precipitated with cold diethyl ether and purified by reversed-phased HPLC on preparative Varian Dynamax C18 column eluting with a linear gradient of CH3CN/water containing 0.1 % TFA (20/80 to 100/0 over 30 minutes) and stored as lyophilized powders at 4 °C. Peptide purity was assessed by analytical reverse-phase HPLC and identity confirmed using ESI-TOF mass spectrometry and NMR.

Fmoc-KFKK(DAC)-NH2 (K)

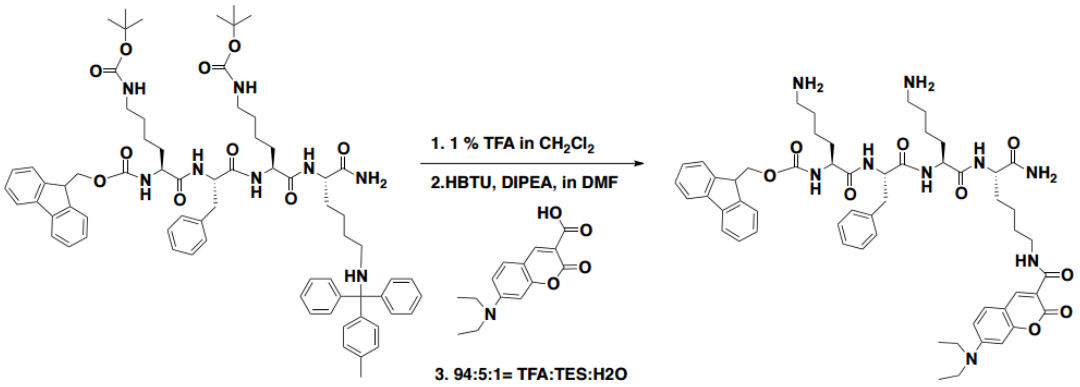

1 H NMR (400 MHz, DMSO-d6) δ 8.95-8.93 (m, 1H), 8.66-8.61 (m, 3H), 8.32-8.30 (m, 1H), 8.19-8.17 (m, 1H), 7.83-7.71 (m, 7H), 7.67 (dd, J = 9.2, 6.3 Hz, 2H), 7.39 (t, J = 0.3 Hz, 1H), 7.27-7.25 (m, 2H), 7.21-7.17 (m, 2H), 7.13- 7.09 (m, 1H), 7.06 (s, 1H), 6.80 (ddd, J = 8.9, 6.3, 2.5 Hz, 2H), 6.60 (dd, J = 11.2, 2.2 Hz, 2H), 4.57-4.45 (m, 2H), 4.27-4.16 (m, 2H), 3.52-3.43 (m, 8H), 3.30-3.25 (m, 2H), 3.10-3.05 (m, 1H), 2.83-2.71 (m, 5H), 1.73-1.65 (m, 3H), 1.61-1.48 (m, 9H), 1.37-1.21 (m, 6H), 1.16-1.09 (m, 11H);).; 13C NMR (100 MHz, DMSO-d6) δ 173.74, 171.38, 171.22, 171.21, 170.66, 162.27, 161.78, 161.71, 157.10, 155.57, 155.17, 152.40, 149. 37, 148.20, 128. 14, 147.64, 147.52, 145.06, 139.33, 137.54, 135.23, 134.24, 131.61, 129.06, 127.97, 95. 76, 95.71, 95. 69, 54.06, 44.34, 38.31, 38. 02, 28. 74, 26.69, 26.53, 24.06, 22.07, 21.83, 12.22; ESI-MS calculated for $C_{56}H_{72}N_9O_9$ [M+H]+ 1014.5453, found 1014.5423.

Fmoc-EFEK(DAC)-NH2 (E)

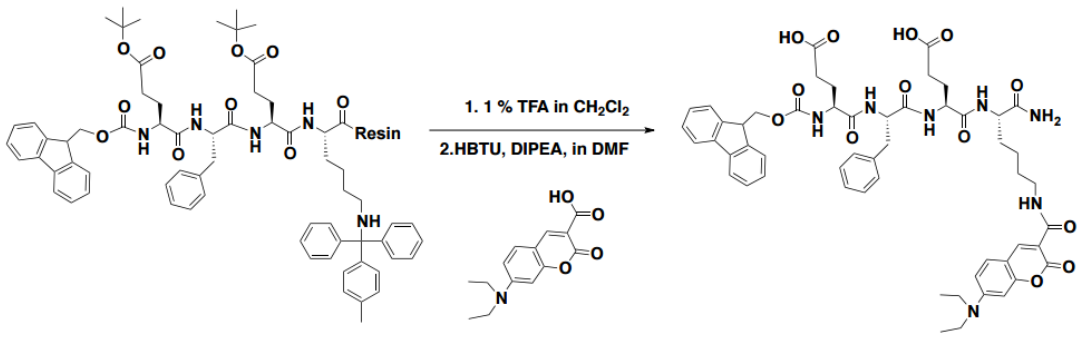

1 H NMR (400 MHz, DMSO-d6) δ 8.64-8.63 (m, 2H), 7.95- 7.93 (m, 1H), 7.89 (d, J = 7.4 Hz, 2H), 7.73-7.70 (m, 2H), 7.66 (d, J = 9.1 Hz, 1H), 7.50 (dd, J = 8.3, 0.3 Hz, 1H),

7.43-7.39 (m, 2H), 7.34-7.30 (m, 3H), 7.23-7.16 (m, 4H), 7.11 (d, J = 0.2 Hz, 1H), 7.01-7.00 (m, 1H), 6.81-6.78 (m, 1H), 6.60 (d, J = 2.2 Hz, 1H), 4.30- 4.18 (m, 5H), 3.50-3.45 (m, 4H), 3.30-3.26 (m, 2H), 2.27-2.24 (m, 2H), 2.18-2.16 (m, 2H), 1.91-1.49 (m, 10H), 1.35-1.30 (m, 4H), 1.26-1.23 (m, 3H), 1.16-1.12 (m, 6H). ; 13C NMR (100 MHz, DMSO-d6) δ 173.49, 171.14,171.10, 171.06, 162.06, 161.86, 161.66, 158.15, 157.26, 157.15, 152.55, 152.37, 147.77, 147.58, 137.74, 131.51, 129.11, 127.94, 126.09, 110.20, 110.06, 109.34, 108.85, 107.62, 107.56, 95.80, 44.31, 38.68, 38.67, 28.88, 26.77, 26.59, 22.80, 22.17, 21.86, 12.29; ESI-MS calculated for $C_{54}H_{61}N_7O_{13}$ [M+H]+ 1015.4327, found 1015.4302.

Cell Lines and Culture Conditions

Cell Lines 293T, A549 and NCI-H460 were obtained from the American Type Culture Collection (ATCC) and were cultured in RPMI-1640 medium (Sigma Aldrich) with 10% fetal bovine serum (FBS) and 1% penicillin/streptomycin and maintained at 37°C in 5% CO_2 unless otherwise noted. The cells were used in transfection assays and total RNA isolation was carried out with Trizol reagent for the RT-qPCR assays (TaqMan miRNA Assay).

Carrier Conjugation with miRNA

Carrier **K** and **E** were dissolved in PBS at 10mM and aged for 24 hours to allow for nanofibers to self-assemble. The solution is diluted to 1mM immediately prior to experiments. Equal volumes of miRNA (5nmol) and **K** or **E** are mixed together for 4

hours at room temperature, final carrier concentration in the mixture is 0.5mM. The solution is then ultracentrifuged at 80,000rpm for 1 hour, and the supernatant is removed. The pellet at the bottom of the tube consists of fully formed carrier **K** or **E** along with miRNA that has electrostatically bound to the carriers. The supernatant consists of unbound excess miRNA, and **K** and **E** molecules that has not formed naonfibers. The pellet is resuspended at the original volume and the concentration of miRNA is determined by UV at 260nm (NanoDrop). This solution of carrier/miRNA conjugate is used for transfection related experiments unless otherwise noted.

Transfection for qPCR

miRNA were purchased from Sigma Aldrich and the positive control, lipofectamine RNAiMAX was purchased from ThermoFisher and transfection was carried out in accordance with the manufacturer's instructions. Briefly, A549 was plated in 6cm dish ($0.1x10^6$ cells / plate) for 16 hours prior to the addition of experimental reagents to allow for the cells to adhere. Experimental conditions are as follow: negative control without have any additives, miRNA without any form of carrier, lipofectamine RNAiMAX as carrier, **K** and **E** as carrier following aforementioned carrier preparation, **K** as carrier following lipofectamine RNAiMAX instructions. After 48 hours, levels of miRNA transfection was analyzed using real-time quantitative PCR.

Real-Time quantitative PCR

Levels of miR-16 and let-7a were analyzed by real time quantitative RT-qPCR using TaqMan MicroRNA assay specific for hsa-miR-16-5p of human origin (miR-16 sequence: 5' UAGCAGCACGUAAAUAUUGGCG 3') and hsa-let-7a of human origin (let-7a sequence: 5' UGAGGUAGUAGGUUGUAUAGUU 3'). Briefly, total RNA was extracted using Trizol reagent, and 10 ng of RNA was retro-transcribed to cDNA using the Taqman miRNA assay. cDNA was then amplified by StepOne Real-time PCR instrument using specific TaqMan primers and TaqMan Universal PCR Master Mix to detect miR-16 and internal control, RNU6B. (RNU6B sequence: 5' CGCAAGGATGACACGCAAATTCGTGAAGCGTTCCATATTTTT 3'). The internal control corrects variations in the experiment. Only mature miR-16 and RNU6B are detected using these assays. ΔΔCt values were used to assign a fold value, which was calculated as $2^{-\Delta\Delta CT}$.

Intracellular Flow Cytometry

A549 cells were seeded in 6cm plates ($0.3x10^6$ cells / plate) for 16 hours prior to addition of 30uM of **K** and **E**. Cells were washed once with ice cold PBS prior to trypsinization. Cells were resuspended in HBSS and kept on ice before subjected to flow cytometer (BD FACS Aria III). Fluorochrome DAPI was used, excitation wavelength at 355nm, emission wavelength 425 – 475nm. A total of 10^4 events per sample were recorded. A bifurcated gate was used on the control untreated cells population to calculate statistics above threshold values as fluorescence intensity (uptake).

Cell Survival MTT Assay

A549 cells were seeded in 48 well plates ($1.0x10^4$ cells/ well) in medium for 16 hours prior to the addition of **K** and **E**. Concentrations of the nanofibers were 0, 3, 10, and 30 μM and the cells were cultured for 96 hours prior to viability analysis. Cell viability was determined using MTT assay and absorbance was measured by SpectraMax M2 Microplate Reader (Molecular Devices).

Preparation of Stable Cell Line

pLenti-UTR-Luciferase Blank Vector was purchased from abm and the experiments were carried out following manufacturer's protocol. In short, cyclin E1 3'UTR (sequence 5'

CAAAGAAAGCCATGTTGTCTGAACAAAATAGGGCTTCTCCTCTCCCCAGTGG

GCTCCTCACCCCGCCACAGAGCGGTAAGAAGCAGAGCAGCGGGCCGGAAAT

GGCGTGACCACCCCATCCTTCTCCACCAAAGACAGTTGCGCGCCTGCTCCAC

GTTCTCTTCTGTCTGTTGCAGCGGAGGCGTGCGTTTGCTTTTACAGATATCTG

AATGGAAGAGTGTTTCTTCCACAACAGAAGTATTTCTGTGGATGGCATCAAA

CAGGGCAAAGTGTTTTTTATTGAATGCTTATAGGTTTTTTTTAAATAAGTGGG

TCAAGTACACCAGCCACCTCCAGACACCAGTGCGTGCTCCCGATGCTGCTAT

GGAAGGTGCTACTTGACCTAAGGGACTCCCACAACAACAAAAGCTTGAAGCT

GTGGAGGGCCACGGTGGCGTGGCTCTCCTCGCAGGTGTTCTGGGCTCCGTTGT

ACCAAGTGGAGCAGGTGGTTGCGGGCAAGCGTTGTGCAGAGCCCATAGCCAG

CTGGGCAGGGGGCTGCCCTCTCCACATTATCAGTTGACAGTGTACAATGCCTT

TGATGAACTGTTTTGTAAGTGCTGCTATATCTATCCATTTTTTAATAAAGATA ATACTGTTTTTGAGACAGCTGGTTTTATGAGCTATGTCTGG 3') was annealed into the vector using KpnI and MfeI restriction enzymes. The engineered plasmid was amplified in E. Coli and then transformed into 293T along with envelope plasmid, VSV-G, and packaging plasmid, Δ8.2, for lentivirus formation. 48 hours later lentivirus is collected and precipitated using PEG-it (SBI) overnight at 4°C. The viral particles are resuspended in Opti-MEM reduced serum medium (ThermoFisher) and added to A549 for infection with TransDux (SBI). 48 hours after the infection, the cells were selected with puromycin to ensure that only the cells that has been successfully infected with our desired plasmid survives.

Luciferase Assay

Aforementioned stable cell line cells were seeded in 6 well plates ($5.0x10^5$ cells/ well) 16 hours prior to experiment to allow for cells to adhere. Commercialized miRiDian miR-16 mimic (Dharmacon) and its negative control were conjugated with **K** using the carrier preparation method above, and the solution was added to the wells using RNAiMAX lipofectamine miRNA concentrations as a guideline. The experimental conditions are as follow: Commercialized negative control with lipofectamine, commercialized negative control with **K**, miRiDian miR-16 mimic with lipofectamine, miRiDian miR-16 with **K**. miR-16 function is measured as a percentage of luciferase fluorescence of miR-16 over that of the negative control.

Gel-Electrophoresis

Carrier conjugated with let-7a solution as prepared following procedure above was run on ethidium bromide infused 1% agarose gel (EmbiTec) at 50mV. The experimental conditions are as follow: 1kb marker, **E** alone, **E** with let-7a, **K** alone, **K** with let-7a, and negative control let-7a. The negative control is a solution with only let-7a that follows the procedure for the conjugation to occur, using DEPC water in place of the carrier solution. After ultracentrifuge a pellet is absent in the negative control tube and the solution is decanted. The tube is then rinsed with DEPC water and this sample is run on the gel to ensure the let-7a band in other conditions are not pseudo positive bands from residual miRNA on the wall of the tube. The bands were then visualized under UV 260nm.

Confocal Microscopy

Confocal Microscopy was performed with either Olympus Filter FV1000 Confocal Microscopy or Olympus Spectral FV1000 Confocal Microscopy. A549 cells were seeded at $5.0x10^4$ cells/ well in Lab-Tek II Chamber Slide (4 well) and allowed to adhere for 16 hours. miR-16-Cy5 (Sigma Aldrich) was conjugated to **K** using the procedure mentioned above and added to culture medium. The conditions for each chamber is as follow: negative control with cells only, miR-16-Cy5 without carrier, miR-16-Cy5 conjugated to carrier **K**, and **K** only. After 48 hours of incubation the medium was removed and rinsed with PBS and fixed with 4% paraformaldehyde for 15 mins at 37°C. The plate was washed with PBS (5 mins x 3) and membrane dye was added to the chambers for 10 mins at room temp (Wheat Germ Agglutinin Alexa Fluor 488 Conjugate, ThermoFisher). The

plate was again washed with PBS (5 mins x 3) and the chamber walls were removed and glass cover was applied with antifade mounting medium (Vectashield). Carrier **K** was visualized at 405nm (blue), membrane dye was visualized at 488 (green), and miR-16-Cy5 was visualized at 535nm (red).

Transmission Electron Microscopy

Transmission Electron Microscopy (TEM) was performed with Technai G2 Spirit instrument operating at 80 kV. **K** and **E** were aged in PBS (10mM, pH 7.4) for 24 hours prior to imaging. The samples were freshly diluted to 0.5mM and applied to carbon coated copper grid (Ted Pella, Inc.) for 2 mins and negative stained with 2% wt uranyl acetate solution for 1 min. Streptavidin conjugated colloidal gold nanoparticles purchased from Cytodiagnostics (5nm, OD3) were used to visualize miR-16 on the fiber and the sample preparation procedure was performed in accordance to manufacturer's protocol. miR-16-biotin (Sigma Aldrich) was conjugated with **K** using the procedure above and the resuspended solution was applied to carbon coated copper grid for 30 mins, the copper grid was then quickly placed on PBS to rinse off excess **K**, and dried with filter paper. Streptavidin conjugated colloidal gold was diluted 1:100 in 1% BSA (Bovine Serum Albumin) in PBS and the copper grid was placed on this solution for 1 hour. The copper grid was then placed on 1% BSA in PBS for 5 mins x 5 to wash off excess gold nanoparticles on the grid and dried with filter paper.

Chapter 2: The Chemotherapeutic Applications of Self-Assembled Nanostructures

Chapter 2.1: The Self-Assembly of Anticancer Camptothecin-Dipeptide Nanotubes: A Minimalistic and High Drug Loading Approach to Increased Efficacy.

(This sub-chapter is adapted from previous publication in CHEMISTRY: A European Journal in 2014, my main contribution for this publication is towards the cellular / biological studies. doi: 10.1002/chem.201404520)

Introduction

Nanotechnology-enhanced drug delivery is emerging as an important strategy to improve the performance and reduce the toxicity of a wide range of chemotherapeutic agents.[106] As such, solid-nanoparticle scaffolds[107-110] and self-assembled materials[111-114] have shown tremendous promise for the development of novel cancer detection and therapeutic nanoparticle technologies. The mass of many of these systems is predominantly inert carrier, compared with that of the active drug, thus requiring larger quantities to be administered. For clinical applications, repeated administration of high

doses of drug carriers has the potential for systemic toxicity as well as the extra burden for patients to eliminate the carriers.[115] Ideally, such nanomedicine would be primarily composed of the active drug. Recent elegant approaches to high-density drug nanocarriers include the use of drug-conjugated dendrimers[116] and self-assembling polypeptides.[117] In this work, we describe the self-assembly of small 20-(S)-camptothecin (CPT)-dipeptide conjugates into well-defined nanotubes with a ~47% CPT loading level. These CPT-peptide nano-assemblies exhibit enhanced resistance to hydrolytic deactivation and show high *in vitro* potency against several human cancer cell types.

Camptothecin (CPT), originally isolated from the Chinese tree *Camptotheca acuminata*, possesses potent anti-tumor properties over a wide range of cancers through its inhibition of topoisomerase I.[118, 119] However, CPT exhibits several properties that severely limit its clinical application, such as low aqueous solubility, high levels of plasms protein binding, and poor biodistribution. Camptothecin also undergoes a reversible pH-dependent ring-opening reaction between the active lactone and inactive carboxylate form, which has also been shown to be toxic (**Figure 16**).[120] In addition, lactone hydrolysis is enhanced by the specific binding and sequestration of the carboxylate form to various proteins, such as human serum albumin, in the biological matrix.[120-122] Finally, considerable variability in the oral and intravenous bioavailability of CPT suggests poor cellular and tumor uptake of unmodified CPT drugs,[123] and therapeutic application of unmodified CPT is hindered by very low solubility in aqueous media, high toxicity, and rapid inactivation through lactone ring hydrolysis at physiological pH.

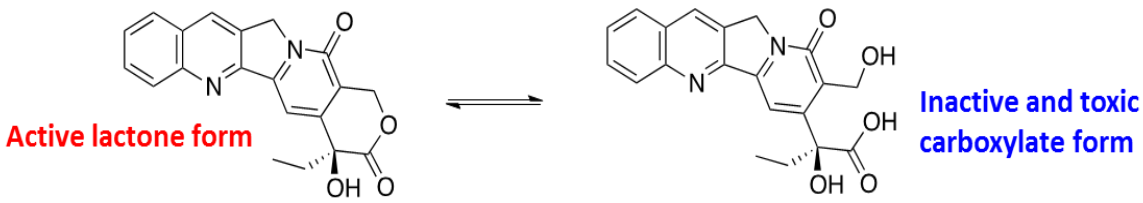

Figure 16. The lactone ring undergoes ring opening due to hydrolysis in aqueous solution at neutral and basic pH. Only the lactone form, which is stable in an acidic environment at pH < 5.5, has anti-cancer (topoisomerase inhibition) properties. The carboxylate form is rapidly formed in human serum at pH 7.4, and binds to human serum albumin, which is one of the most abundant proteins in serum. The carboxylate-albumin conjugate is rapidly cleared by the kidneys and leads to severe side effects.

Results and Discussion

The design strategy used here is based on our prior studies that demonstrate the self-assembly of di-lysine peptides functionalized at the ε-amino position on one residue with a 1,4,5,8-naphthalenetetracarboxylic acid diimide (NDI) chromophore.[124, 125] These peptides self-assembled into 1D helical nanofibers and twisted nanoribbons in aqueous solution, de-pending on the placement of the NDI group. The NDI chromophore drives self-assembly through hydrophobic effects and π-π stacking interactions. We reasoned that replacing the NDI molecule with the CPT structure would replicate this design strategy. The CPT molecule was appended to an ε-amino group of di-lysine by a 20-O-

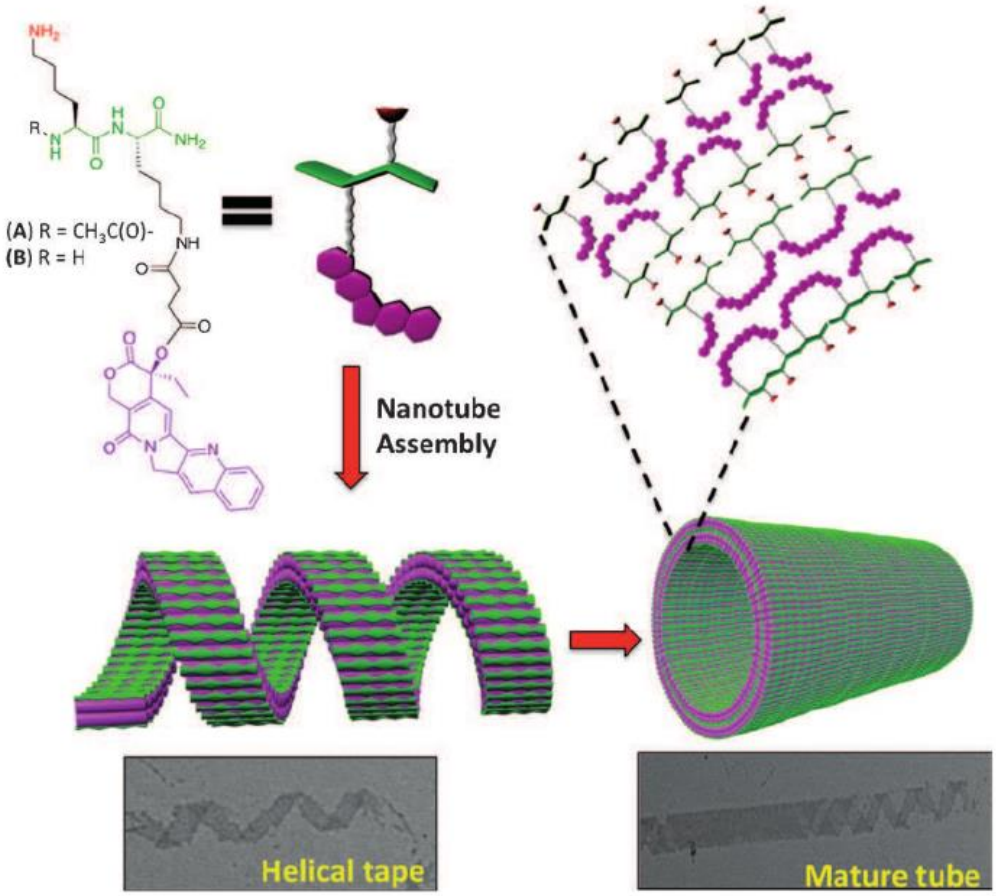

Figure 17. Self-assembly of CPT-dipeptide into nanotubes, where individual molecules are slowly stacked together to form a helical tape and the helical tape then stack together to form the mature tube.

succinyl linkage[126] to prepare compounds Ac-KK(CPT)- NH_2 (A) and NH_2-KK(CPT)-NH_2(B) (**Figure 17**). The CPT–peptides were prepared by using 9-fluorenylmethoxy-carbonyl (Fmoc)/tBu solid-phase peptide synthesis followed by on-resin amidation of the

side chain with 20- O-camptothecin succinic acid. The synthesis is facile, automated, scalable, and high yielding.

The self-assembly of dipeptide Ac-KK(CPT)-NH_2(A) was studied by transmission electron microscopy (TEM) in phosphate buffered saline (PBS) (**Figure 18**). After aging at 10 mM in PBS for 3 days prior to diluting to 1 mM, A produced 1D nanotubes with diameters ranging from 80–120 nm and lengths of several micrometers (**Figure 18A**). In contrast, only non-specific aggregation was observed at 1 mM without pre-incubating at 10 mM. A few coiled ribbons and helical tapes were observed along-side the fully formed nanotubes when 10 mM solutions of A were diluted to 1 mM (PBS) and imaged after only one day, suggesting the structures as intermediates leading to the formation of uniform nanotubes.[127] TEM images of A displayed short nanofibers after three days in pure water (10 mM), and nanofibers increased in length over two weeks (**Figure 19**). TEM images of samples of NH_2-KK(CPT)-NH_2 (B), prepared by dissolving in water or PBS at 10 mM then diluting to 1 mM after three days, indicated the formation of nanotubes with similar dimensions (80–120 nm) (**Figure 18B**). In addition, when the molecules were prepared in human serum, nanotubes were still visible (**Figure 20**). Solutions initially prepared at low concentrations of PBS (0.25 mM) did not produce nanotubes. The impact of pre-incubating at high concentration prior to dilution suggested that fully matured nanotube structures were initially stable at concentrations below the critical micelle concentration (CMC). The CMCs of freshly dissolved solutions of A and B, prepared without pre-incubation, were 350 and 420 μM, respectively, measured using

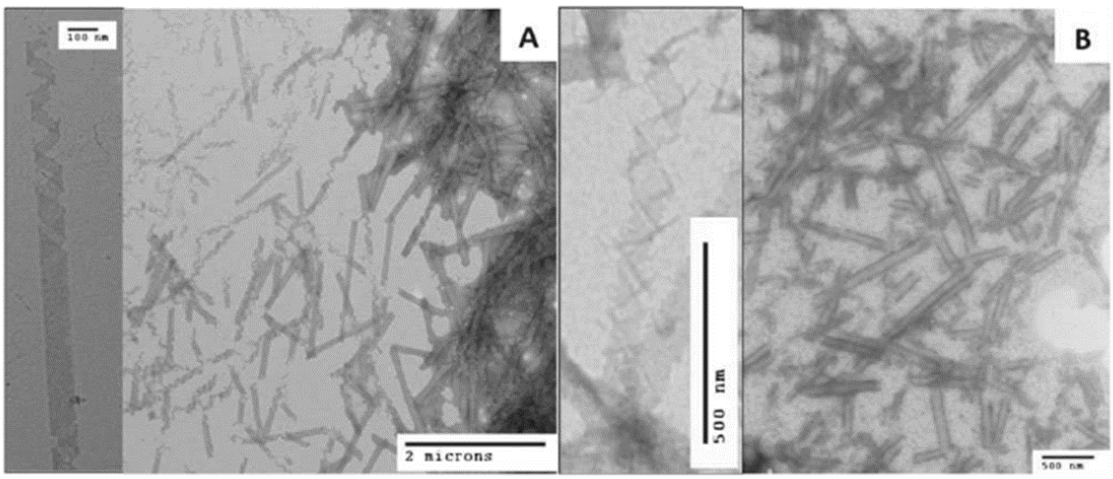

the solvochromatic dye Nile Red (**Figure 21**)[128]. The stability of the nanotubes toward dilution was determined by recording the concentration dependence of the CPT

Figure 18. Self-assembly of nanotubes from Ac-KK(CPT)-NH_2 (A) and NH_2-KK(CPT)-NH_2 (B) in PHB (pH 7.4). Insets are magnification nanotubes, and the samples were prepared with 10mM for 24 h aging before diluting to 1mM immediately prior to making imaging grids.

fluorescence, which quenches in aggregated states.[129, 130] Thus, samples, prepared by diluting 10 mM solutions in PBS, exhibited dissociation concentrations of 8.7 (A) and 21 nm (B) after 5 minutes. Similar values were measured after 24 h, suggesting that the preformed nanotubes were quite stable to dilution below the CMC (**Figure 22**).

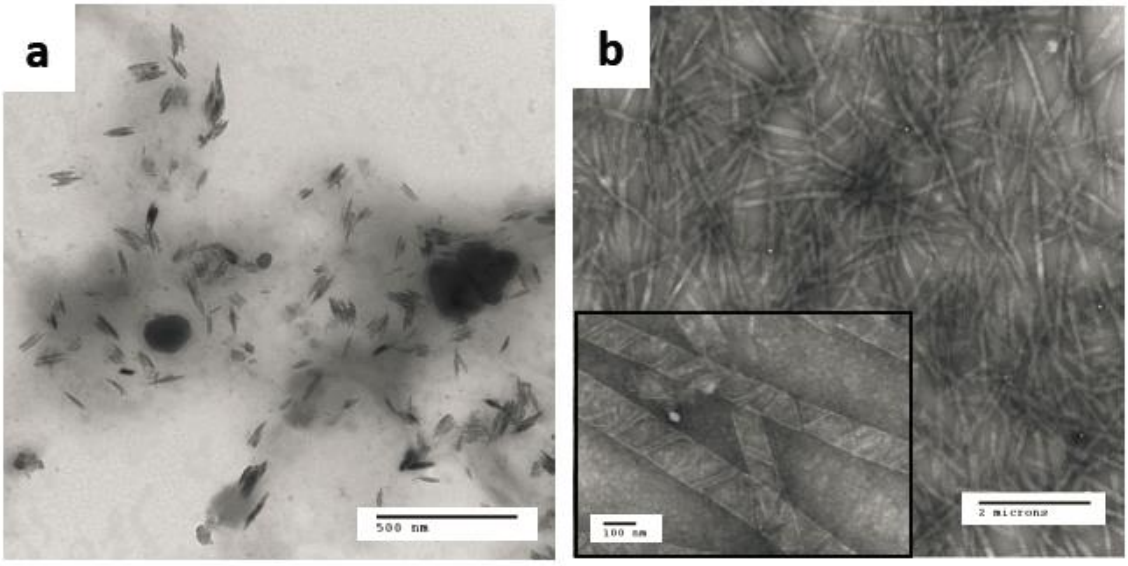

Figure 19. TEM images of **A** and **B** in water. Samples were prepared by dissolving the CPT-dipeptides in water at 10mM and freshly diluted to 1mM prior to making imaging grids after 3 days of aging.

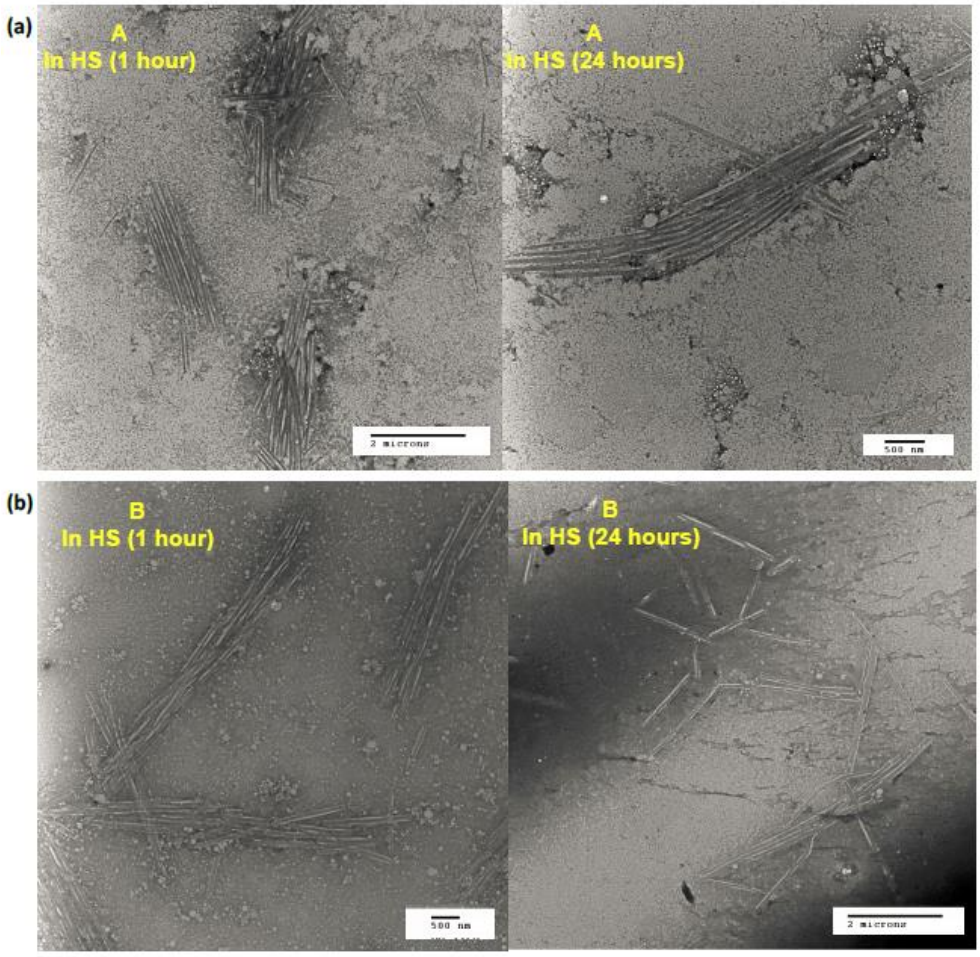

Figure 20. TEM of A and B after 1 hour and 24 ours of aging at 10mM in human serum.

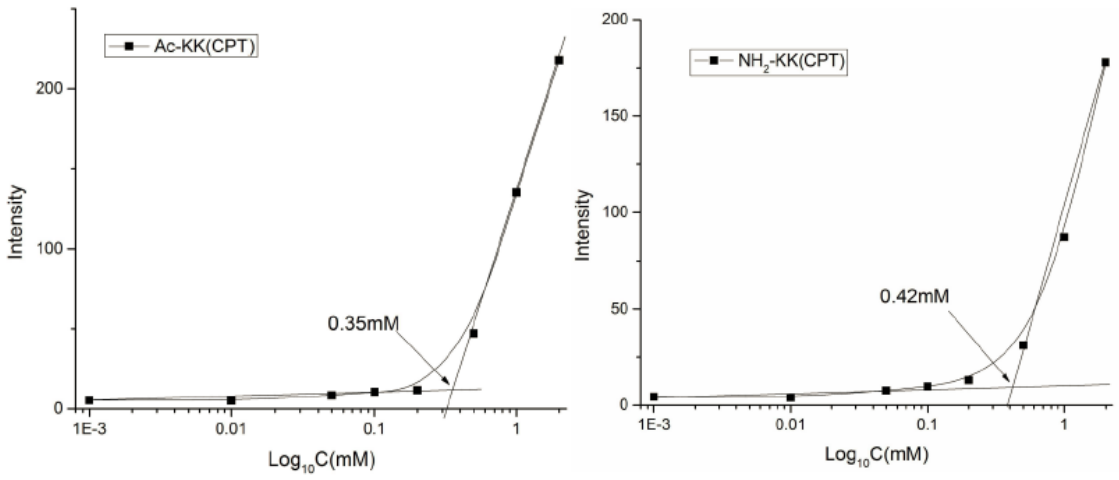

Figure 21. Plot of fluorescence intensity of Nile Red at 656 nm (excitation = 550nm), x-axis is the concentration in mM of A and B in PBS.

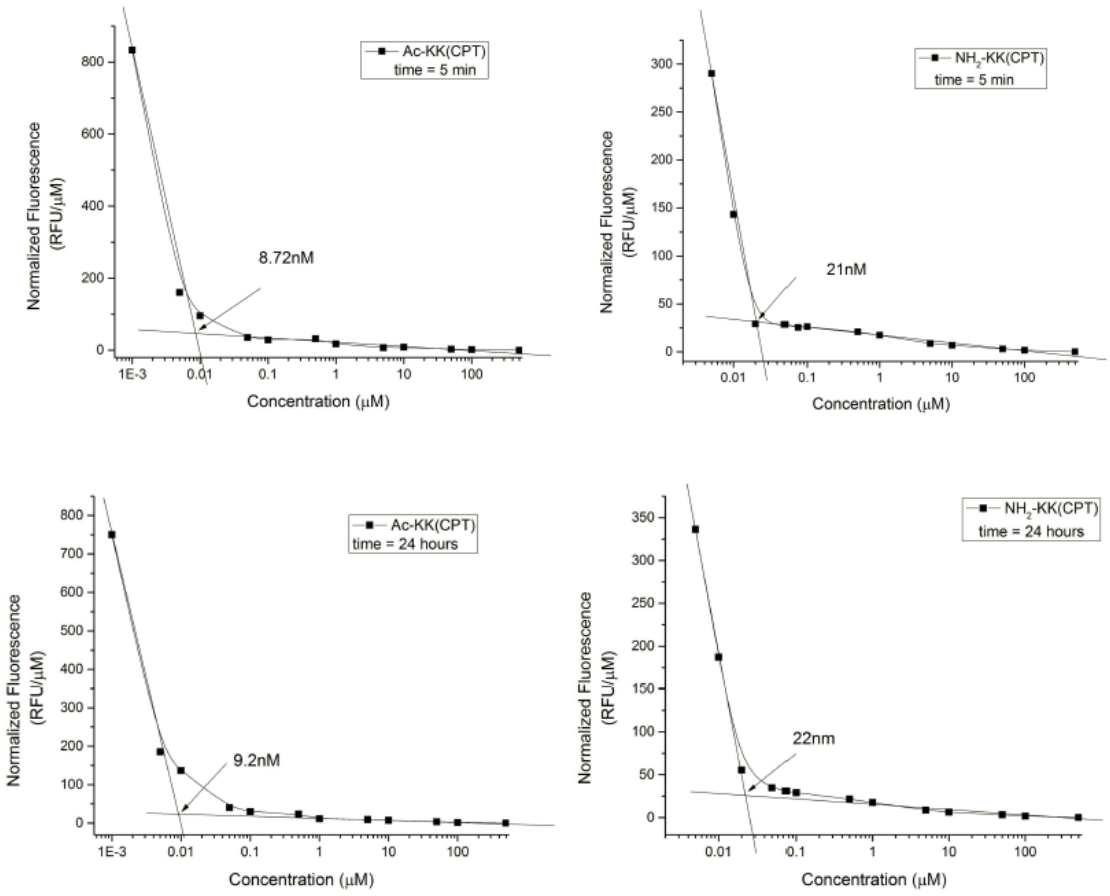

Figure 22. Fluorometric determination at 425 nm (excitation = 350 nm) of the stability towards dilution of A and B after incubating in PBS at 10mM.

Next, Fourier-transform infrared (FTIR) and UV/Vis spectroscopy were used to further study the intermolecular interactions that stabilize the nanotubes. Solutions of A and B, pre-pared in PBS (20 mM ,D_2O), displayed relatively weak amide I ($\upsilon_{C=O}$) bands at 1625 cm^{-1}, characteristic of β-sheet secondary structure,[131] and a larger band at 1650 cm^{-1} in the deconvoluted spectra owing to the presence of a random coil conformation.

Deconvolution of the spectra indicated that the nanotubes were comprised of 64 % random coil and 36 % β-sheet structures. The UV/Vis spectra of both dipeptides in PBS displayed two bands at 350 and 368 nm that were slightly redshifted compared with solutions measured in trifluoroethanol (TFE), in which both are minimally aggregated. The lower ratio of the bands at 350 and 368 nm, along with the significantly lower extinction coefficients in PBS, compared with TFE, were consistent with the formation of *J*-aggregated CPT chromophores within the assemblies.[132] These observations suggest that self-assembly is predominantly driven by amphiphilic phase segregation in aqueous media, exhibiting limited β-sheet structures.

Although hydrolytic cleavage of the 20-O-succinyl linkage is required to produce active CPT, hydrolysis of the lactone ring of CPT has a detrimental impact on its biological activity. Further, the high affinity of the carboxylate form for human serum albumin (HSA) accelerates the hydrolytic deactivation of the drug. We reasoned that sequestering the CPT molecules within the hydrophobic walls of the nanotube would protect the drug from both water and HSA, and thereby reduce the rates of lactone hydrolysis and CPT release, which occurs by hydrolysis of the 20-O-succinyl linkage. The stability of A and B in PBS at 37 ˚C was measured by HPLC over one week as a function of concentration (**Figure 23**). In contrast to CPT, which underwent hydrolysis to

the inactive carboxylate form within hours in PBS, nanotubes of A and B were 91 % and 77 % intact after 7 days when stored at 10 mM.

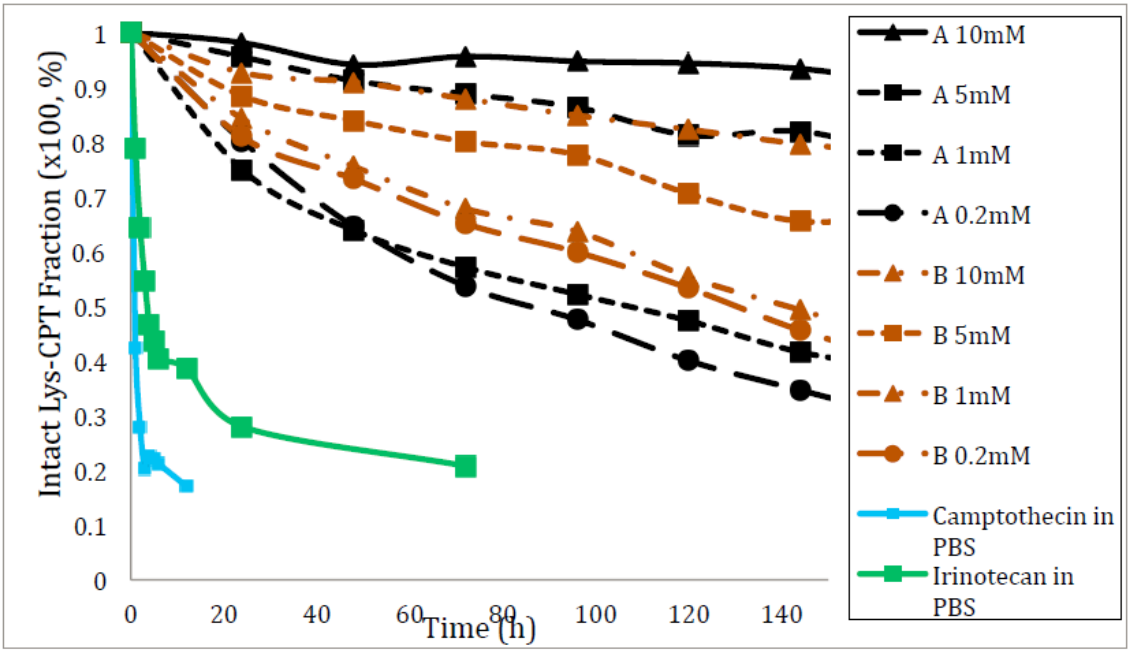

Figure 23. Time and concentration dependent CPT-dipeptide stability monitored by analytical reverse-phase HPLC in PBS. The dipeptides were prepared in PBS at 10mM and then diluted to the desired experimental concentrations after 24 hours of aging. Samples were incubated at 37 ˚C, and the proportion of lactone (active) to carboxylate (inactive) form was monitored by HPLC. In green is the camptothecin parental drug, and in green it is Irinotecan, clinically used CPT derivative as comparison for stability.

It is noteworthy that exposure of A and B to these conditions produced free CPT–lactone and CPT–carboxylate owing to cleavage of the 20-O-succinyllinkage, rather than lactone hydrolysis of the intact CPT–dipeptide (<1 %). For example, after 7 days at 10 mM (PBS), A remained 91% intact, producing ~7 % free CPT–lactone without significant lactone hydrolysis of either free CPT or A. Under the same conditions, B was slightly less stable, producing both CPT–lactone (6 %) and CPT–carboxylate (13 %). The overall stability, with respect to lactone hydrolysis and ester cleavage, of A or B in PBS depended strongly on concentration (**Figure 23**). Thus, the amount of intact CPT–dipeptide present progressively decreased from 91 % to 30 % for A, and from 77 % to 40 %, for B, going from 10 to 0.2 mM, measured after 7 days. Even under these conditions, the major hydrolysis product was free CPT, present in both carboxylate and lactone forms. This progression was consistent with the noncovalent nature of the nanotube structures, which sequesters the ester linkages from the aqueous phase and the external environment. Accordingly, hydrolysis may occur upon dissociation of the monomer from the nanotubes or by partial exposure of the ester linkages within the assembly. Thus, the difference in the rates of CPT release in HS between A and B likely emerges from small changes in the stability and structure of the nanotubes, which would affect the accessibility of the ester linkages to the aqueous media and HSA. Overall, the nanotubes exhibit much greater lactone stability, preferentially undergoing cleavage of the ester linkage, compared with free CPT, of which 17 % remained in the lactone form after 24 h under these conditions.[122]

The noncovalent nature of the intermolecular interactions that stabilize the structure of the nanotubes creates a potential for their structures to vary under physiological conditions. In particular, HSA, which is the most abundant plasma protein in the body,[133] has the potential to destabilize or modify the nanotube structures, which may impact their biodistribution, cell permeability, and stability. Fortuitously, TEM imaging of samples prepared by diluting A and B (10 mM PBS) to 1 mM with human serum (HS) revealed that the nanotubes were present in HS after 24 h at 1 mM (**Figure 24 b-c**).

Hydrolysis of the CPT nanotubes was also examined in HS at 37 ˚C by preparing 20 mM solutions of A and B in PBS, then diluting with HS after 24 h. The solutions were treated with cold methanol to precipitate the proteins, and the supernatant was analyzed by HPLC. After 30 h at 10 mm in HS, dipeptide A was predominantly intact (~ 89 %), whereas B was ~ 40 % intact. (**Figure 24 a**). The dipeptides were less stable when the solutions were diluted to 1 mM in HS, similar to the studies in PBS. However, A exhibited significantly greater stability at all concentrations than B. In contrast, both CPT and irinotecan were predominantly in the carboxylate form after 1–3 h in HS.

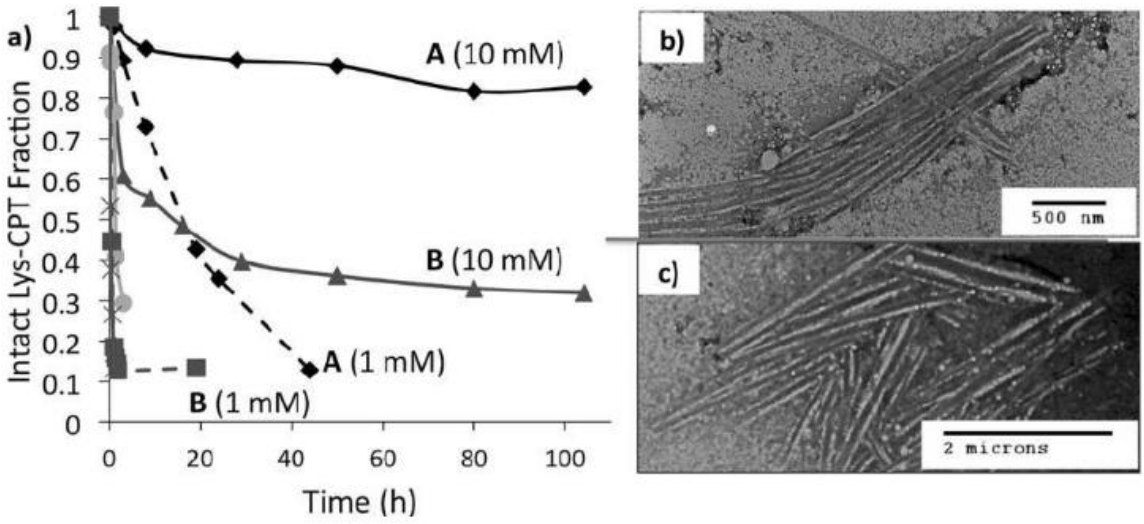

Figure 24. a) CPT-dipeptide stability in human serum at 37 ˚C, pH 7.4 and 1mM vs. 10mM. b) TEM of A in human serum for 24 hours. c) TEM of B in human serum for 24 hours. Samples aged at 10mM and diluted to 1mM prior to imaging.

Although it was not possible to identify all the degraded products of A and B in HS, hydrolysis of the succinyl linkage dominated the degradation process for both A and B. The nanotubes formed by A and B display positive zeta potentials of 27.7 and 39.9 mV, respectively, which may be attributed to the presence of protonated amines on the surface of nanotube structures. HSA has a net negative charge at physiological pH.[134] Thus, the lower stability of B in HS, compared with A, may emerge from greater nonspecific, electrostatic binding to the surface of HSA.[135]

The CPT–dipeptides, CPT, and clinically used irinotecan were then assessed for their efficacy against human colorectal adenocarcinoma (HT-29) cells. This cell line was

chosen as irinotecan is a first line chemotherapeutic agent used for the treatment of colon cancer.[136] Irinotecan is a prodrug, where the solubilizing piperidinopiperidine group is cleaved by carboxylesterases to form the potent agent SN-38.[137] The prodrug has been adopted clinically over the active metabolite SN-38 be-cause the poor solubility of SN-38 (~36 μg mL^{-1} in PBS)[138] prohibits delivery of clinically relevant doses. Irinotecan itself is not very potent and only 2–8 % is metabolized to form the active drug SN-38 *in vivo*.[139, 140] In addition, as discussed earlier, hydrolysis of the lactone ring inactivates the drug. These two limitations reduce the anticancer efficacy of irinotecan, while the common severe side effects of diarrhea, myelosuppression, and hemorrhagic cystitis, remain as critical drawback.[141] **Figure 25** shows the superior efficacy of the dipeptide conjugates A and B against the HT-29 cell line with an IC_{50} of 50 and 63 nm, respectively, versus 2μm for irinotecan. CPT is the most potent, IC_{50} of 8 nM, but CPT is not clinically used owing to its limited aqueous solubility and toxicity.

The performance of CPT-dipeptides, CPT, and irinotecan was examined in three additional human cancer cell lines (non-small cell lung A549, NCI-H460, and NCI-H23 cells). The IC_{50} values of A and B were 351 and 970 nm againstA549, 626 and 188 nm against H460, and 368 and 97 nm against H23, respectively (**Figure 26**). These values are significantly lower than the IC_{50} values of > 10, 6.1, and 7.7 μm for irinotecan ($p < 0.0001$). These results are similar to those observed with the HT-29 cells, in that the CPT–dipeptides are more potent than irinotecan. In contrast, CPT was slightly more potent than A and B with IC_{50} values of 167, 101, and 19 nm for A549, H460, andH23 cells, respectively ($p < 0.001$).

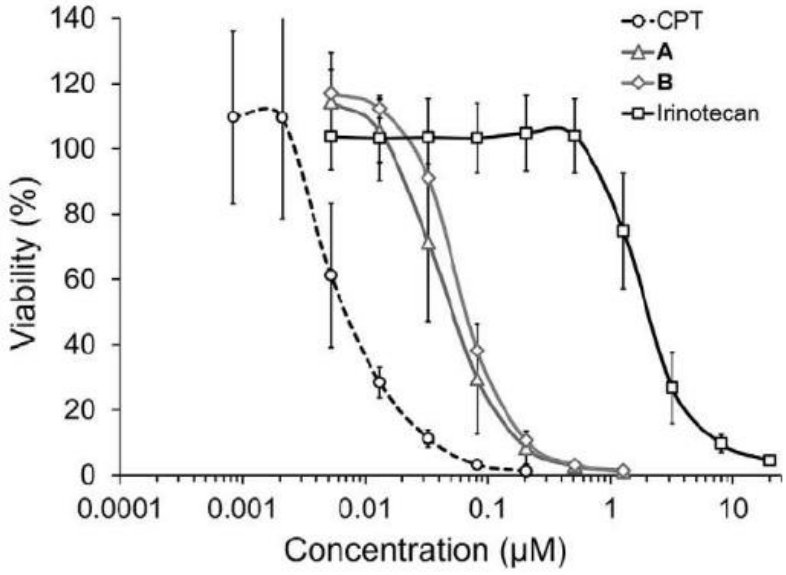

Figure 25. Cell cytotoxicity assay on human colorectal HT-29 cancer cells for compounds A and B and with parental CPT and clinically used Irinotecan for comparison. CPT has the strongest anti-cancer property with IC_{50} at 8nM while irinotecan has the lowest at 2μM. A and B are in between at 50nm and 63nm, respectively.

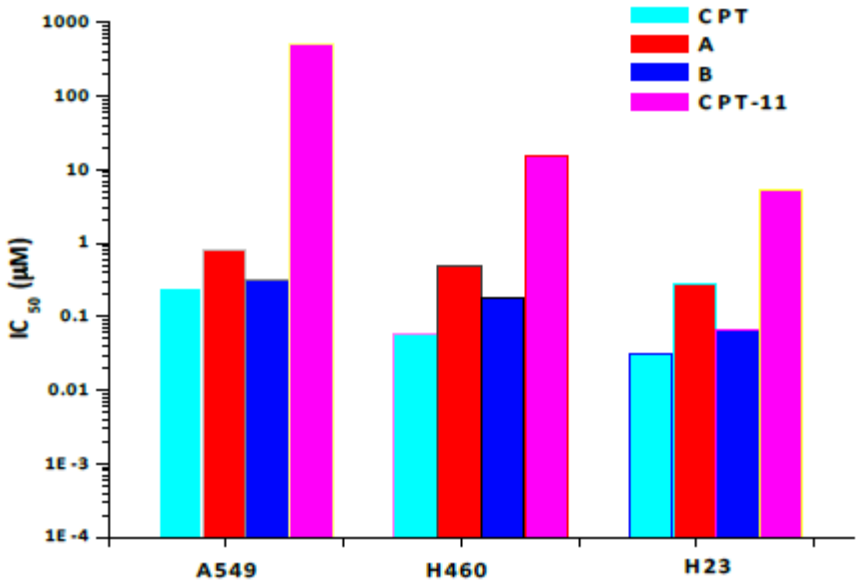

Figure 26. IC_{50} results showing CPT and its derivatives' drug efficacy against human non-small cell lung cancers, A549, H460, and H23. These cells were chosen based upon the different BCRP expression level, with A549 the highest, and H23 the lowest. Drug efficacy was highest in H23 as expected (lowest amount of drug resistance).

Finally, flow cytometry and confocal microscopy were performed with HT-29 cells to monitor cellular uptake of the CPT–dipeptides (**Figure 27**). First, to quantify the cellular uptake as a function of time, flow cytometry was conducted by monitoring the CPT–dipeptides at a wavelength of 420–470 nm after 335 nm excitation. **Figure 27** summarizes the percentage of fluorescent cells (i.e., uptake) compared with the control cells. Irinotecan-treated cells consistently had the highest fluorescence for all incubation periods. On the other hand, the CPT–dipeptides exhibited time-dependent uptake. Uptake

of B was slightly higher than for A (**Figure 27**), and cells treated with free CPT exhibited lower uptake than that of irinotecan, and similar uptake to the nano-assemblies.

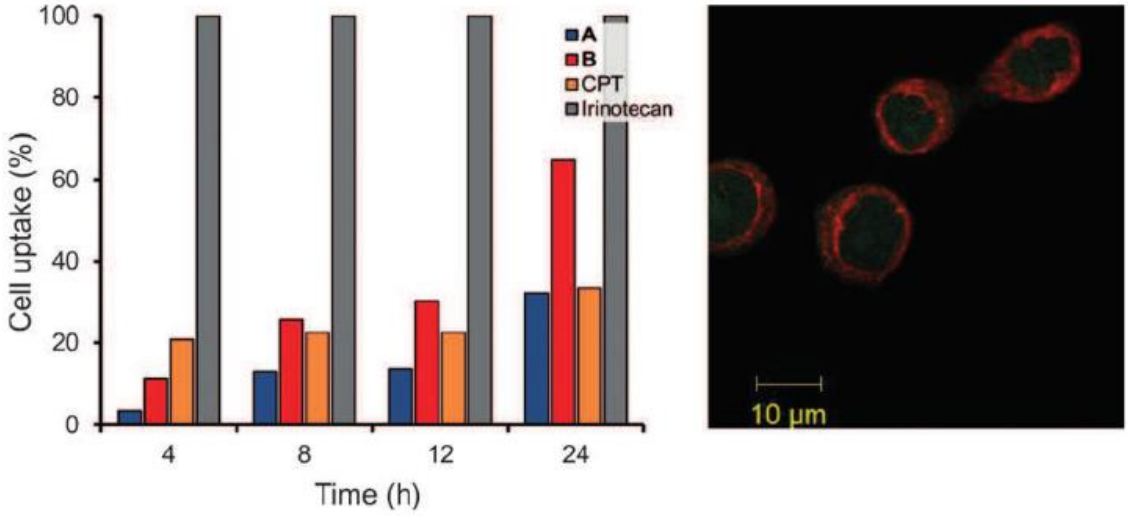

Figure 27. Left is the flow cytometry results showing intracellular drug accumulation of A, B, irinotecan, and CPT for HT-29 cells. On the right it is the confocal images of HT-29 cells showing the uptake of CPT-dipeptide B after exposure for 4 h at 200μM. Orange is the membrane dye while green is B.

An analogous flow cytometry study was performed with A549 cells, and similar results and trends were observed. Time dependent study shows that there is a steady increase in drug molecule accumulation within the cells over a 24 h time period as

visualized with flow cytometry (**Figure 28**). The accumulation of drugs were also studied in normal human bronchial epithelium (BEAS-2b) and the results are shown in **Figure 29.**

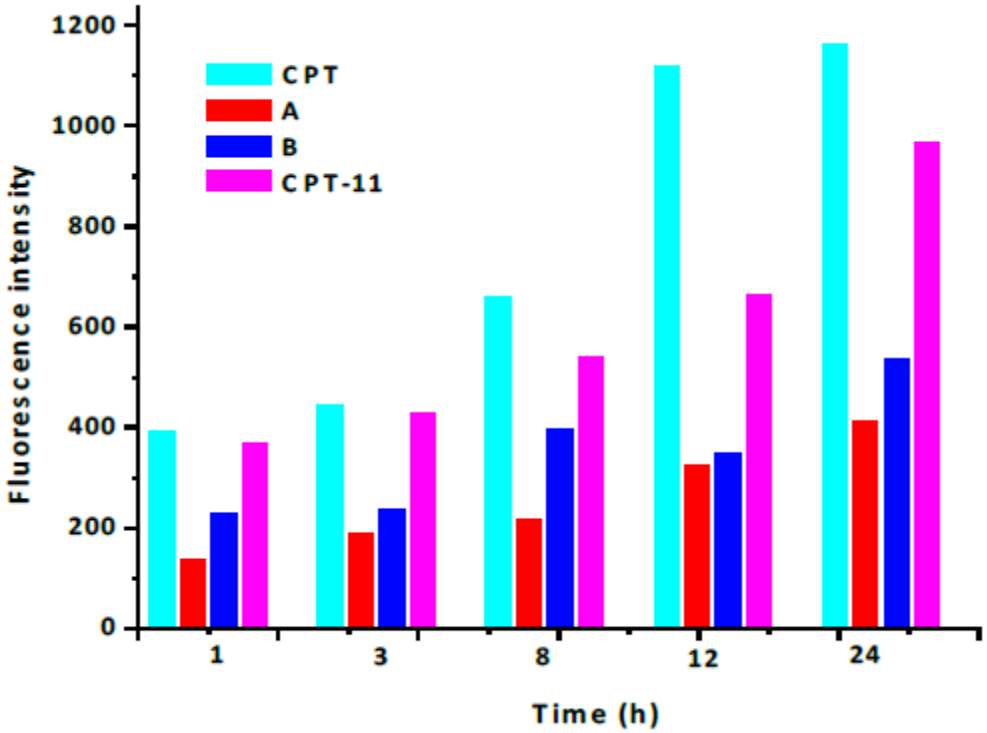

Figure 28. Normalized time-dependent flow cytometry results showing steady increase in intracellular drug accumulation on human NSCLC A549. Cells were treated with 10μM CPT-dipeptide A and B, parental CPT and clinically used irinotecan at different time points and quenched at the same time. Emission was detected at 420-470nm upon excitation at 355nm.

To visualize the CPT–dipeptide within the HT-29 cells, we incubated the cells with B for four hours, fixed the cells, and stained the cell membrane with Alexa Fluor 488-concanavalin A. The cells were then imaged under excitation at 405 and 488 nm, and the emission detected at 420–480 and 505–530 nm for CPT and Alexa Fluor 488-concanavalin A, respectively. As shown in **Figure 27**, the merged fluorescent image shows the CPT–dipeptide (green) dispersed throughout the cytosol with the mem-brane highlighted in red. The slightly lower potency of A and B, compared with free CPT, may be a consequence of the slower rate of cellular uptake and the need for hydrolytic cleavage to produce active CPT.

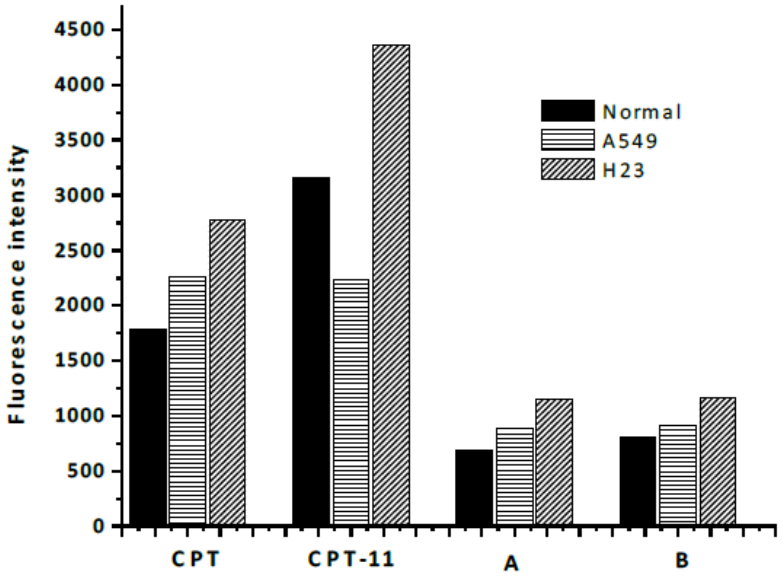

Figure 29. Normalized emission results showing intracellular drug accumulation on NSCLC A549, H23, and normal human bronchial epithelium (BEAS-2b) treated with 10μM CPT dipeptides A and B, compared with CPT and irinotecan using flow cytometry.

In summary, the self-assembly and anticancer activity of two CPT-conjugated dipeptides are reported. These CPT–dipeptides assemble into well-defined nanotubes in both PBS and HS with diameters ranging from 80–120 nm. The nanotube structures sequester the CPT segment within the hydrophobic nanotube walls, thereby protecting the drug from hydrolytic lactone opening. Hydrolytic cleavage of the succinyl linkage readily releases active CPT at rates that depend strongly on concentration. This nanotechnology approach enables high drug loadings and increased CPT stability within the dipeptide nanostructures without the need for excipient, macromolecular carriers.

Experimental Procedure

General Methods

Transmission Electron Microscopy (TEM) was performed with Technai G2 Spirit instrument operating at 80 kV. All reactions were performed under an argon or nitrogen atmosphere. 1H NMR was recorded at 400 MHz and 13C NMR spectra at 100 MHz on a Bruker DPX-400 instrument. Water and trifluoroethanol (TFE) used for CD, UV, and TEM were spectroscopic grade. Phosphate buffered saline (PBS, pH 7.4) and human serum (Human male AB plasma, sterile-filtered) were purchased from Gibco and Sigma-Aldrich, respectively.

Synthesis of CPT-CO2H

1,8-Diazabicycloundec-7-ene (DBU, 4.6 mL, 3 mmol) was slowly at 0 °C to a mixture of (S)-(+)-camptothecin (348.35 mg, 1 mmol) and succinic anhydride (300.3 mg, 3 mmol) in 30 mL of dichloromethane. The reaction mixture was stirred at room temperature for 4 hours, quenched with water (20mL), acidified with 1% aqueous HCl solution. The yellow precipitate was collected and washed with 1% aqueous HCl solution (10 mL× 3) and H2O (10 mL× 3). The crude product was recrystallized with methanol to obtain the pale yellow crystalline product (439 mg, 98%). 1H NMR (400 MHz; DMSO-d6) δ 8.68 (1 H, s), 8.11-8.20 (2 H, m), 7.85-7.89 (1 H, m), 7.69-7.73 (1 H, m), 5.44-5.53 (2 H, m), 5.23-5.33 (2 H, m), 2.68-2.85 (2 H, m), 2.09-2.20 (2 H, m), 0.87-0.94 (3 H, m); 13C NMR (100 MHz; DMSO-d6) δ 172.93, 171.23, 167.13, 145.89, 145.24, 131.51, 131.36, 129.73,

128.98, 128.49, 127.93, 118.89, 95.09, 75.86, 66.28, 50.16, 30.39, 28.55, 28.37, 7.50.; ESI-MS for C24H20N2O7 [M+Na]+ calculated 471.1163; found 471.1187.

General Peptide Preparation

The protected dipeptides were manually prepared using Fmoc/*t*-Bu solid-phase peptide synthesis on rink amide resin (loading 0.59 mmol/g). Amide-coupling steps were accomplished with standard techniques for all amino acids: Fmoc-amino acid, 1,3-diisopropylcarbodiimide (DIC), and 1-hydroxybenzotriazole (HOBt) (500 mol% each relative to resin) in 1:1 DMF/DCM for 1.5 h. A solution of 20% piperidine in DMF was used for Fmoc removal and 1% TFA in dichloromethane was used for Mtt group deprotection. The CPT-peptide conjugates were cleaved from the resin by the treatment with TFA/water/triethylsilane (95/1/4) at room temperature for 2 h. The crude peptides were precipitated with cold diethyl ether and purified by reversed-phased HPLC on preparative Varian Dynamax C18 column eluting with a linear gradient of acetonitrile/water containing 0.1% TFA (10/90 to 100/0 over 30 minutes) and stored as lyophilized powers at 0 °C. Peptide purity was assessed by analytical reverse-phase HPLC and identity confirmed using ESITOF mass spectrometry and NMR.

Ac-KK(CPT)-NH2 (A) 1H NMR (400 MHz, DMSO-d6) δ 8.68 (s, 1H), 8.18-8.11 (m, 2H), 8.04-8.02 (m, 1H), 7.89-7.86 (m, 2H), 7.81-7.79 (m, 1H), 7.75-7.67 (m, 4H), 7.29 (d, *J* = 0.4 Hz, 1H),7.14 (s, 1H), 6.99 (t, *J* = 0.3 Hz, 1H), 5.49 (s, 2H), 5.39 (d, *J* = 81.7 Hz, 7H), 5.29 (s, 2H), 4.23-4.17(m, 1H), 4.12-4.07 (m, 1H), 3.04-2.97 (m, 2H), 2.82-2.68

(m, 4H), 2.39-2.34 (m, 2H), 2.17-2.10 (m,2H), 1.84 (s, 3H), 1.65-1.41 (m, 6H), 1.36-1.23 (m, 4H), 1.23-1.14 (m, 2H), 0.92 (dd, *J* = 9.7, 5.0Hz, 3H).; 13C NMR (100 MHz, DMSO-d6) δ 174.55, 171.52, 171.46, 169.94, 169.44, 167.23,158.26, 157.92, 156.52, 152.34, 147.86, 145.87, 145.44, 131.51, 130.37, 129.72, 128.90, 128.50,127.92, 127.67, 118.74, 115.02, 95.17, 75.81. 66.20, 52.39, 52.12, 50.15, 40.10, 39.90, 39.69, 39.48, 39.27, 39.06, 38.85, 38.67, 38.49, 31.53, 31.20, 30.25, 29.62, 28.94, 28.73, 26.58, 22.71, 22.48,22.21, 7.53.; ESI-MS for C38H47N7O9 [M+H]+ calculated 746.3514; found 746.3522.

NH2-KK(CPT)-NH2 (B) 1H NMR (400 MHz, DMSO-d6) δ 8.70 (d, *J* = 0.6 Hz, 1H), 8.47-8.45 (m,1H), 8.19-8.11 (m, 5H), 7.91-7.85 (m, 2H), 7.84-7.76 (m, 3H), 7.76-7.71 (m, 1H), 7.51-7.48 (m,1H), 7.04-7.02 (m, 1H), 5.54-5.49 (m, 2H), 5.30 (d, *J* = 4.9 Hz, 2H), 4.23-4.17 (m, 1H), 3.84-3.78(m, 1H), 3.08-2.98 (m, 2H), 2.83-2.68 (m, 4H), 2.41-2.32 (m, 2H), 2.19-2.10 (m, 2H), 1.73-1.67 (m,2H), 1.63-1.45 (m, 4H), 1.41-1.19 (m, 0H), 0.94-0.89 (m, 3H); 13C NMR (100 MHz, DMSO-d6) δ173.07, 171.54, 169.99, 168.24, 167.24, 158.32, 158.00, 156.52, 152.34, 147.86, 145.89, 145.41, 131.56, 130.40, 129.74, 128.89, 128.54, 127.95, 127.70, 118.78, 113.98, 95.13, 75.82, 66.23, 55.53,51.76, 50.18, 38.42, 31.70, 30.41, 30.29, 29.63, 28.91, 28.82, 26.37, 22.72, 20.88, 7.54.; ESI-MS for C36H45N7O8 [M+H]+ calculated 704.3408; found 704.3485.

Transmission Electron Microscopy Measurement – Negative Stain TEM

CPT-dipeptide samples in PBS (10 mM, pH 7.4) were prepared and aged for 1 day before the measurement. For TEM studies, the samples were freshly diluted in PBS to 1 mM. Drops (10 μL) of CPT-dipeptide solutions in PBS (1 mM) were applied to carbon coated copper grids (Ted Pella, Inc.) for 2 min. After removing the excess solution with filter paper, the grid was floated on 10 μL drops of 2 wt% uranyl acetate solution (for negative stain) for 1 min. For the stability test in human serum (HS), 25 μL solutions in PBS (10 mM, pH 7.4) were diluted into 225 μL HS to make 1 mM sample concentrations in HS. The samples were then prepared after 1 hour and 24 hours post-dilution in HS. The excess solution was removed by filter paper. Drops (10 μL) of peptide solutions after incubation were applied to carbon coated copper grid for 2 min. After removing the excess solution with filter paper, the grid was floated on 10 μL drops of 2 wt% uranyl acetate for 2 min. Data were analyzed with Image pro software.

Determination of Dipeptide Stability in PBS and HS by HPLC

The lactone stability of both CPT-dipeptides, CPT, and irinotecan was measured by analytical reversed-phase HPLC (1 mL/min) under ambient temperature eluting with a linear gradient ofCH3CN/water containing 0.05M ammonium acetate in H2O, pH = 5.5~6.0. The timeline was set to0-5 min, 5-40% CH3CN; 5-20min, 40%-80% CH3CN; 20-23min, 80-95% CH3CN; 23-25min, 95-5% CH3CN.The presence of open/closed E-ring was detected by UV-Vis detector at 360 nm and the percentage of those two forms was determined by the ratio of the peak area of closed lactone ring compared with the

total area measured at each time point. HPLC traces of closed lactone form and open carboxylate form were determined by using citrate buffer (pH = 3.0) solutions and borate buffer (pH = 9.0). A solution of CPT in DMSO was prepared and mixed with either 0.01 M citrate buffer solution (pH = 3.0) and 0.02 M borate buffer solution (pH = 9.0) to obtain CPT lactone or carboxylate respectively. After 24 hours incubation at 37 °C, samples were taken from each buffer solution and tested by analytical reversed-phase HPLC.

After solutions of CPT in DMSO and irinotecan in PBS (pH = 7.4) were prepared, they were diluted to 20 μg/mL using 500 μl PBS (pH = 7.4) and 500 μl acetonitrile and incubated at 37 °C. Samples (30 μL) were injected to the HPLC at predesignated time points. CPT and irinotecan were monitored for 12 and 72 hours, respectively.
For lactone stability in PBS, solutions of dipeptide **A** and **B** in PBS (10 mM, pH = 7.4) were prepared and incubated at 37 °C. Forty microliter aliquots were taken and diluted with PBS to the desired concentration and monitored for 7 days by analytical reversed-phase HPLC. For lactone stability under basic condition, solutions of dipeptide **A** and **B** were prepared (0.2 mM) in borate buffer under pH = 9 and incubated at 37 °C for one hour, then analyzed with HPLC.

For the lactone stability in the human serum, 10 and 20 mM solutions of dipeptide **A** and **B** in PBS (pH=7.4) were prepared and aged for 1 day. The pre-aged samples in PBS were taken and diluted in human serum to 1 and 10 mM, and then incubated at 37 °C. A 10 μL

aliquot from each sample was withdrawn, diluted with 120 μL cold methanol to precipitate the protein, and centrifuged at 5000 rpm for 5 minutes. Forty microliters of supernatant were then analyzed by HPLC for lactone stability in human serum each day for 5 days.

Cell Culture and Reagents

Cytotoxicity assays, confocal microscopy, and flow cytometry were performed using the human colorectal adenocarcinoma (HT-29) cell line, human non-small cell lung cancer cell lines (A549, NCI-H460, and NCI-H23), and normal human bronchial epithelium cell line (BEAS-2b), obtained from American Type Culture Collection (ATCC, Manassas, GA). HT-29 was grown in McCoy's 5A medium supplemented with 10% fetal bovine serum, 1X penicillin/streptomycin, and incubated in a humidified 37 °C, 5% CO2 environment. CPT-dipeptide species **A** and **B** were prepared at 10 mM in sterile PBS and allowed to age 3 days prior to experiments. Immediately prior to experiments, *S*-camptothecin (95%, Sigma-Aldrich) was dissolved (10 mM) in dimethyl sulfoxide, and irinotecan hydrochloride (> 97%, Sigma-Aldrich) was dissolved (1 mM) in nanopure water.

Human non-small cell lung cancer cell lines (A549, NCI-H460, and NCI-H23) were grown in RPMI-1640 medium (Sigma Aldrich) supplemented with 10% fetal bovine serum, 1X penicillin/streptomycin, and incubated in a humidified 37°C, 5% CO2 environment. Normal human bronchial epithelium cell line (BEAS-2b) was grown in

BEGM Bronchial Epithelial Cell Growth Medium (BEGM BulletKit, Lonza). CPT-dipeptide species **A** and **B** were prepared at 10 mM in sterile PBS and allowed to age 3 days prior to experiments. Immediately prior to experiments, *S*-camptothecin (95%, Sigma-Aldrich) and irinotecan hydrochloride (> 97%, Sigma-Aldrich) was dissolved in dimethyl sulfoxide (2.5mM and 10mM, respectively).

Cytotoxicity Assay

Human colorectal adenocarcinoma (HT-29) cells were plated in 96-well plates at a density of 5 x 103 cells/well (100 μL/well) and allowed to adhere overnight. All drug stock solutions were diluted to 40 μM in complete cell culture medium and serially diluted, then 100 μL were added to each well. Cells were incubated for a further 96 hours and then assayed for viability using a MTS tetrazolium colorimetric assay (Promega). Four wells were tested per sample and concentration, and three total experiments were performed on separate days, with separate reagents each day. Viability is reported as the mean of 12 total wells per data point, and error bars represent +/- standard deviation.

Human non-small cell lung cancer cell lines (A549, NCI-H460, and NCI-H23) cells were seeded in 48 well plates (1.0 x 104 cells/well) 24 hours prior to the addition of drugs. Concentrations of drugs were 0, 0.01, 0.03, 0.1, 0.3, 1, 3, and 10 μM and cells were incubated at 37 °C under a humidified atmosphere of 5% CO2 for 96 h prior to MTT viability analysis. Absorbance was measured with SpectraMax M2 Microplate Reader (Molecular Devices) and the effects of drug activity were evaluated by determining the

50% inhibition values (IC50) as an average of three replicas. Each experiment was repeated at least 3 times.

Confocal Microscopy

Cells (HT-29) were plated at 5 x 105 cells/well on top of #1.5 glass coverslips in 6-well plates, and allowed to adhere overnight. The next day, cells were exposed to 200 μM drug for 90 minutes, and subsequently washed three times with PBS, fixed with 4% paraformaldehyde, gently permeabilized with 0.1% Triton-X 100, and stained for membrane and nuclear visualization using AlexaFluor 488-concanavalin A (Invitrogen) and TO-PRO®-3 Iodide (Invitrogen), respectively. Coverslips were mounted on glass slides using ProLong® Gold Antifade Reagent (Invitrogen) and imaged using a Carl Zeiss confocal laser scanning microscope. Fluorophores were visualized with the 405, 488, and 633 excitation lines.

Flow Cytometry

Human colorectal adenocarcinoma (HT-29) cells (5 x 105/well) were plated in 6-well plates and incubated overnight. Medium was subsequently removed, and fresh medium containing treatment (100 μM) was added. Cells were exposed to treatments for 4, 8, 12, and 24 hours, then washed three times with PBS, detached via trypsinization, and analyzed using a LSRII flow cytometer (Becton Dickinson). A UV (355 nm) laser excited camptothecin, and emission was observed through a UV450/50 bandpass filter. A total of 103 events per sample were recorded, and the data were subsequently analyzed and

plotted using FlowJo (Ashland, OR). A bifurcated gate was used on the control (untreated) cell population (99% negative for fluorescence) to calculate statistics (i.e., the percentage of cells/events exhibiting fluorescence ("uptake") above threshold values). Human non-small cell lung cancer cells (A549, NCI-H460, and NCI-H23) were seeded in 6 cm plates (0.3 x 106 cells/plate) 24 hours prior to the experiment. Concentration of CPT and its derivatives were 10 mM, and 2 mL of the drug in medium was added to cells at different time points for final incubation time of 0, 1, 3, 8, 12, and 24 hrs. Cells were washed once with PBS, and trypsinized before subjected to flow cytometry analysis (BD FACSAria III) with excitation at 355nm, and fluorescence detected at 420-470nm.

Chapter 2.2: The Self-Assembly of a Camptothecin-Lysine Nanotube

(This sub-chapter is adapted from previous publication in Bioorganic & Medicinal Chemistry Letters in 2016, my main contribution for this publication is towards the cellular / biological studies. doi:10.1016/j.bmcl.2016.04.056)

Introduction

The selective delivery of high doses of anticancer drugs to tumor sites without side effects remains as an important goal in cancer therapy.[142] Nanotechnology is emerging as a potential strategy to reduce the dose-limiting toxicity of many chemotherapeutic agents.[143-145] Linking anticancer drugs to excipient nanoscale carriers exploits the enhanced permeability and retention (EPR) effect to achieve selective transport to tumor tissue.[146, 147] This effect allows nanoscale materials to accumulate in tumor tissues via the abnormally leaky blood vessels at these sites. The majority of nanoscale materials used as inert carriers are polymers,[148] solid nanoparticles,[149] and liposomal aggregates,[150] which bind the drug via noncovalent encapsulation,[151] or covalent conjugation.[152] The drug loading level of these constructs is often limited by the size of the inert carrier, which often dominates the mass of the conjugated drug, requiring larger quantities to be administered.[153] Thus, decreasing the mass of the carrier is necessary to increase the effective drug loading of the nanomedicine. Higher drug loadings have been achieved by the multivalent attachment of the drug to carriers such as dendrimers.[116] An alternative approach creates the nanoscale carrier via the self-assembly

of a suitable derivative of the drug.[154-156] This strategy offers a potential to achieve higher loading levels by using smaller, drug-containing building blocks as precursors.[157]

Camptothecin (CPT) is a natural quinoline alkaloid with potent anti-tumor activity that functions through the inhibition of DNA topoisomerase I.[158] However, the clinical application of CPT is limited due to its poor aqueous solubility, the instability of the E-lactone ring and nonselective biodistribution.[158] CPT also undergoes lactone ring opening to form the carboxylate form, which renders the drug an inactive chemotherapeutic agent (**Figure 30**). Previously, we reported that the assembly of CPT-dipeptide conjugates produced well-defined nanotubes in PBS and human serum.[159] These nanostructures exhibited enhanced resistance to hydrolytic deactivation and showed high in vitro potency against several human cancer cell types.

Results and Discussion

In this work, we report that a smaller CPT-Lysine conjugate (A) assembles into water soluble, uniform nanotubes (**Figure 31)** having a high drug loading (~60.5%) and also exhibits favorable *in vitro* cytotoxicity and cellular uptake against several tumor cell lines. Furthermore, the potential hydrolytic breakdown products of CPT-lysine A would be succinic acid and lysine, which are both classified as 'generally recognized as safe' (GRAS) by the FDA.

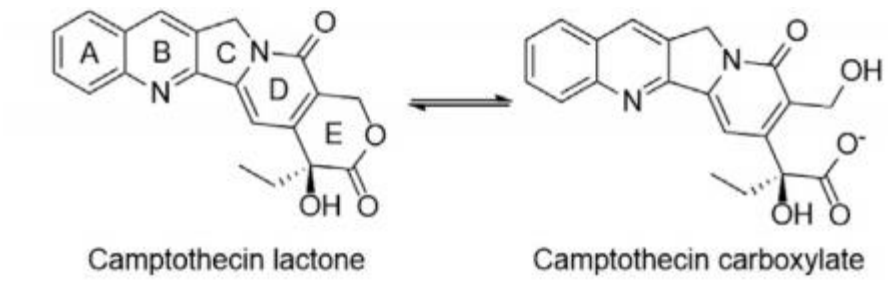

Figure 30. pH dependent hydrolysis of lactone / carboxylate form of Camptothecin.

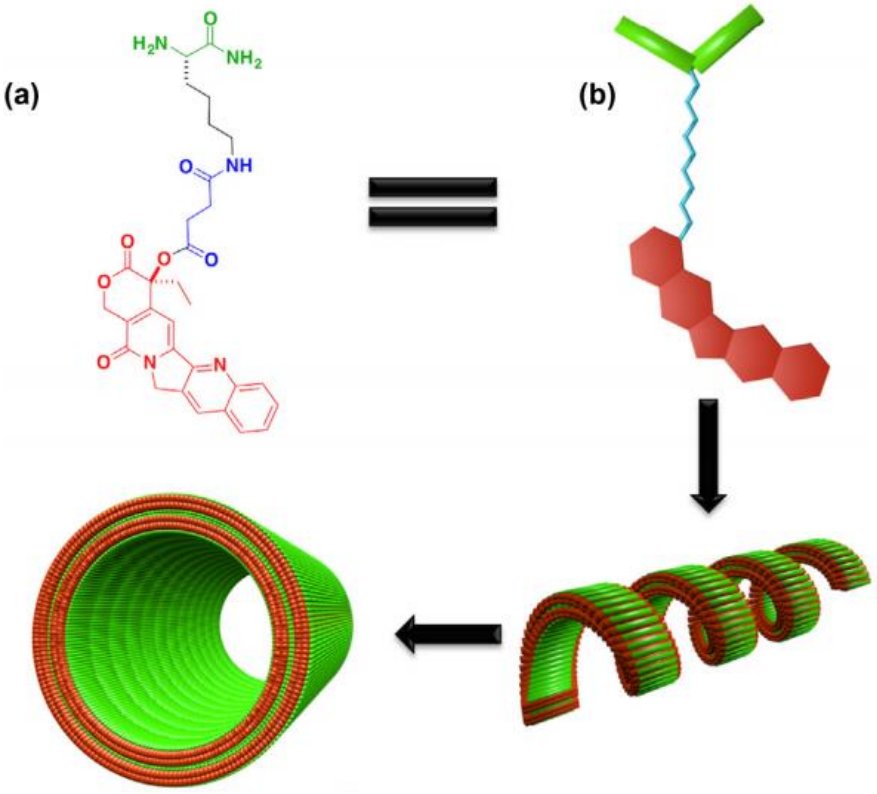

Figure 31. (a) Structure of CPT-Lysine. (b) Cartoon figure of CPT-Lysine and the progressive helical winding and nanotube formation.

CPT-Lysine A was prepared via on-resin modification of the ε-amino group of N_α-Fmoc-lysine with CPT, linked through a 20-O-succinic acid linkage[160]. In contrast to free CPT, which was insoluble in water (0.003 mg/mL),[161] CPT-Lysine A exhibited excellent aqueous solubility (5.14 mg/mL in PBS, pH = 7.4; 12.1 mg/mL in water). The self-assembly of A was explored by transmission electron microscopy (TEM) in PBS and pure water. A sample of A, incubated at 10 mM in PBS for 72 h, then diluted to 1 mM, exhibited an array of nanotubes displaying diameters ranging from 70 to 100 nm and lengths of several micrometers by TEM imaging (**Figure 32a**). When shorter incubation times were employed prior to imaging, a range of intermediates that preceded the formation of well-defined nanotubes could be observed.[162] For example, after 24 h at 10 mM, short, incompletely formed nanotubes (<500 nm) were present (**Figure 32b**). Under these conditions, partially formed nanotubes, coiled ribbons and helical tapes could be discerned in addition to the fully formed nanotubes.

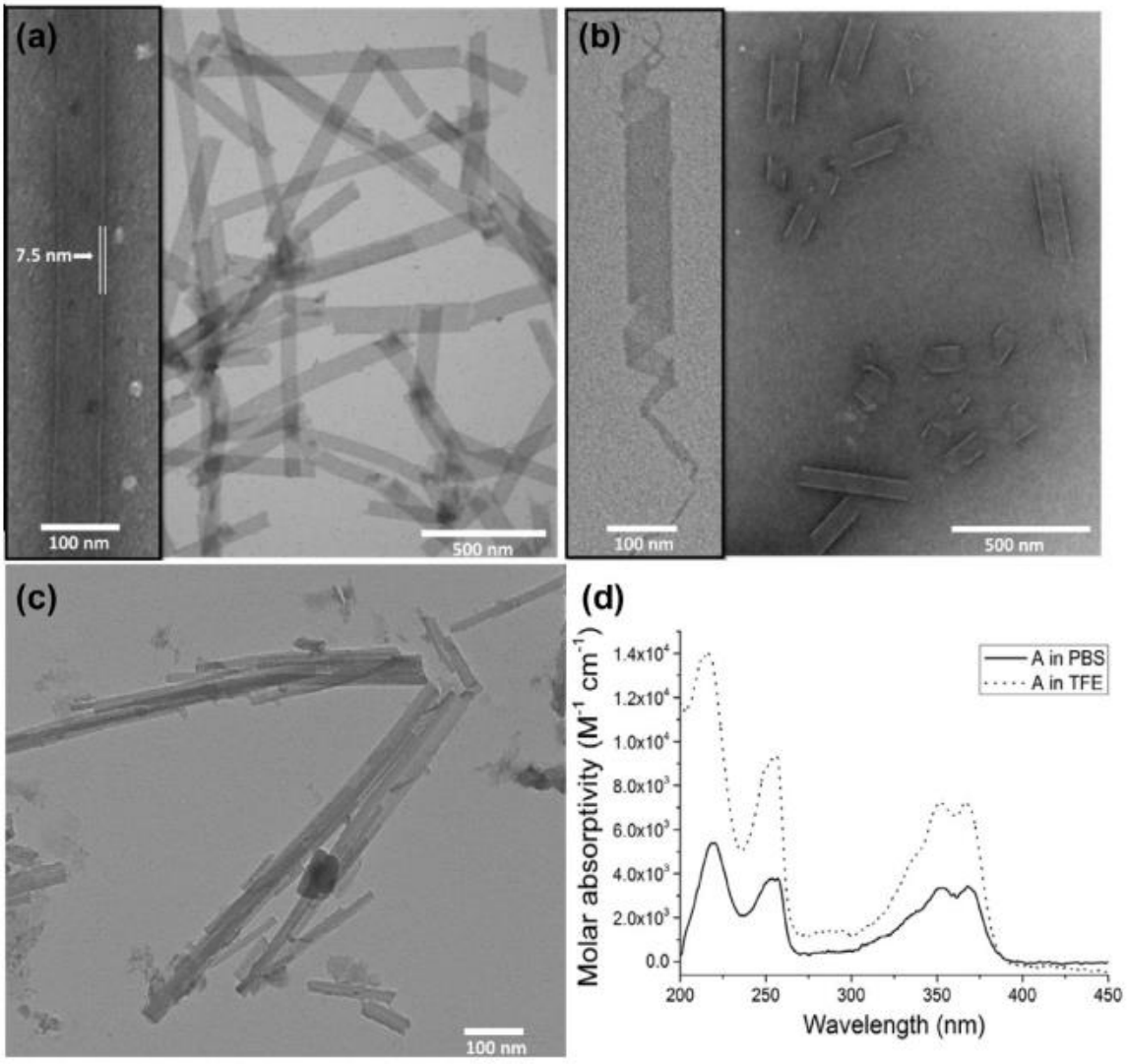

Figure 32. TEM images of CPT-Lysine in (a) PBS, 3 days, pH 7.4, (b) PBS, 1 day, pH 7.4, (c) water, 3 days, pH 7.0, (d) UV-Vis spectra in PBS and TFE.

The critical aggregation concentration (CAC) of freshly dissolved solutions of A in PBS and H_2O, prepared without pre-incubation, was 160 and 200 μM respectively,

measured using the solvochromatic dye Nile Red.[128] Solutions of A at concentrations in this range (250 μM in PBS), imaged without prior incubation at 10 mM, displayed primarily non-specific aggregation. In pure water (10 mM for 72 h, then diluted to 1 mM, pH 7), A formed parallel arrays of nanotubes with decreased diameters (40 nm) (**Figure 32c**). The aligned packing and decreased diameters of the nanotubes can be attributed to the reduced charge screening that takes place in pure water.[163]

The thickness of the nanotube walls (7.5 nm), as measured by TEM imaging, suggested a double bilayer structure comprised of 4 molecules of A in an extended conformation (1.7 nm) (**Figure 32a inset**). The zeta potential of nanotube A in PBS was 19.7 mV, due to the positive ammonium head group of A. The UV–Vis spectra of A revealed bands at 350 and 368 nm in PBS that were decreased in amplitude and slightly red-shifted compared with solutions measured in TFE, indicative of *J*-type aggregation of the CPT chromophores in PBS (**Figure 32d**). Fourier transform infrared spectra of a sample of A, prepared in PBS (20 mM), then lyophilized and re-dissolved in D_2O, exhibited a peak at 1650 cm^{-1} , indicative of the lack of any β-sheet interactions within the assembly.

The self-assembly of A sequesters the hydrophobic CPT structure within the hydrophobic regions of the nanotubes, thereby protecting the 20-O-succinyl linkage from the hydrolytic aqueous environment. Free CPT undergoes a reversible, pH-dependent ring-opening of the lactone ring in water, producing the carboxylate form, which has been shown to be toxic.[122] Although hydrolytic cleavage of the 20-O-succinyl linkage is required to produce active CPT, competing hydrolysis of the lactone ring of CPT has a

detrimental impact on its biological activity.[120] Accordingly, we explored the capability of the nanotube structure to enhance the stability of the CPT lactone and the 20-O-succinyl linkage to hydrolytic cleavage in PBS. The release of CPT from the nanotubes formed from A was measured by HPLC over one week as a function of concentration in PBS at 37 ˚C. Under these conditions, hydrolytic cleavage of 20-O-succinyl linkage produced free CPT, observed in both the lactone and carboxylate states.[164] However, the carboxylate form of A, which would be formed by CPT-lactone hydrolysis, could not be detected at any concentration or time point. In contrast, exposure of A to borate buffer at pH 9 for 6 h, produced free CPT-carboxylate and the carboxylate form of A, clearly observable by HPLC analysis (**Figure 33**).

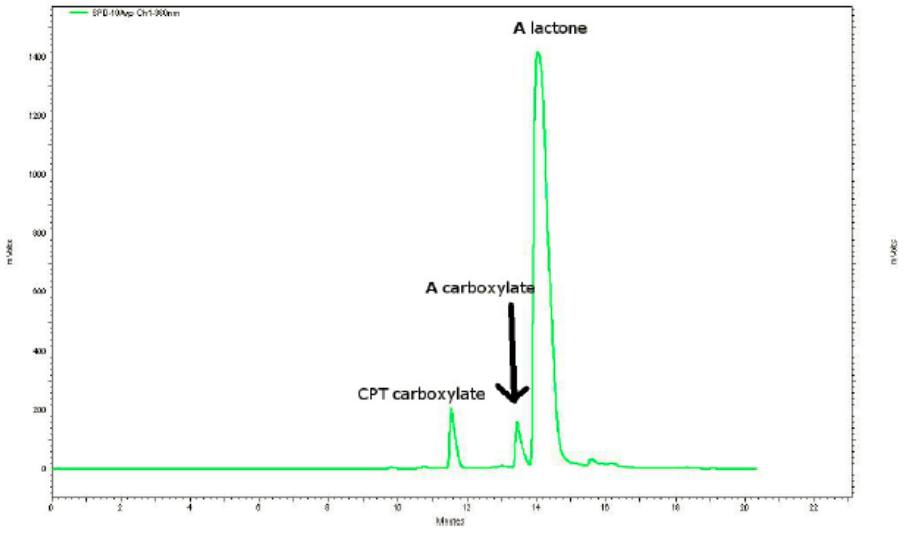

Figure 33. HPLC traces of 1mM CPT-Lysine showing release of CPT in borate buffer at 37 ˚C, flow rate = 1 ml/min, eluent acetonitrile in water 5% - 95% in 25 min.

For example, after 3 days at 1 mM in PBS, 61% of CPT was released from A, observed in both the CPT-lactone (79%) and CPT-carboxylate (21%) forms. The remainder of A (39%) was intact as the lactone without any apparent hydrolysis to the carboxylate form. Although no apparent ring-opening of A could be observed, it is not possible to exclude the possibility that ring-opening takes place prior to a more rapid cleavage of the 20-O-succinyl linkage, which would also preclude observation of A-carboxylate. The rate of hydrolytic release of CPT from A depended strongly on concentration (**Figure 34**). Accordingly, as the concentration was increased from 0.1 mM to 10 mM, the amount of free CPT progressively decreased from 70% to 4% after 30 h (**Figure 35**). These observations contrast with the hydrolytic instability of free CPT in PBS, which experiences rapid hydrolysis to the inactive carboxylate form within hours.[122]

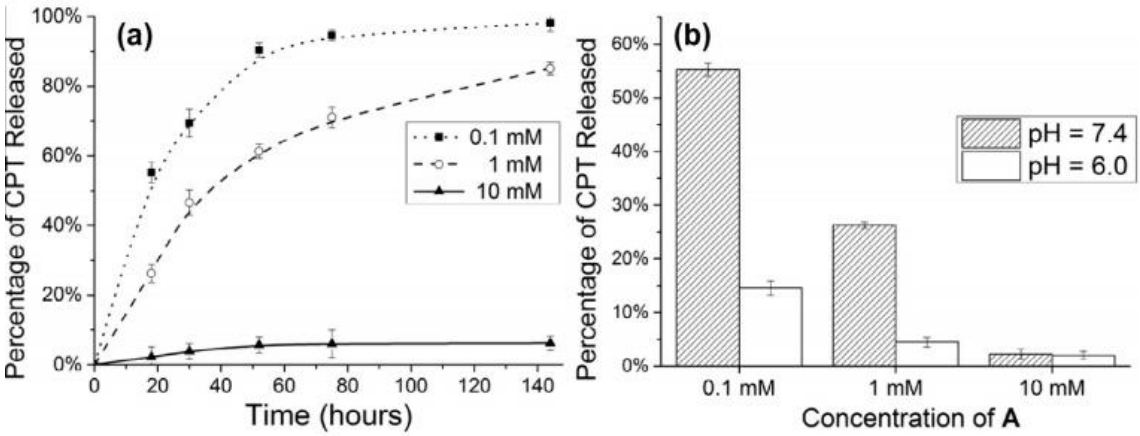

Figure 34. (a) Time vs. concentration dependent release profile of CPT from CPT-Lysine in PBS at 37 ˚C, pH 7.4 and (b) pH vs. concentration dependent release profile of CPT from CPT-Lysine in PBS (pH= 7.4) and pH = 6 at 37 ˚C after 15 h.

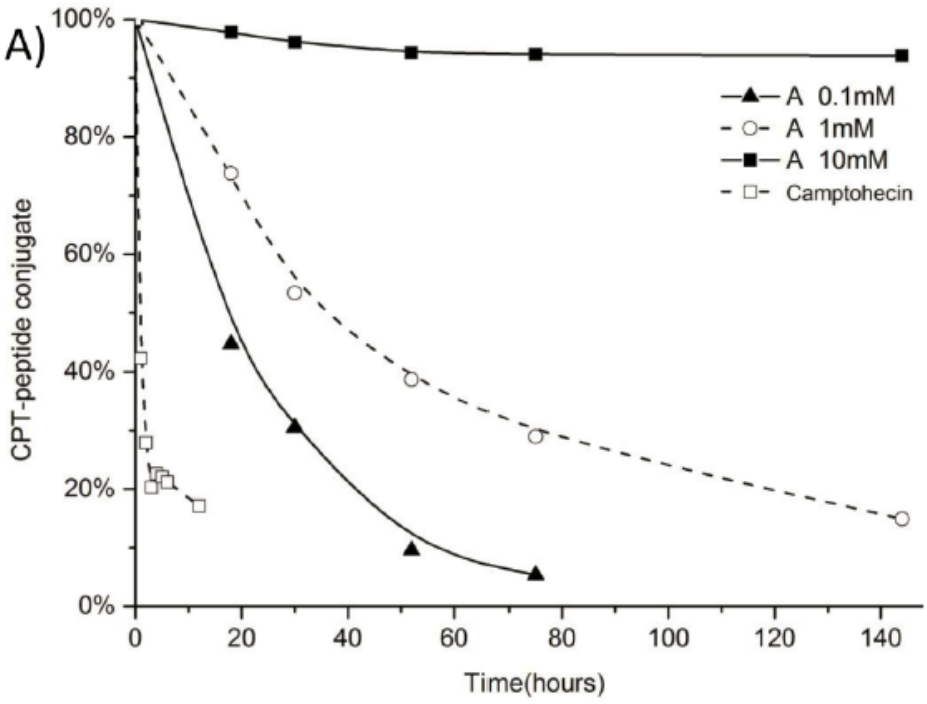

Figure 35. Overall stability of CPT-Lysine in PBS at pH 7.4 and 37 ˚C. Parental CPT undergoes lactone ring opening whereas CPT-Lysine undergoes hydrolytic release of CPT.

The CPT release rates were also studied at lower pH values to replicate the lysosomal and tumor environments, which are more acidic than normal tissues.[165] The pH of the buffer had a large impact on the rate of CPT release. For example, at 0.1 mM in PBS, whereas 55% of the CPT was released from A at pH 7.4 (37.5 ˚C), only 15% was released at pH 6.0. At 1 mM, the rate of release was 7-fold slower at pH 6.0; however, the CPT-lysine conjugate was stable at 10 mM at either pH value (**Figure 34b**). The pH

dependence of the hydrolytic cleavage of the 20-O-succinyl linkage in the nanotubes was consistent with reports of other CPT conjugates attached via a 20-O ester group.[166]

The CPT-lysine A was assessed for efficacy against human non-small cell lung cancer (NSCLC) cell lines A549, NCI-460, and NCI-H23, which were selected according to the indications of approved CPT derivative Topotecan.[167] The cytotoxic activity was assayed using MTT-assay over the course of a 96 h incubation period and the IC_{50} values were 1.12μM, 0.43μM, 0.12μM for A, and 0.35μM, 0.19μM, and 0.07μM for CPT, respectively (**Figure 36a**). CPT exhibits a roughly 2–3 fold higher potency than A in all cell lines; however, it is not used clinically due to its limited aqueous solubility and toxicity. Flow cytometry was performed with the A549 cells to monitor the cellular uptake of A, and compared with free CPT. The cellular uptake was monitored at 425 nm, after excitation at 355 nm, over a 24 h period. As shown in **Figure 36b**, CPT treated cells exhibited a larger number of fluorescent cells at longer incubations, but the uptake was similar for both A and CPT during the first 8 h. The lower cytotoxicity of A may be due to the slower cellular uptake and the gradual release of the active CPT component.

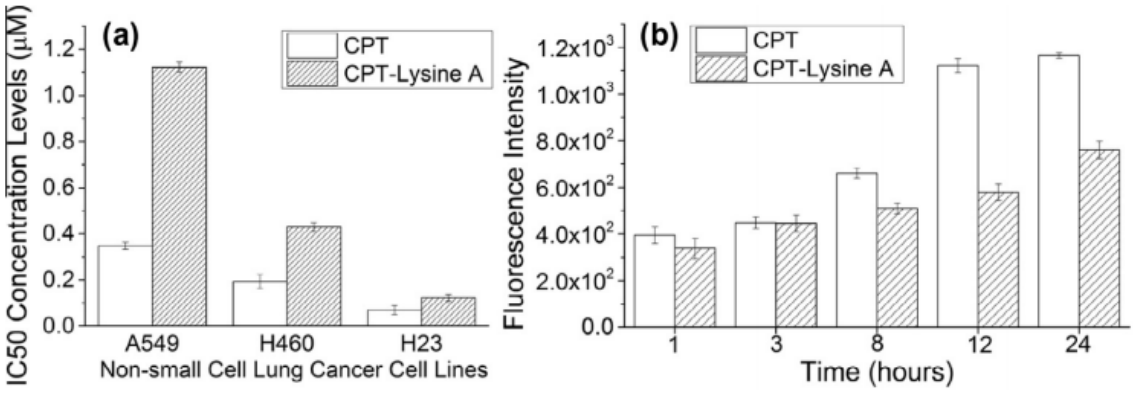

Figure 36. (a) IC_{50} values of CPT-Lysine on NSCLC A549, H460, and H23 and (b) Normalized flow cytometry results showing intracellular accumulation of CPT-Lysine compared with parental drug CPT over 24 h period.

In summary, the self-assembly and anticancer activity of a simple CPT-lysine conjugate was reported. The CPT-lysine conjugate assembles into well-defined nanotubes in PBS with diameters ranging from 70 to 100 nm. The nanotube structures provide a hydrophobic environment for the CPT segment, thereby protecting the drug from hydrolytic lactone inactivation and achieving higher aqueous solubility. Hydrolytic cleavage of the 20-O-succinyl linkage readily releases active CPT at rates that depend strongly on concentration, temperature and the pH of the solution. The tremendous stability imparted to the CPT drug linkage suggests that drug release occurs from smaller aggregates or monomeric forms of A. This possibility creates a potential to induce drug release via a triggered disassembly of the nanotube structure. This strategy also enables the creation of a nanoscale drug delivery vehicle that is comprised primarily of a low

molecular weight derivative of CPT, resulting in exceptionally high drug loadings (60.5%), aqueous solubility and increased CPT stability without the need for excipient, macromolecular carriers.

Experimental Procedure

Synthesis of NH2-K(CPT)-NH2. (CPT-Lysine A):

CPT-Lysine **A** was prepared *via* on-resin modification of the side chain.

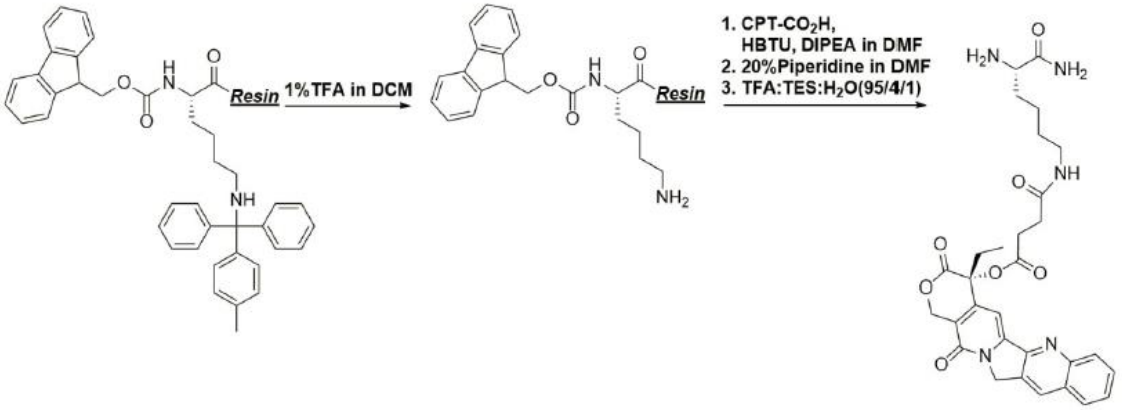

Lysine protected with Fmoc and Mtt protection groups was manually linked on rink amide resin (loading 0.80 mmol/g) using solid-phase peptide synthesis. Amide-coupling steps were accomplished with standard techniques: Fmoc-Lysine (Boc)-OH, 1,3-diisopropylcarbodiimide (DIC), and 1-hydroxybenzotriazole (HOBt) (300 mol% each relative to resin) in 1:1 DMF/DCM for 1.5 h. A solution of 20% piperidine in DMF was used for Fmoc deprotection and 2 % TFA in dichloromethane with 1% triethylsilane (TES) was used for Mtt group deprotection. A mixture of CPT-CO2H, HBTU, and DIPEA (200 mol% each relative to resin) in DMF was added to the resin. The reaction

mixture was shaken for 24 h at room temperature and then filtered through a fritted syringe. The resin was washed thoroughly (3 x DMF, 3 x CH2Cl2) and the final CPT Lysine **A** was cleaved from the resin by the treatment with TFA/water/triethylsilane (95 / 1 / 4) at room temperature for 2 h. The crude product was precipitated with cold diethyl ether and purified by reversed-phased HPLC on preparative Varian Dynamax C18 column eluting with a linear gradient of CH3CN/water containing 0.1 % TFA (10/90 to 100/0 over 30 minutes) and stored as lyophilized powers at 0 °C. Compound purity was assessed by analytical reverse-phase HPLC, and identity was confirmed using ESI-TOF mass spectrometry and NMR.

CPT-Lysine A

1H NMR (400 MHz, DMSO-d6) δ 0.86 (t, 3H, *J*= 7 Hz), 1.28-1.31 (m, 2H), 1.55-4.60 (m, 2H), 2.10 (m, 2H), 2.28 (m, 2H), 2.61-2.77 (m, 2H), 2.91-3.02 (m, 2H), 3.56-3.58 (m, 1H), 5.24 (s, 2H), 5.43 (s, 2H), 7.07 (s, 1H), 7.65 (t, 1H, *J*= 7 Hz), 7.82 (t, 1H, *J*=7 Hz), 8.10 (t, 2H, *J*= 9 Hz), 8.64 (s, 1H); 13C NMR (400 MHz, DMSO-d6) δ 7.53, 21.73, 28.63, 28.90, 29.64, 30.34, 30.54, 33.72, 50.42, 52.07, 66.41, 75.82, 95.11, 101.25, 118.80, 127.97, 128.62, 129.03, 129.78, 131.59, 145.39, 145.94, 156.53, 167.25, 170.12, 170.34, 171.61, 173.61; ESI-MS calculated for C30H33N5O7 [M+H]+ 576.2453, found 576.2460;

Experimental procedure for TEM, CAC, HPLC, and all cellular studies follow the same procedures as those in **Chapter 2.1**.

Chapter 2.3: Self-Assembly of a 5-Fluorouracil-Dipeptide Hydrogel

(This sub-chapter is adapted from previous publication in Chemical Communications in 2016, my main contribution for this publication is towards the cellular / biological studies. doi: 10.1039/c6cc01195k)

Introduction

Nanotechnology enhanced drug delivery promises a capability to favorably control the pharmacokinetics, biodistribution and efficacy of anticancer therapeutics.[145, 168] Peptide-based gelators are receiving significant interest for biomedical applications such as drug delivery,[169-171] tissue engineering,[172] biomacromolecule immobilization,[173] and regenerative medicine[174] due to their biocompatibility, injectability, and controllable formation / degradation rates. Compared with conventional polymeric hydrogels, peptide gelators are formed primarily through non-covalent interactions such as hydrophobic interactions, π-π stacking, and hydrogen bonding. The non-covalent structures of these hydrogels enables them to be formed, biodegraded and excreted *in vivo*, making them ideal as biomedical delivery vehicles.[175] The active drug can often be physically entrapped within the hydrogel matrix, but this strategy often suffers low or variable drug loading/encapsulation levels and uncontrollable release kinetics.[176]

Results and Discussion

In this work, we report a self-assembled, low molecular weight hydrogel composed entirely of a 5-fluorouracil drug conjugate organized into nanotube assemblies.[112, 177] The hydrogels maintain high drug loading levels, and exhibit slow drug release profiles controlled by the nanotube and hydrogel structures.

5-Fluorouracil (5-Fu) is an antimetabolite drug whose mechanism of action involves the irreversible inhibition of thymidylate synthase *via* competitive binding.[178, 179] It has been used as an anticancer agent against various tumors such as anal, breast, colorectal, and skin cancers—as well as for treating actinic or solar keratosis.[180, 181] Injectable hydrogel formulations offer localized delivery and sustained release profiles,[181] and have potential for the treatment of colorectal cancer.[182] Nanoscale carriers have also been reported to reduce the occurrence of acquired drug resistance (ADR),[183] which often emerges from the high doses of 5-Fu necessary in many therapeutic applications. In dermatological treatment protocols, 5-Fu is generally administered intravenously or as a ~5 wt% topical cream or ointment.[184] A low molecular weight hydrogel comprised of 5-Fu organized into nanotubes, has potential to enhance the clinical utility of 5-fluorouracil.

Dipeptides A and B were prepared using standard Fmoc/t-Bu solid-phase peptide synthesis, wherein the 5-Fu moieties were introduced by on-resin modification of the supported peptide. The design was based on previously described, di-lysine peptide motifs that effectively assembled into various nanostructures, such as nanotubes, nanobelts, and nanofibers in water. In this design, β-sheet self-assembly is driven by

hydrophobic π-π association of both the uracil and Fmoc chromophores in aqueous media.[159, 185] The tendency toward infinite β-sheet assembly into insoluble amyloid-type aggregates is opposed by the electrostatic repulsions of adjacent protonated lysines within the assembly, which also promote aqueous solubility. The 5-Fu moiety was appended at N-1 to the ε-amine of the C-terminal lysine residue *via* either a hydrolytic, self-immolative succinate (A) or a stable, acetamide linkage (B).[186] Based on the structures of A and B, the calculated drug loadings were 17.6 and 19.6%, respectively (**Figure 37**). Accordingly, hydrogels A (formed at 20 mM) and B (formed at 10 mM) contain 0.26 wt% and 0.13 wt% 5-Fu, respectively.

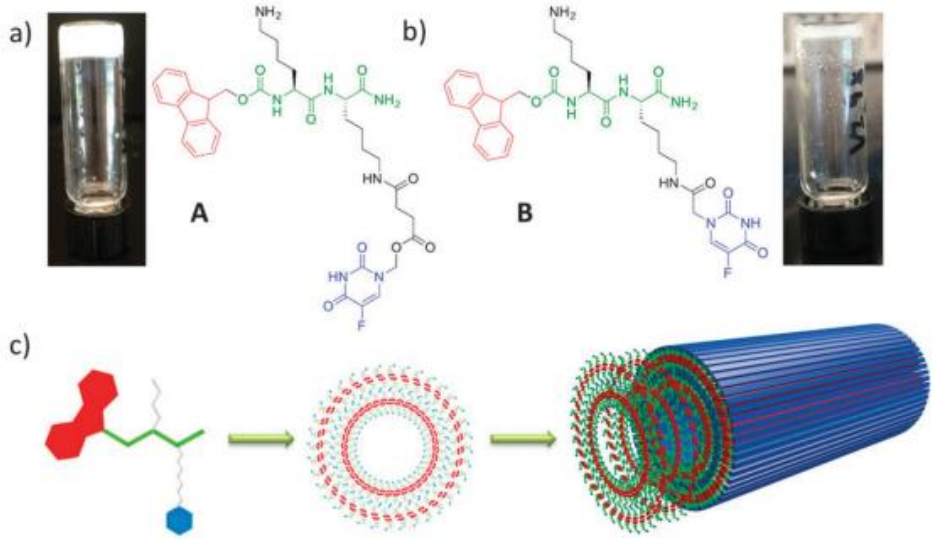

Figure 37. Structural design and self-assembly of the hydrogel compounds. (a) Dipeptide A and the hydrogel formed after aging at 20mM in PBS for 3 days; (b) dipeptide B and the hydrogel formed after aging at 10mM in PBS for 3 days; (c) cartoon depiction of

hydrogel A and its self-assembly into bilayer rings, which then stacks to form 1D nanotubes.

The hydrogelation of dipeptide conjugates A and B was studied in phosphate buffered saline (PBS, pH = 7.4). Conjugates A and B both formed clear, self-supporting hydrogels[187] after briefly sonicating (~1 min) at low concentrations (A, 20 mM; B, 10 mM) in PBS then aging for 72 h. The structure of the hydrogels formed by A and B were further studied using transmission and scanning electron microscopy (TEM and SEM) (**Figure 38**). The hydrogel formed by A consisted of a network of one-dimensional nanotubes with diameters of ~16 nm, wall thicknesses of ~4 nm and lengths of several micrometers (**Figure 38a**). The dimensions of the nanotube walls are consistent with a bilayer structure comprised of two molecules of A. Additionally, the occasional presence of intermediate ring structures with identical dimensions as the nanotubes indicated a progressive assembly process whereby an initially formed bilayer ring subsequently stacked into the nanotube (**Figure 38a, inset**).[188] The hydrogel formed by B displayed a network of nanofibers with diameters of ~10 nm (**Figure 38b**).

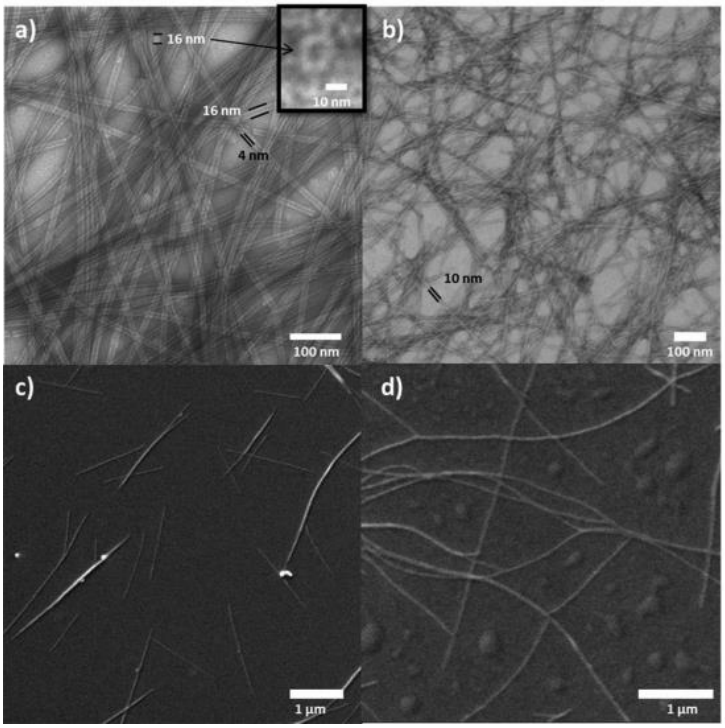

Figure 38. TEM (top) and SEM (bottom) images of dipeptide A (a and c) and B (b and d) in PBS. Samples were aged at 20mM for A and 10mM for B for 3 days at pH 7.4, and diluted to 1mM prior to preparing imaging samples.

The critical aggregation concentrations (CACs), as measured using the solvochromatic dye Nile Red,[128] of freshly dissolved solutions of A and B in PBS, prepared without pre-incubation, were 1.50 and 0.78 mM, respectively. It is noteworthy that a 0.25 mM sample of dipeptide A did not undergo gelation, only exhibiting a small degree of non-specific aggregation by TEM, incapable of encapsulating Nile Red. It is likely that these nonspecific aggregates precede the formation of the intermediate ring structures en route to the final nanotube assemblies. However, the unstable nature of the

rings, relative to the nanotubes, makes it difficult to assess the concentration at which these form in the assembly process.

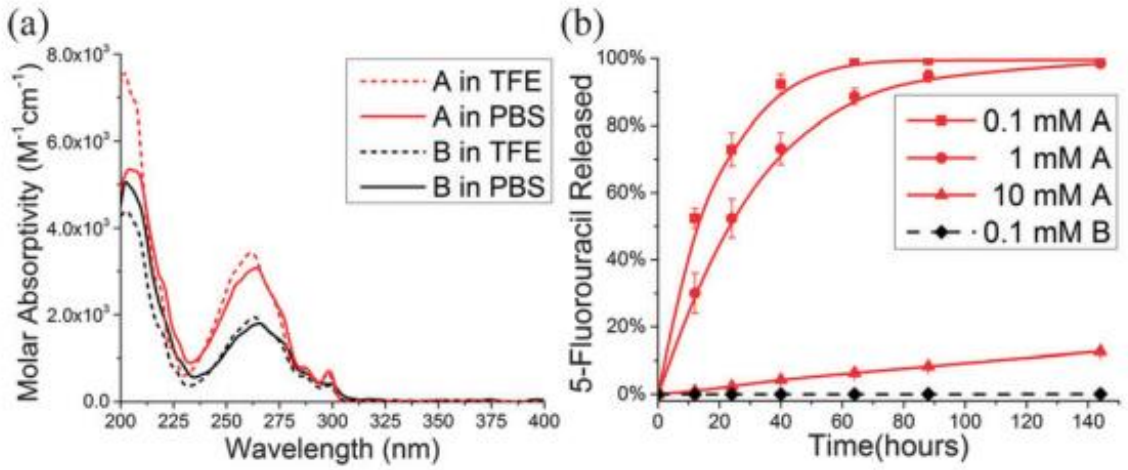

Figure 39. (a) UV-Vis spectra of dipeptide A and B in PBS and TFE, conjugates were aged at previously mentioned concentrations for 3 days and diluted to 0.25 mM prior to the experiment. (b) Release profile of 5-FU in PBS (pH = 7.4, 37 ˚C) from solutions of A and B as a function of concentration.

The broad bands exhibited by A and B in PBS at 264 nm in the ultraviolet (UV-Vis) spectra were slightly red-shifted (~2 nm), compared with the spectra in 2,2,2-trifluoroethanol (TFE), in which aggregation was minimal (**Figure 39a**). The red shifting of the absorption at 264 nm that occurs upon solvent induced assembly was indicative of *J*-type aggregation of the Fmoc chromophore within the assemblies.[189] Deconvoluted

Fourier-transform infrared (FT-IR) spectra of samples, prepared by lyophilizing the hydrogels formed in PBS then re-dissolving in D_2O (20 mM), revealed predominant bands at 1639 cm^{-1} (for A) and 1634 cm^{-1} (for B), due to the presence of β-sheet secondary structure.

Release of 5-Fu from the nanotubes takes place following hydrolytic cleavage of the acyloxymethylene linkage of A and subsequent collapse of the resultant hemiaminal intermediate.[190] The release of active drug, 5-Fu, from A and B was measured by analytical RP-HPLC over time as a function of concentration in PBS (**Figure 39b**). Whereas A readily released 5-Fu in PBS (pH 7.4) at 37.5 ˚C, B was stable under these conditions, as a consequence of the more stable acetamide linkage between the peptide and 5-Fu. At concentrations above the CAC of A, the release of 5-Fu from the nanotube was considerably slower than at concentrations below the CAC. For example, 12.6% of 5-Fu was released after 7 days when aging at 10 mM in PBS, whereas near complete release of 5-Fu was achieved after 7 days at 1 or 0.1 mM. At concentration ranges below the CAC, the rate of release was also inversely dependent on concentration, but to a lesser extent (e.g., 50% free 5-Fu released after 1 day at 1 mM, compared to 73% at 0.1 mM). As we observed previously, self-assembly slows the hydrolytic release of 5-Fu from A by sequestering the ester linkage within the hydrophobic regions of the nanotubes.[159] This observation demonstrates that self-assembly is an effective strategy to slow down the release of free drug by protecting the hydrolyzable bond from exposure to the aqueous media.

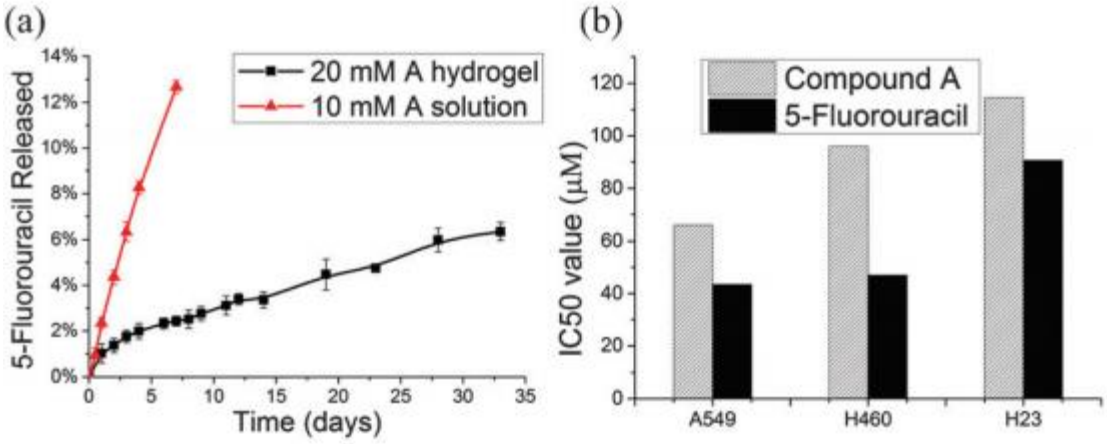

Figure 40. (a) Release profile of 5-Fu from hydrogel A compared with its solution form; (b) IC_{50} values of compound A and 5-Fu on non-small cell lung cancer cell lines A549, H460, and H23.

Next, the release of 5-Fu from hydrogel A was also determined by analytical RP-HPLC over one month. The hydrogel of A was formed in PBS (20 mM) in a cylindrical vial (15 x 45 mm), and allowed to equilibrate for 3 days, during which time 5-Fu release was insignificant. A solution of PBS (1 mL) was added on top of the hydrogel (~1 mL) without disturbing the gel. A 10 mL aliquot was then collected, replaced and analyzed for the release of 5-Fu at each time point. Compared with non-gel solutions at 10 mM, the release of 5-Fu from hydrogels was significantly slower due to the extensive self-assembly and slow diffusion within the hydrogel structure. For example, after 7 days, hydrogel A released 2.5% of 5-Fu into the top solution, while 12.6% of 5-Fu was released when aged at 10 mM without pre-gelation (**Figure 40a**). Hydrogel A was stable for over

one month, with only 6% of 5-Fu released. This result suggests hydrogel A may be used in formulations for sustained local application.

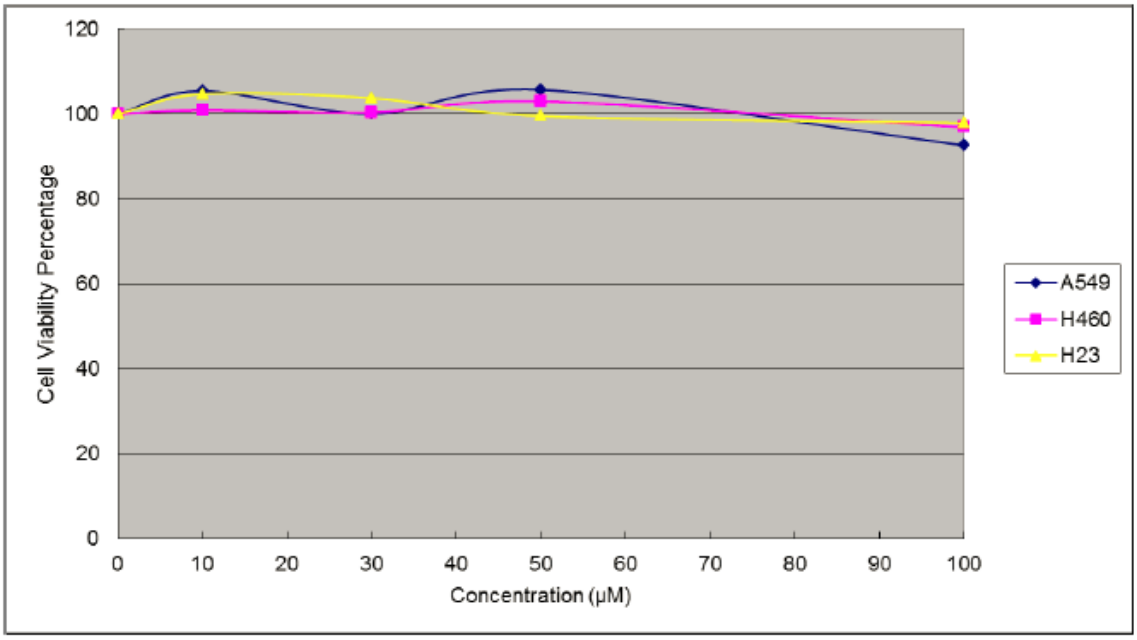

Figure 41. Cell viability study of Fmoc-KK(succinic acid) against NSCLC A549, H460, and H23. The scaffold after the release of 5-Fu exhibits no toxicity towards the cells, suggesting the toxicity observed from dipeptide A and B are solely the result of 5-Fu toxicity.

Dipeptides A and B and the parental drug 5-Fu, were assessed for their cytotoxicity against human non-small cell lung cancer cell lines A549, NCI-H460, and NCI-H23. The cytotoxic activity was assayed using the colorimetric MTT assay after a 96 hours

incubation period. The IC_{50} values were 66.1 mM, 96 mM, 114.6 mM for compound A, respectively, and 43.4 mM, 47 mM, and 90.6 mM for 5-Fu, respectively (**Figure 40b**). Dipeptide B exhibited no cytotoxicity against any of the three cell lines, as a consequence of the inability of B to release free 5-Fu. Notably, the cytotoxicity of the by-product of hydrolytic release of CPT from A, Fmoc-KK(succinic acid), was also assessed and found to have negligible impact cancer cell growth (**Figure 41**), proving that the cytotoxicity of A is from the release of 5-Fu. Overall, 5-Fu exhibits roughly 1.5 greater potency than compound A in all cell lines, likely reflecting the slower release of 5-Fu from A.

Finally, the mechanical properties of hydrogels A and B were investigated by rotational shear rheometry.[191] The hydrogels possess distinctive mechanical behavior resulting from their respective linkages to 5-Fu. Stress sweep testing (25 °C, 1.0 Hz) revealed significant differences in the linear viscoelastic regions (LVR) between the two hydrogels (hydrogel A: LVR < 0.1 Pa; hydrogel B: LVR < 10 Pa). Hydrogel A, which contains a hydrolyzable succinimidyl ester linkage to 5-Fu, exhibited two log lower storage (G') and loss (G'') moduli than hydrogel B (**Figure 42 a and b, respectively**), which lacks this flexible linker to 5-Fu and instead contains an N-acetamide linkage. Temperature sweep testing—performed by ramping the temperature from 25 °C to 80 °C, and back to 25 °C at a rate of $\pm$1 °C min^{-1} —showed that these hydrogels possess similar melting points (determined from the crossover of G' and G'') of ~75–80 °C (**Figure 42 b and c**), despite their differences in mechanical strength.[192] Hydrogels A and B behave differently upon heating and cooling. Whereas hydrogel B recovers its original mechanical strength upon cooling to < 60 °C, hydrogel A is not

thermally reversible. We suspect that the ester linkage present in hydrogel A is hydrolyzed under these conditions, which is supported by 5-Fu release studies on A that show this linkage is labile.

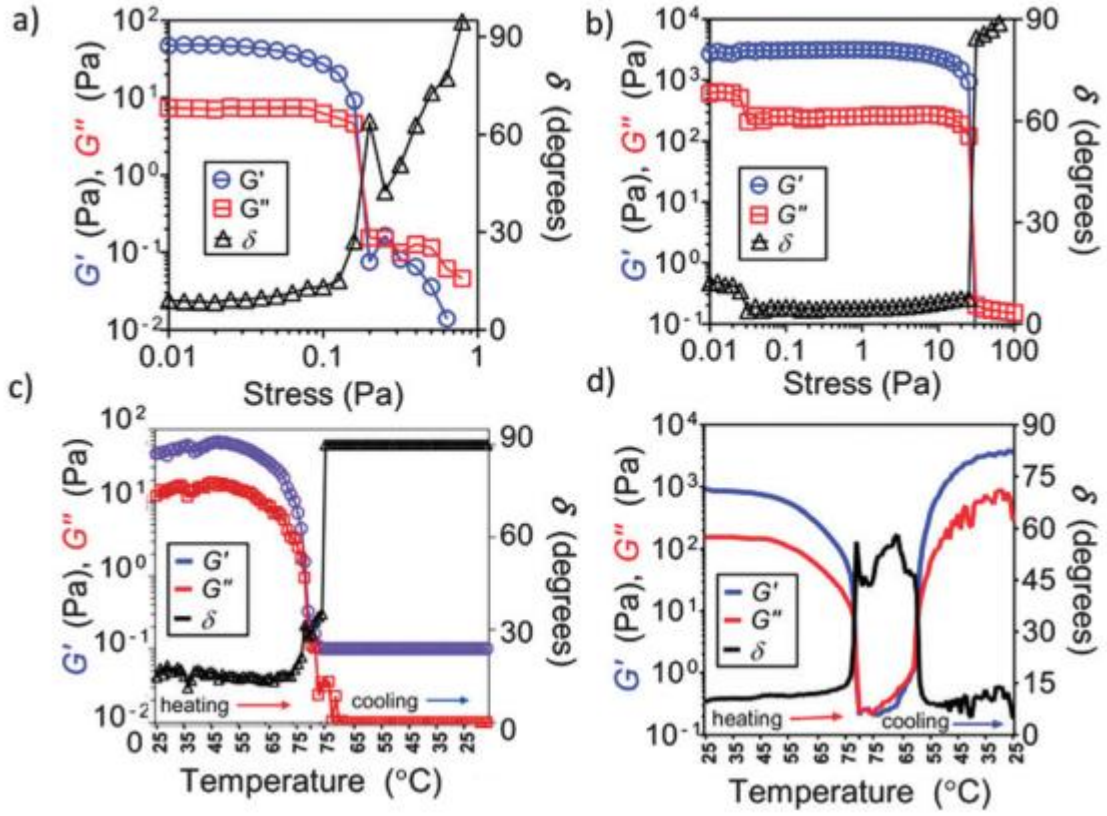

Figure 42. (a) Oscillatory stress sweep of hydrogel A at 20 mM and (b) B at 10mM , 1.0 Hz; (c) temperature sweet (heating and cooling) of hydrogels A and B, and 0.1 Pa applied oscillatory shear stress; (G' = storage modulus, G'' = loss modulus, δ = phase angle).

In summary, the 5-Fu di-lysine conjugates A and B formed hydrogels via the self-assembly of a network of nanotubes or nanofibers in PBS with diameters of 16 and 10 nm, respectively. The nanotube structures from dipeptide A provided a protective environment for 5-Fu, thereby affording a slow release of active 5-Fu depending on concentration. Furthermore, the hydrogel structure significantly reduced the release rate of 5-Fu, offering the potential for sustained local drug delivery. The cytotoxicity of A, as determined in three cancer cell lines, arose from the release of free 5-Fu, while dipeptide B, with a hydrolytically stable, N-acetamide linkage, exhibited no cytotoxicity. Additionally, oscillatory shear testing shows that the choice of linkage to the 5-Fu moiety significant impacted the strength, stability, and reversibility of the resulting hydrogels. In summary, a simple strategy to create nanostructured hydrogels for the delivery of 5-Fu based on the self-assembly of dipeptide-5-Fu conjugates has been described.

Experimental Procedure

Synthesis of Fmoc-KK(5-Fu ester)-NH_2 (A) and Fmoc-KK(5-Fu amide)-NH_2 (B)

Dipeptides **A** and **B** were prepared *via* on-resin modification of the side chain (Scheme S5). The di-lysine peptide, protected with Fmoc and Mtt groups, was manually prepared using Fmoc/t-Bu solid-phase peptide synthesis on rink amide resin (loading 0.80 mmol/g). Amide-coupling steps were accomplished with standard techniques for all amino acids: Fmoc-amino acid, 1,3-diisopropylcarbodiimide (DIC), and 1-hydroxybenzotriazole (HOBt) (300 mol% each relative to resin) in 1:1 DMF/DCM for 1.5 h. A solution of 20 % piperidine in DMF was used for Fmoc removal and 1 % TFA in dichloromethane was used for Mtt group deprotection. A mixture of 5-Fluorouracil-1-acetic acid or 5-fluorouracil-1-succinic acid, HBTU, and DIPEA (200 mol% each relative to resin) in DMF was added to the resin. The reaction mixture was shaken for 24 h at room temperature and then filtered through a fritted syringe. The resin was washed thoroughly (3 x DMF, 3 x CH2Cl2) and the final 5-Fu-peptide conjugate was cleaved from the resin by the treatment with TFA/water/triethylsilane (95/1/4) at room temperature for 2 h. The crude peptides were precipitated with cold diethyl ether and purified by reversed-phased HPLC on preparative Varian Dynamax C18 column eluting with a linear gradient of CH3CN/water containing 0.1 % TFA (10/90 to 100/0 over 30 minutes) and stored as lyophilized powers at 0°C. Peptide purity was assessed by analytical reverse-phase HPLC, and identity was confirmed using ESI-TOF mass spectrometry and NMR.

Fmoc-KK(5-Fu ester)-NH2 (Compound A) 1H NMR (400 MHz, DMSO-d6) δ 11.97 (d, 1H, *J*= 5.2 Hz), 8.08 (d,1H, *J*= 6.4 Hz), 7.90 (d, 2H, *J*= 7.6 Hz), 7.69-7.83 (m, 4H), 7.61 (s, 3H), 7.50 (d, 1H, *J*= 8.4 Hz), 7.40-7.44(t, 2H), 7.31-7.35 (t, 3H), 7.01 (s, 1H), 5.55 (s, 2H), 4.17-4.30 (m, 4H), 3.99-4.00 (m, 1H), 2.97 (d, 2H, *J*= 5.6 Hz), 2.76 (d, 2H, *J*= 5.2 Hz), 2.28-2.35 (m, 4H), 1.61-1.66 (m, 2H), 1.49-1.52 (m, 4H), 1.21-1.33 (m, 6H) ; 13C NMR (400 MHz, DMSO-d6) δ 173.50, 172.16, 171.55, 170.18, 157.51, 157.24, 155.95, 149.19, 143.87, 140.69, 129.62, 127.61, 127.06, 125.23, 120.08, 70.35, 65.58, 54.52, 52.11, 46.64, 38.67, 38.44, 31.79, 31.23, 29.99, 29.49, 28.77, 26.52, 22.61, 22.30; ESI-MS calculated for C36H45FN7O9 [M+H]+ 738.3263, found 738.2744;

Fmoc-KK(5-Fu amide)-NH2 (Compound B)1H NMR (400 MHz, DMSO-d6) δ 11.80 (d, 1H, *J*= 5.2 Hz), 8.11 (m, 1H), 7.99 (d, 1H, *J*= 6.8 Hz), 7.89 (d, 2H, *J*= 7.6 Hz), 7.79 (d, 1H, *J*= 8 Hz), 7.72 (d, 2H, *J*= 8.4 Hz), 7.69 (m, 2H), 7.50 (d, 1H, *J*= 8 Hz), 7.40-7.44 (t, 2H), 7.31-7.36 (m, 3H), 7.01 (s, 1H), 4.17-4.30 (m, 6H), 3.99-4.00 (m, 1H), 3.02-3.04 (m, 2H), 2.75-2.76 (m, 2H), 1.64-1.66 (m, 2H), 1.48-1.52 (m, 4H), 1.27-1.38 (m, 6H) ; 13C NMR (400 MHz, DMSO-d6) δ 173.50, 171.58, 166.23, 157.49, 155.98, 149.65, 143.86, 143.68, 140.69, 138.09, 130.88, 127.62, 127.06, 125.21, 120.10, 65.58, 54.42, 53.36, 52.06, 49.56, 46.63, 38.69, 31.76, 31.18, 28.64, 26.52, 22.56, 22.31; ESI-MS calculated for C33H40FN7O7 [M+H]+ 666.3051, found 666.2500;

Scanning Electron Microscopy Measurement

Scanning Electron Microscopy (SEM) was performed with FEI Nova 400 Nano SEM instrument operating at 5.0 kV. The 5-Fu-peptide samples in PBS (20 mM for **A** and 10 mM for **B**, pH 7.4) was prepared and freshly diluted from to 1 mM before the measurement. A 20 μl aliquot of the resulting solution was dried at room temperature on a copper stubs and coated with gold.

Rheology Testing

Compound **A** was prepared at 20 mM in PBS (without Ca2+ and Mg2+) and incubated at room temperature for 24 hours. Compound **B** was prepared at 10 mM in PBS (without Ca2+ and Mg2+) and incubated at room temperature for 24 h. Individual gel samples were removed from vials first using a scalpel blade, and then a curved spatula, to disengage them from the glass walls and bottom, respectively. The complex shear storage (G') and loss
(G'') moduli of these self-assembled hydrogels were then measured as a function of oscillatory stress using a rheometer (AR1000, TA Instruments, Delaware) equipped with either 40-mm aluminum parallel plate (gels in pure water) or 12-mm stainless steel parallel plate geometries.

Experimental procedure for TEM, CAC, HPLC, and all cellular studies follow the same procedures as those in **Chapter 2.1**.

References

[1] FH, C. (**1958**) On protein synthesis, *Symp Soc Exp Biol 12*, 138-163.

[2] S M Berget, C. M., P A Sharp. (**1977**) Spliced segments at the 5' terminus of adenovirus 2 late mRNA, *Proc Natl Acad Sci U S A 74*, 3171-3175.

[3] Chow LT, G. R., Broker TR, Roberts RJ. (**1977**) An amazing sequence arrangement at the 5- ends of adenovirus 2 messenger RNA, *Cell 12*, 1-8.

[4] B, W. (**1977**) DNA insertions and gene structure, *Nature 270*, 295-297.

[5] Gilbert, W., Marchionni, M., and McKnight, G. (**1986**) On the antiquity of introns, *Cell 46*, 151-153.

[6] Warner, J. R., Soeiro, R., Birnboim, H. C., Girard, M., and Darnell, J. E. (**1966**) Rapidly labeled HeLa cell nuclear RNA, *J. Mol. Biol. 19*, 349-361.

[7] Webb, C. H., Riccitelli, N. J., Ruminski, D. J., and Luptak, A. (**2009**) Widespread occurrence of self-cleaving ribozymes, *Science 326*, 953.

[8] de la Pena, M., and Garcia-Robles, I. (**2010**) Intronic hammerhead ribozymes are ultraconserved in the human genome, *EMBO Rep 11*, 711-716.

[9] Peterson, S. M., Thompson, J. A., Ufkin, M. L., Sathyanarayana, P., Liaw, L., and Congdon, C. B. (**2014**) Common features of microRNA target prediction tools, *Front Genet 5*, 23.

[10] Lee, R. C., Feinbaum, R. L., and Ambros, V. (**1993**) The C. elegans heterochronic gene lin-4 encodes small RNAs with antisense complementarity to lin-14, *Cell 75*, 843-854.

[11] Reinhart, B. J., Slack, F. J., Basson, M., Pasquinelli, A. E., Bettinger, J. C., Rougvie, A. E., Horvitz, H. R., and Ruvkun, G. (**2000**) The 21-nucleotide let-7 RNA regulates developmental timing in Caenorhabditis elegans, *Nature 403*, 901-906.

[12] Pasquinelli, A. E., Reinhart, B. J., Slack, F., Martindale, M. Q., Kuroda, M. I., Maller, B., Hayward, D. C., Ball, E. E., Degnan, B., Muller, P., Spring, J., Srinivasan, A., Fishman, M., Finnerty, J., Corbo, J., Levine, M., Leahy, P., Davidson, E., and Ruvkun, G. (**2000**) Conservation of the sequence and temporal expression of let-7 heterochronic regulatory RNA, *Nature 408*, 86-89.

[13] Cooper, G. M., and Brown, C. D. (**2008**) Qualifying the relationship between sequence conservation and molecular function, *Genome Res 18*, 201-205.

[14] John, B., Enright, A. J., Aravin, A., Tuschl, T., Sander, C., and Marks, D. S. (**2004**) Human MicroRNA targets, *PLoS Biol 2*, e363.

[15] Lewis, B. P., Burge, C. B., and Bartel, D. P. (**2005**) Conserved seed pairing, often flanked by adenosines, indicates that thousands of human genes are microRNA targets, *Cell 120*, 15-20.
[16] Fabian, M. R., Sonenberg, N., and Filipowicz, W. (**2010**) Regulation of mRNA translation and stability by microRNAs, *Annu. Rev. Biochem 79*, 351-379.
[17] Schnall-Levin, M., Rissland, O. S., Johnston, W. K., Perrimon, N., Bartel, D. P., and Berger, B. (**2011**) Unusually effective microRNA targeting within repeat-rich coding regions of mammalian mRNAs, *Genome Res 21*, 1395-1403.
[18] Winter, J., Jung, S., Keller, S., Gregory, R. I., and Diederichs, S. (**2009**) Many roads to maturity: microRNA biogenesis pathways and their regulation, *Nat Cell Biol 11*, 228-234.
[19] Ha, M., and Kim, V. N. (**2014**) Regulation of microRNA biogenesis, *Nat Rev Mol Cell Biol 15*, 509-524.
[20] Macfarlane, L. A., and Murphy, P. R. (**2010**) MicroRNA: Biogenesis, Function and Role in Cancer, *Curr Genomics 11*, 537-561.
[21] Kim, V. N. (**2005**) MicroRNA biogenesis: coordinated cropping and dicing, *Nat Rev Mol Cell Biol 6*, 376-385.
[22] Okamura, K., Phillips, M. D., Tyler, D. M., Duan, H., Chou, Y. T., and Lai, E. C. (**2008**) The regulatory activity of microRNA* species has substantial influence on microRNA and 3' UTR evolution, *Nat Struct Mol Biol 15*, 354-363.
[23] Lytle, J. R., Yario, T. A., and Steitz, J. A. (**2007**) Target mRNAs are repressed as efficiently by microRNA-binding sites in the 5' UTR as in the 3' UTR, *Proc Natl Acad Sci U S A 104*, 9667-9672.
[24] Carthew, R. W., and Sontheimer, E. J. (**2009**) Origins and Mechanisms of miRNAs and siRNAs, *Cell 136*, 642-655.
[25] Wu, L., and Belasco, J. G. (**2008**) Let me count the ways: mechanisms of gene regulation by miRNAs and siRNAs, *Mol Cell 29*, 1-7.
[26] Eulalio, A., Huntzinger, E., and Izaurralde, E. (**2008**) Getting to the root of miRNA-mediated gene silencing, *Cell 132*, 9-14.
[27] Filipowicz, W., Bhattacharyya, S. N., and Sonenberg, N. (**2008**) Mechanisms of post-transcriptional regulation by microRNAs: are the answers in sight?, *Nat Rev Genet 9*, 102-114.
[28] Kim, V. N., Han, J., and Siomi, M. C. (**2009**) Biogenesis of small RNAs in animals, *Nat Rev Mol Cell Biol 10*, 126-139.
[29] Fire, A., Xu, S., Montgomery, M. K., Kostas, S. A., Driver, S. E., and Mello, C. C. (**1998**) Potent and specific genetic interference by double-stranded RNA in Caenorhabditis elegans, *Nature 391*, 806-811.
[30] Ozcan, G., Ozpolat, B., Coleman, R. L., Sood, A. K., and Lopez-Berestein, G. (**2015**) Preclinical and clinical development of siRNA-based therapeutics, *Adv Drug Deliv Rev 87*, 108-119.
[31] Bobbin, M. L., and Rossi, J. J. (**2016**) RNA Interference (RNAi)-Based Therapeutics: Delivering on the Promise?, *Annu Rev Pharmacol Toxicol 56*, 103-122.

[32] Lin, S., and Gregory, R. I. (**2015**) MicroRNA biogenesis pathways in cancer, *Nat Rev Cancer 15*, 321-333.
[33]
[34] Chidambaram, M., Manavalan, R., and Kathiresan, K. (**2011**) Nanotherapeutics to overcome conventional cancer chemotherapy limitations, *J Pharm Pharm Sci 14*, 67-77.
[35] Gelperina, S., Kisich, K., Iseman, M. D., and Heifets, L. (**2005**) The potential advantages of nanoparticle drug delivery systems in chemotherapy of tuberculosis, *Am J Respir Crit Care Med 172*, 1487-1490.
[36] Jain, R. K., and Stylianopoulos, T. (**2010**) Delivering nanomedicine to solid tumors, *Nat Rev Clin Oncol 7*, 653-664.
[37] Min, Y., Caster, J. M., Eblan, M. J., and Wang, A. Z. (**2015**) Clinical Translation of Nanomedicine, *Chem. Rev. 115*, 11147-11190.
[38] Opalinska, J. B., and Gewirtz, A. M. (**2002**) Nucleic-acid therapeutics: basic principles and recent applications, *Nat Rev Drug Discov 1*, 503-514.
[39] Lam, J. K., Chow, M. Y., Zhang, Y., and Leung, S. W. (**2015**) siRNA Versus miRNA as Therapeutics for Gene Silencing, *Mol Ther Nucleic Acids 4*, e252.
[40] Mansoori, B., Sandoghchian Shotorbani, S., and Baradaran, B. (**2014**) RNA interference and its role in cancer therapy, *Adv Pharm Bull 4*, 313-321.
[41] Wang, Z., Rao, D. D., Senzer, N., and Nemunaitis, J. (**2011**) RNA interference and cancer therapy, *Pharm. Res. 28*, 2983-2995.
[42] Filleur, S., Courtin, A., Ait-Si-Ali, S., Guglielmi, J., Merle, C., Harel-Bellan, A., Clezardin, P., and Cabon, F. (**2003**) SiRNA-mediated inhibition of vascular endothelial growth factor severely limits tumor resistance to antiangiogenic thrombospondin-1 and slows tumor vascularization and growth, *Cancer Res 63*, 3919-3922.
[43] Shen, J., Samul, R., Silva, R. L., Akiyama, H., Liu, H., Saishin, Y., Hackett, S. F., Zinnen, S., Kossen, K., Fosnaugh, K., Vargeese, C., Gomez, A., Bouhana, K., Aitchison, R., Pavco, P., and Campochiaro, P. A. (**2006**) Suppression of ocular neovascularization with siRNA targeting VEGF receptor 1, *Gene Ther 13*, 225-234.
[44] Dorn, G., Patel, S., Wotherspoon, G., Hemmings-Mieszczak, M., Barclay, J., Natt, F. J., Martin, P., Bevan, S., Fox, A., Ganju, P., Wishart, W., and Hall, J. (**2004**) siRNA relieves chronic neuropathic pain, *Nucleic Acids Res. 32*, e49.
[45] Alvarado, V., and Scholthof, H. B. (**2009**) Plant responses against invasive nucleic acids: RNA silencing and its suppression by plant viral pathogens, *Semin Cell Dev Biol 20*, 1032-1040.
[46] Croce, C. M. (**2009**) Causes and consequences of microRNA dysregulation in cancer, *Nat Rev Genet 10*, 704-714.
[47] Park, C. Y., Choi, Y. S., and McManus, M. T. (**2010**) Analysis of microRNA knockouts in mice, *Hum Mol Genet 19*, R169-175.
[48] Leonardo, T. R., Schultheisz, H. L., Loring, J. F., and Laurent, L. C. (**2012**) The functions of microRNAs in pluripotency and reprogramming, *Nat Cell Biol 14*, 1114-1121.

[49] Bracken, C. P., Gregory, P. A., Khew-Goodall, Y., and Goodall, G. J. (**2009**) The role of microRNAs in metastasis and epithelial-mesenchymal transition, *Cell Mol Life Sci 66*, 1682-1699.
[50] Fernandez-Valverde, S. L., Taft, R. J., and Mattick, J. S. (**2011**) MicroRNAs in beta-cell biology, insulin resistance, diabetes and its complications, *Diabetes 60*, 1825-1831.
[51] Bredy, T. W., Lin, Q., Wei, W., Baker-Andresen, D., and Mattick, J. S. (**2011**) MicroRNA regulation of neural plasticity and memory, *Neurobiol Learn Mem 96*, 89-94.
[52] Czauderna, F., Fechtner, M., Dames, S., Aygun, H., Klippel, A., Pronk, G. J., Giese, K., and Kaufmann, J. (**2003**) Structural variations and stabilising modifications of synthetic siRNAs in mammalian cells, *Nucleic Acids Res. 31*, 2705-2716.
[53] Miele, E., Spinelli, G. P., Miele, E., Di Fabrizio, E., Ferretti, E., Tomao, S., and Gulino, A. (**2012**) Nanoparticle-based delivery of small interfering RNA: challenges for cancer therapy, *Int J Nanomedicine 7*, 3637-3657.
[54] Gantier, M. P., McCoy, C. E., Rusinova, I., Saulep, D., Wang, D., Xu, D., Irving, A. T., Behlke, M. A., Hertzog, P. J., Mackay, F., and Williams, B. R. (**2011**) Analysis of microRNA turnover in mammalian cells following Dicer1 ablation, *Nucleic Acids Res. 39*, 5692-5703.
[55] Chen, Y., Gao, D. Y., and Huang, L. (**2015**) In vivo delivery of miRNAs for cancer therapy: challenges and strategies, *Adv Drug Deliv Rev 81*, 128-141.
[56] Liu, N., Ding, H., Vanderheyden, J. L., Zhu, Z., and Zhang, Y. (**2007**) Radiolabeling small RNA with technetium-99m for visualizing cellular delivery and mouse biodistribution, *Nucl Med Biol 34*, 399-404.
[57] Thomas, C. E., Ehrhardt, A., and Kay, M. A. (**2003**) Progress and problems with the use of viral vectors for gene therapy, *Nat Rev Genet 4*, 346-358.
[58] Price, C., and Chen, J. (**2014**) MicroRNAs in Cancer Biology and Therapy: Current Status and Perspectives, *Genes Dis 1*, 53-63.
[59] Pegtel, D. M., Cosmopoulos, K., Thorley-Lawson, D. A., van Eijndhoven, M. A., Hopmans, E. S., Lindenberg, J. L., de Gruijl, T. D., Wurdinger, T., and Middeldorp, J. M. (**2010**) Functional delivery of viral miRNAs via exosomes, *Proc Natl Acad Sci U S A 107*, 6328-6333.
[60] Pouton, C. W., and Seymour, L. W. (**2001**) Key issues in non-viral gene delivery1PII of original article: S0169-409X(98)00048-9. The article was originally published in Advanced Drug Delivery Reviews 34 (1998) 3–19.1, *Advanced Drug Delivery Reviews 46*, 187-203.
[61] Yang, N. (**2015**) An overview of viral and nonviral delivery systems for microRNA, *Int J Pharm Investig 5*, 179-181.
[62] Zhang, Y., Wang, Z., and Gemeinhart, R. A. (**2013**) Progress in microRNA delivery, *J Control Release 172*, 962-974.
[63] de Antonellis, P., Medaglia, C., Cusanelli, E., Andolfo, I., Liguori, L., De Vita, G., Carotenuto, M., Bello, A., Formiggini, F., Galeone, A., De Rosa, G., Virgilio, A., Scognamiglio, I., Sciro, M., Basso, G., Schulte, J. H., Cinalli, G., Iolascon, A., and Zollo, M. (**2011**) MiR-34a targeting of Notch ligand delta-like 1 impairs

CD15+/CD133+ tumor-propagating cells and supports neural differentiation in medulloblastoma, *PLoS One 6*, e24584.
[64] Wiggins, J. F., Ruffino, L., Kelnar, K., Omotola, M., Patrawala, L., Brown, D., and Bader, A. G. (**2010**) Development of a lung cancer therapeutic based on the tumor suppressor microRNA-34, *Cancer Res 70*, 5923-5930.
[65] Boussif, O., Lezoualch, F., Zanta, M. A., Mergny, M. D., Scherman, D., Demeneix, B., and Behr, J. P. (**1995**) A Versatile Vector for Gene and Oligonucleotide Transfer into Cells in Culture and in-Vivo - Polyethylenimine, *P Natl Acad Sci USA 92*, 7297-7301.
[66] Takeshita, F., Minakuchi, Y., Nagahara, S., Honma, K., Sasaki, H., Hirai, K., Teratani, T., Namatame, N., Yamamoto, Y., Hanai, K., Kato, T., Sano, A., and Ochiya, T. (**2005**) Efficient delivery of small interfering RNA to bone-metastatic tumors by using atelocollagen in vivo, *Proc Natl Acad Sci U S A 102*, 12177-12182.
[67] Garzon, R., Marcucci, G., and Croce, C. M. (**2010**) Targeting microRNAs in cancer: rationale, strategies and challenges, *Nat Rev Drug Discov 9*, 775-789.
[68] Pecot, C. V., Calin, G. A., Coleman, R. L., Lopez-Berestein, G., and Sood, A. K. (**2011**) RNA interference in the clinic: challenges and future directions, *Nat Rev Cancer 11*, 59-67.
[69] Trang, P., Wiggins, J. F., Daige, C. L., Cho, C., Omotola, M., Brown, D., Weidhaas, J. B., Bader, A. G., and Slack, F. J. (**2011**) Systemic delivery of tumor suppressor microRNA mimics using a neutral lipid emulsion inhibits lung tumors in mice, *Mol Ther 19*, 1116-1122.
[70] Torchilin, V. P. (**2010**) Passive and active drug targeting: drug delivery to tumors as an example, *Handb. Exp. Pharmacol.*, 3-53.
[71] Kumar Khanna, V. (**2012**) Targeted delivery of nanomedicines, *ISRN Pharmacol 2012*, 571394.
[72] Bartlett, D. W., and Davis, M. E. (**2007**) Physicochemical and biological characterization of targeted, nucleic acid-containing nanoparticles, *Bioconjug Chem 18*, 456-468.
[73] Pirollo, K. F., and Chang, E. H. (**2008**) Does a targeting ligand influence nanoparticle tumor localization or uptake?, *Trends Biotechnol. 26*, 552-558.
[74] Kirpotin, D. B., Drummond, D. C., Shao, Y., Shalaby, M. R., Hong, K., Nielsen, U. B., Marks, J. D., Benz, C. C., and Park, J. W. (**2006**) Antibody targeting of long-circulating lipidic nanoparticles does not increase tumor localization but does increase internalization in animal models, *Cancer Res 66*, 6732-6740.
[75] Mikhail, A. S., and Allen, C. (**2009**) Block copolymer micelles for delivery of cancer therapy: transport at the whole body, tissue and cellular levels, *J Control Release 138*, 214-223.
[76] Y. Matsumura, H. M. (**1986**) A new concept for macromolecular therapeutics in cancer chemotherapy: mechanism of tumoritropic accumulation of proteins and the antitumor agent SMANCS, *Cancer Res 46*, 6387-6392.
[77] Bae, Y. H., and Park, K. (**2011**) Targeted drug delivery to tumors: myths, reality and possibility, *J Control Release 153*, 198-205.

[78] Kim, S. H., and Parquette, J. R. (**2012**) A model for the controlled assembly of semiconductor peptides, *Nanoscale 4*, 6940-6947.
[79] Yoo, H., Jung, H., Kim, S. A., and Mok, H. (**2014**) Multivalent comb-type aptamer-siRNA conjugates for efficient and selective intracellular delivery, *Chem Commun (Camb) 50*, 6765-6767.
[80] Greish, K. (**2010**) Enhanced permeability and retention (EPR) effect for anticancer nanomedicine drug targeting, *Methods Mol Biol 624*, 25-37.
[81] Perez-Herrero, E., and Fernandez-Medarde, A. (**2015**) Advanced targeted therapies in cancer: Drug nanocarriers, the future of chemotherapy, *Eur J Pharm Biopharm 93*, 52-79.
[82] Dreher, M. R., Liu, W., Michelich, C. R., Dewhirst, M. W., Yuan, F., and Chilkoti, A. (**2006**) Tumor vascular permeability, accumulation, and penetration of macromolecular drug carriers, *J Natl Cancer Inst 98*, 335-344.
[83] Maeda, H., Nakamura, H., and Fang, J. (**2013**) The EPR effect for macromolecular drug delivery to solid tumors: Improvement of tumor uptake, lowering of systemic toxicity, and distinct tumor imaging in vivo, *Adv Drug Deliv Rev 65*, 71-79.
[84] Maeda, H. (**2001**) The enhanced permeability and retention (EPR) effect in tumor vasculature: the key role of tumor-selective macromolecular drug targeting, *Adv. Enzyme Regul. 41*, 189-207.
[85] Hashizume, H., Baluk, P., Morikawa, S., McLean, J. W., Thurston, G., Roberge, S., Jain, R. K., and McDonald, D. M. (**2000**) Openings between Defective Endothelial Cells Explain Tumor Vessel Leakiness, *The American Journal of Pathology 156*, 1363-1380.
[86] Matsumura, Y., and Maeda, H. (**1986**) A new concept for macromolecular therapeutics in cancer chemotherapy: mechanism of tumoritropic accumulation of proteins and the antitumor agent smancs, *Cancer Res 46*, 6387-6392.
[87] Gabizon, A., Catane, R., Uziely, B., Kaufman, B., Safra, T., Cohen, R., Martin, F., Huang, A., and Barenholz, Y. (**1994**) Prolonged circulation time and enhanced accumulation in malignant exudates of doxorubicin encapsulated in polyethylene-glycol coated liposomes, *Cancer Res 54*, 987-992.
[88] Venturoli, D., and Rippe, B. (**2005**) Ficoll and dextran vs. globular proteins as probes for testing glomerular permselectivity: effects of molecular size, shape, charge, and deformability, *Am J Physiol Renal Physiol 288*, F605-613.
[89] Plank, C., Mechtler, K., Szoka, F. C., Jr., and Wagner, E. (**1996**) Activation of the complement system by synthetic DNA complexes: a potential barrier for intravenous gene delivery, *Hum Gene Ther 7*, 1437-1446.
[90] Bustin, S. A., Benes, V., Nolan, T., and Pfaffl, M. W. (**2005**) Quantitative real-time RT-PCR--a perspective, *J Mol Endocrinol 34*, 597-601.
[91] Pfaffl, M. W. (**2004**) Quantification strategies in real-time PCR, *AZ of quantitative PCR 1*, 89-113.
[92] Livak, K. J., and Schmittgen, T. D. (**2001**) Analysis of relative gene expression data using real-time quantitative PCR and the 2(-Delta Delta C(T)) Method, *Methods 25*, 402-408.

[93] Thomas, P., and Smart, T. G. (**2005**) HEK293 cell line: a vehicle for the expression of recombinant proteins, *J. Pharmacol. Toxicol. Methods 51*, 187-200.
[94] Stepanenko, A. A., and Dmitrenko, V. V. (**2015**) HEK293 in cell biology and cancer research: phenotype, karyotype, tumorigenicity, and stress-induced genome-phenotype evolution, *Gene 569*, 182-190.
[95] Zhao, M., Yang, H., Jiang, X., Zhou, W., Zhu, B., Zeng, Y., Yao, K., and Ren, C. (**2008**) Lipofectamine RNAiMAX: an efficient siRNA transfection reagent in human embryonic stem cells, *Mol Biotechnol 40*, 19-26.
[96] Cardarelli, F., Digiacomo, L., Marchini, C., Amici, A., Salomone, F., Fiume, G., Rossetta, A., Gratton, E., Pozzi, D., and Caracciolo, G. (**2016**) The intracellular trafficking mechanism of Lipofectamine-based transfection reagents and its implication for gene delivery, *Sci Rep 6*, 25879.
[97] Dalby, B., Cates, S., Harris, A., Ohki, E. C., Tilkins, M. L., Price, P. J., and Ciccarone, V. C. (**2004**) Advanced transfection with Lipofectamine 2000 reagent: primary neurons, siRNA, and high-throughput applications, *Methods 33*, 95-103.
[98] Cui, S., Zhang, S., Chen, H., Wang, B., Zhao, Y., and Zhi, D. (**2012**) The Mechanism of Lipofectamine 2000 Mediated Transmembrane Gene Delivery, *Engineering 04*, 172-175.
[99] Filion, M. C., and Phillips, N. C. (**1997**) Toxicity and immunomodulatory activity of liposomal vectors formulated with cationic lipids toward immune effector cells, *Biochimica et Biophysica Acta (BBA) - Biomembranes 1329*, 345-356.
[100] Mayhew, E., Ito, M., and Lazo, R. (**1987**) Toxicity of non-drug-containing liposomes for cultured human cells, *Experimental Cell Research 171*, 195-202.
[101] Campbell, P. I. (**1983**) Toxicity of Some Charged Lipids Used in Liposome Preparations, *Cytobios 37*, 21-26.
[102] Xiong, F., Mi, Z., and Gu, N. (**2011**) Cationic liposomes as gene delivery system: transfection efficiency and new application, *Pharmazie 66*, 158-164.
[103] Zubillaga-Guerrero, M. I., Alarcon-Romero Ldel, C., Illades-Aguiar, B., Flores-Alfaro, E., Bermudez-Morales, V. H., Deas, J., and Peralta-Zaragoza, O. (**2015**) MicroRNA miR-16-1 regulates CCNE1 (cyclin E1) gene expression in human cervical cancer cells, *Int J Clin Exp Med 8*, 15999-16006.
[104] Rivas, M. A., Venturutti, L., Huang, Y. W., Schillaci, R., Huang, T. H., and Elizalde, P. V. (**2012**) Downregulation of the tumor-suppressor miR-16 via progestin-mediated oncogenic signaling contributes to breast cancer development, *Breast Cancer Res 14*, R77.
[105] Xia, Y., Tian, J., and Chen, X. (**2016**) Effect of surface properties on liposomal siRNA delivery, *Biomaterials 79*, 56-68.
[106] Cho, K., Wang, X., Nie, S., Chen, Z. G., and Shin, D. M. (**2008**) Therapeutic nanoparticles for drug delivery in cancer, *Clin Cancer Res 14*, 1310-1316.
[107] Janib, S. M., Moses, A. S., and MacKay, J. A. (**2010**) Imaging and drug delivery using theranostic nanoparticles, *Adv Drug Deliv Rev 62*, 1052-1063.
[108] Boncel, S., Zajac, P., and Koziol, K. K. (**2013**) Liberation of drugs from multi-wall carbon nanotube carriers, *J Control Release 169*, 126-140.

[109] Ji, S. R., Liu, C., Zhang, B., Yang, F., Xu, J., Long, J., Jin, C., Fu, D. L., Ni, Q. X., and Yu, X. J. (**2010**) Carbon nanotubes in cancer diagnosis and therapy, *Biochim. Biophys. Acta 1806*, 29-35.
[110] Schleich, N., Sibret, P., Danhier, P., Ucakar, B., Laurent, S., Muller, R. N., Jerome, C., Gallez, B., Preat, V., and Danhier, F. (**2013**) Dual anticancer drug/superparamagnetic iron oxide-loaded PLGA-based nanoparticles for cancer therapy and magnetic resonance imaging, *Int. J. Pharm. 447*, 94-101.
[111] Song, Z., Liu, H., Shen, J., and Chen, X. (**2013**) A molecular hydrogel of a camptothecin derivative, *Biomater. Sci. 1*, 190-193.
[112] Cheetham, A. G., Zhang, P., Lin, Y. A., Lock, L. L., and Cui, H. (**2013**) Supramolecular nanostructures formed by anticancer drug assembly, *J. Am. Chem. Soc. 135*, 2907-2910.
[113] Davis, M. E., and Brewster, M. E. (**2004**) Cyclodextrin-based pharmaceutics: past, present and future, *Nat Rev Drug Discov 3*, 1023-1035.
[114] Chang, D. K., Chiu, C. Y., Kuo, S. Y., Lin, W. C., Lo, A., Wang, Y. P., Li, P. C., and Wu, H. C. (**2009**) Antiangiogenic targeting liposomes increase therapeutic efficacy for solid tumors, *J. Biol. Chem. 284*, 12905-12916.
[115] Shen, Y., Jin, E., Zhang, B., Murphy, C. J., Sui, M., Zhao, J., Wang, J., Tang, J., Fan, M., Van Kirk, E., and Murdoch, W. J. (**2010**) Prodrugs forming high drug loading multifunctional nanocapsules for intracellular cancer drug delivery, *J. Am. Chem. Soc. 132*, 4259-4265.
[116] Kaminskas, L. M., McLeod, V. M., Porter, C. J., and Boyd, B. J. (**2012**) Association of chemotherapeutic drugs with dendrimer nanocarriers: an assessment of the merits of covalent conjugation compared to noncovalent encapsulation, *Mol Pharm 9*, 355-373.
[117] Standley, S. M., Toft, D. J., Cheng, H., Soukasene, S., Chen, J., Raja, S. M., Band, V., Band, H., Cryns, V. L., and Stupp, S. I. (**2010**) Induction of cancer cell death by self-assembling nanostructures incorporating a cytotoxic peptide, *Cancer Res 70*, 3020-3026.
[118] Pizzolato, J. F., and Saltz, L. B. (**2003**) The camptothecins, *The Lancet 361*, 2235-2242.
[119] Lesueur-Ginot, L., Demarquay, D., Kiss, R., Kasprzyk, P. G., Dassonneville, L., Bailly, C., Camara, J., Lavergne, O., and Bigg, D. C. (**1999**) Homocamptothecin, an E-ring modified camptothecin with enhanced lactone stability, retains topoisomerase I-targeted activity and antitumor properties, *Cancer Res 59*, 2939-2943.
[120] Hertzberg, R. P., Caranfa, M. J., Holden, K. G., Jakas, D. R., Gallagher, G., Mattern, M. R., Mong, S. M., Bartus, J. O. L., Johnson, R. K., and Kingsbury, W. D. (**1989**) Modification of the hydroxylactone ring of camptothecin: inhibition of mammalian topoisomerase I and biological activity, *J. Med. Chem. 32*, 715-720.
[121] Fassberg, J., and Stella, V. J. (**1992**) A kinetic and Mechanistic Study of the Hydrolysis of Camptothecin and Some Analogues, *J. Pharm. Sci. 81*, 676-684.
[122] Burke, T. G., and Mi, Z. (**1994**) The structural basis of camptothecin interactions with human serum albumin: impact on drug stability, *J. Med. Chem. 37*, 40-46.

[123] Paranjpe, P. V., Chen, Y., Kholodovych, V., Welsh, W., Stein, S., and Sinko, P. J. (**2004**) Tumor-targeted bioconjugate based delivery of camptothecin: design, synthesis and in vitro evaluation, *J Control Release 100*, 275-292.
[124] Shao, H., Nguyen, T., Romano, N. C., Modarelli, D. A., and Parquette, J. R. (**2009**) Self-Assembly of 1-D n-Type Nanostructures Based on Naphthalene Diimide-Appended Dipeptides, *J. Am. Chem. Soc. 131*, 16374-+.
[125] Shao, H., Lockman, J. W., and Parquette, J. R. (**2007**) Coupled conformational equilibria in beta-sheet peptide-dendron conjugates, *J. Am. Chem. Soc. 129*, 1884-+.
[126] Safavy, A., Georg, G. I., Vander Velde, D., Raisch, K. P., Safavy, K., Carpenter, M., Wang, W., Bonner, J. A., Khazaeli, M. B., and Buchsbaum, D. J. (**2004**) Site-specifically traced drug release and biodistribution of a paclitaxel-antibody conjugate toward improvement of the linker structure, *Bioconjug Chem 15*, 1264-1274.
[127] Shao, H., Gao, M., Kim, S. H., Jaroniec, C. P., and Parquette, J. R. (**2011**) Aqueous Self-Assembly of L-Lysine-Based Amphiphiles into 1D n-Type Nanotubes, *Chemistry - A European Journal 17*, 12882-12885.
[128] Stuart, M. C. A., van de Pas, J. C., and Engberts, J. B. F. N. (**2005**) The use of Nile Red to monitor the aggregation behavior in ternary surfactant-water-organic solvent systems, *J. Phys. Org. Chem. 18*, 929-934.
[129] Lin, R., Cheetham, A. G., Zhang, P., Lin, Y. A., and Cui, H. (**2013**) Supramolecular filaments containing a fixed 41% paclitaxel loading, *Chem Commun (Camb) 49*, 4968-4970.
[130] Chirico, G., Collini, M., Olivini, F., Zamai, M., Frigerio, E., and Caiolfa, V. R. (**2004**) Aggregation properties of a HPMA-camptothecin copolymer in isotonic solutions, *Biophys. Chem. 110*, 281-295.
[131] Miyazawa, T., and Blout, E. R. (**1961**) The Infrared Spectra of Polypeptides in Various Conformations: Amide I and II Bands1, *J. Am. Chem. Soc. 83*, 712-719.
[132] Nabiev, I., Fleury, F., Kudelina, I., Pommier, Y., Charton, F., Riou, J.-F., Alix, A. J. P., and Manfait, M. (**1998**) Spectroscopic and Biochemical Characterisation of Self-Aggregates Formed by Antitumor Drugs of the Camptothecin Family, *Biochem. Pharmacol. 55*, 1163-1174.
[133] Beretta, G. L., and Zunino, F. (**2007**) Relevance of extracellular and intracellular interactions of camptothecins as determinants of antitumor activity, *Biochem. Pharmacol. 74*, 1437-1444.
[134] Foghandersen, N., Bjerrum, P. J., and Siggaardandersen, O. (**1993**) Ionic Binding, Net Charge, and Donnan Effect of Human Serum-Albumin as a Function of Ph, *Clin. Chem. 39*, 48-52.
[135] Schaffler, M., Sousa, F., Wenk, A., Sitia, L., Hirn, S., Schleh, C., Haberl, N., Violatto, M., Canovi, M., Andreozzi, P., Salmona, M., Bigini, P., Kreyling, W. G., and Krol, S. (**2014**) Blood protein coating of gold nanoparticles as potential tool for organ targeting, *Biomaterials 35*, 3455-3466.
[136] Li, Q.-Y., Zu, Y.-G., Shi, R.-Z., and Yao, L.-P. (**2006**) Review Camptothecin: Current Perspectives, *Current Medicinal Chemistry 13*, 2021-2039.

[137] Mathijssen, R. H., van Alphen, R. J., Verweij, J., Loos, W. J., Nooter, K., Stoter, G., and Sparreboom, A. (**2001**) Clinical pharmacokinetics and metabolism of irinotecan (CPT-11), *Clin Cancer Res 7*, 2182-2194.
[138] Zhang, J. A., Xuan, T., Parmar, M., Ma, L., Ugwu, S., Ali, S., and Ahmad, I. (**2004**) Development and characterization of a novel liposome-based formulation of SN-38, *Int. J. Pharm. 270*, 93-107.
[139] Rothenberg, M. L., Kuhn, J. G., Burris, H. A., 3rd, Nelson, J., Eckardt, J. R., Tristan-Morales, M., Hilsenbeck, S. G., Weiss, G. R., Smith, L. S., Rodriguez, G. I., and et al. (**1993**) Phase I and pharmacokinetic trial of weekly CPT-11, *J Clin Oncol 11*, 2194-2204.
[140] Rothenberg, M. L., Kuhn, J. G., Schaaf, L. J., Rodriguez, G. I., Eckhardt, S. G., Villalona-Calero, M. A., Rinaldi, D. A., Hammond, L. A., Hodges, S., Sharma, A., Elfring, G. L., Petit, R. G., Locker, P. K., Miller, L. L., and von Hoff, D. D. (**2001**) Phase I dose-finding and pharmacokinetic trial of irinotecan (CPT-11) administered every two weeks, *Ann Oncol 12*, 1631-1641.
[141] Kawato, Y., Aonuma, M., Hirota, Y., Kuga, H., and Sato, K. (**1991**) Intracellular roles of SN-38, a metabolite of the camptothecin derivative CPT-11, in the antitumor effect of CPT-11, *Cancer Res 51*, 4187-4191.
[142] He, Q., and Shi, J. (**2014**) MSN anti-cancer nanomedicines: chemotherapy enhancement, overcoming of drug resistance, and metastasis inhibition, *Adv. Mater. 26*, 391-411.
[143] Faraji, A. H., and Wipf, P. (**2009**) Nanoparticles in cellular drug delivery, *Bioorg. Med. Chem. 17*, 2950-2962.
[144] Gao, Z., Ming, D., Xiao, L., and Wang, H. (**2012**) Scale-Adaptive Feature Points Extraction and Dual-Scale Based High-Precision Image Registration, 45-50.
[145] Devadasu, V. R., Bhardwaj, V., and Kumar, M. N. (**2013**) Can controversial nanotechnology promise drug delivery?, *Chem. Rev. 113*, 1686-1735.
[146] Fang, J., Nakamura, H., and Maeda, H. (**2011**) The EPR effect: Unique features of tumor blood vessels for drug delivery, factors involved, and limitations and augmentation of the effect, *Adv Drug Deliv Rev 63*, 136-151.
[147] Torchilin, V. (**2011**) Tumor delivery of macromolecular drugs based on the EPR effect, *Adv Drug Deliv Rev 63*, 131-135.
[148] Cheng, J., Khin, K. T., Jensen, G. S., Liu, A., and Davis, M. E. (**2003**) Synthesis of linear, beta-cyclodextrin-based polymers and their camptothecin conjugates, *Bioconjug Chem 14*, 1007-1017.
[149] Chen, Y., Chen, H., Zeng, D., Tian, Y., Chen, F., Feng, J., and Shi, J. (**2010**) Core/shell structured hollow mesoporous nanocapsules: a potential platform for simultaneous cell imaging and anticancer drug delivery, *ACS Nano 4*, 6001-6013.
[150] Ke, X., Ng, V. W., Ono, R. J., Chan, J. M., Krishnamurthy, S., Wang, Y., Hedrick, J. L., and Yang, Y. Y. (**2014**) Role of non-covalent and covalent interactions in cargo loading capacity and stability of polymeric micelles, *J Control Release 193*, 9-26.
[151] Morgan, M. T., Nakanishi, Y., Kroll, D. J., Griset, A. P., Carnahan, M. A., Wathier, M., Oberlies, N. H., Manikumar, G., Wani, M. C., and Grinstaff, M. W. (**2006**)

Dendrimer-encapsulated camptothecins: increased solubility, cellular uptake, and cellular retention affords enhanced anticancer activity in vitro, *Cancer Res 66*, 11913-11921.
[152] Shi, M., Ho, K., Keating, A., and Shoichet, M. S. (**2009**) Doxorubicin-Conjugated Immuno-Nanoparticles for Intracellular Anticancer Drug Delivery, *Adv. Funct. Mater. 19*, 1689-1696.
[153] Yurkovetskiy, A. V., and Fram, R. J. (**2009**) XMT-1001, a novel polymeric camptothecin pro-drug in clinical development for patients with advanced cancer, *Adv Drug Deliv Rev 61*, 1193-1202.
[154] Baek, K., Hwang, I., Roy, I., Shetty, D., and Kim, K. (**2015**) Self-assembly of nanostructured materials through irreversible covalent bond formation, *Acc. Chem. Res. 48*, 2221-2229.
[155] Kim, S. M., Park, B. K., Jung, B. D., and Kim, H. C. (**2015**) First record of Cosmocephalus obvelatus (Acuariidae) in common gulls (Larus canus) from Gangneung, Korea, *Korean J Parasitol 53*, 101-104.
[156] Hu, X., Hu, J., Tian, J., Ge, Z., Zhang, G., Luo, K., and Liu, S. (**2013**) Polyprodrug amphiphiles: hierarchical assemblies for shape-regulated cellular internalization, trafficking, and drug delivery, *J. Am. Chem. Soc. 135*, 17617-17629.
[157] Pei, Q., Hu, X., Li, Z., Xie, Z., and Jing, X. (**2015**) Small molecular nanomedicines made from a camptothecin dimer containing a disulfide bond, *RSC Adv. 5*, 81499-81501.
[158] Pommier, Y. (**2006**) Topoisomerase I inhibitors: camptothecins and beyond, *Nat Rev Cancer 6*, 789-802.
[159] Kim, S. H., Kaplan, J. A., Sun, Y., Shieh, A., Sun, H. L., Croce, C. M., Grinstaff, M. W., and Parquette, J. R. (**2015**) The Self-Assembly of Anticancer Camptothecin-Dipeptide Nanotubes: A Minimalistic and High Drug Loading Approach to Increased Efficacy, *Chem-Eur J 21*, 101-105.
[160] Greenwald, R. (**1998**) Camptothecin-20-PEG ester transport forms: the effect of spacer groups on antitumor activity, *Biorg. Med. Chem. 6*, 551-562.
[161] Saha, S. C., Patel, D., Rahman, S., and Savva, M. (**2013**) Physicochemical characterization, solubilization, and stabilization of 9-nitrocamptothecin using pluronic block copolymers, *J. Pharm. Sci. 102*, 3653-3665.
[162] Shao, H., Gao, M., Kim, S. H., Jaroniec, C. P., and Parquette, J. R. (**2011**) Aqueous Self-Assembly of L-Lysine-Based Amphiphiles into 1D n-Type Nanotubes, *Chem-Eur J 17*, 12882-12885.
[163] Dong, H., Paramonov, S. E., Aulisa, L., Bakota, E. L., and Hartgerink, J. D. (**2007**) Self-assembly of multidomain peptides: balancing molecular frustration controls conformation and nanostructure, *J. Am. Chem. Soc. 129*, 12468-12472.
[164] Zhao, H., Lee, C., Sai, P., Choe, Y. H., Boro, M., Pendri, A., Guan, S., and Greenwald, R. B. (**2000**) 20-O-Acylcamptothecin Derivatives: Evidence for Lactone Stabilization, *The Journal of Organic Chemistry 65*, 4601-4606.
[165] Bareford, L. M., and Swaan, P. W. (**2007**) Endocytic mechanisms for targeted drug delivery, *Adv Drug Deliv Rev 59*, 748-758.

[166] Cheng, J., Khin, K. T., and Davis, M. E. (**2004**) Antitumor Activity of β-Cyclodextrin Polymer−Camptothecin Conjugates, *Molecular Pharmaceutics 1*, 183-193.
[167] O'Brien, M., Eckardt, J., and Ramlau, R. (**2007**) Recent advances with topotecan in the treatment of lung cancer, *Oncologist 12*, 1194-1204.
[168] Gao, Z., Zhang, L., and Sun, Y. (**2012**) Nanotechnology applied to overcome tumor drug resistance, *J Control Release 162*, 45-55.
[169] Branco, M. C., and Schneider, J. P. (**2009**) Self-assembling materials for therapeutic delivery, *Acta Biomater 5*, 817-831.
[170] Skilling, K. J., Citossi, F., Bradshaw, T. D., Ashford, M., Kellam, B., and Marlow, M. (**2014**) Insights into low molecular mass organic gelators: a focus on drug delivery and tissue engineering applications, *Soft Matter 10*, 237-256.
[171] Wang, H., and Yang, Z. (**2012**) Short-peptide-based molecular hydrogels: novel gelation strategies and applications for tissue engineering and drug delivery, *Nanoscale 4*, 5259-5267.
[172] Cheng, T. Y., Chen, M. H., Chang, W. H., Huang, M. Y., and Wang, T. W. (**2013**) Neural stem cells encapsulated in a functionalized self-assembling peptide hydrogel for brain tissue engineering, *Biomaterials 34*, 2005-2016.
[173] Ha, W., Meng, X.-W., Li, Q., Fan, M.-M., Peng, S.-L., Ding, L.-S., Tian, X., Zhang, S., and Li, B.-J. (**2010**) Self-assembly hollow nanosphere for enzyme encapsulation, *Soft Matter 6*, 1405.
[174] Kisiday, J., Jin, M., Kurz, B., Hung, H., Semino, C., Zhang, S., and Grodzinsky, A. J. (**2002**) Self-assembling peptide hydrogel fosters chondrocyte extracellular matrix production and cell division: implications for cartilage tissue repair, *Proc Natl Acad Sci U S A 99*, 9996-10001.
[175] Koutsopoulos, S., Unsworth, L. D., Nagai, Y., and Zhang, S. (**2009**) Controlled release of functional proteins through designer self-assembling peptide nanofiber hydrogel scaffold, *Proc Natl Acad Sci U S A 106*, 4623-4628.
[176] Li, Y., Lokitz, B. S., Armes, S. P., and McCormick, C. L. (**2006**) Synthesis of Reversible Shell Cross-Linked Micelles for Controlled Release of Bioactive Agents†, *Macromolecules 39*, 2726-2728.
[177] Lock, L. L., LaComb, M., Schwarz, K., Cheetham, A. G., Lin, Y.-a., Zhang, P., and Cui, H. (**2013**) Self-assembly of natural and synthetic drug amphiphiles into discrete supramolecular nanostructures, *Faraday Discuss. 166*, 285.
[178] Grem, J. L. (**2000**) *Investigational New Drugs 18*, 299-313.
[179] Longley, D. B., Harkin, D. P., and Johnston, P. G. (**2003**) 5-fluorouracil: mechanisms of action and clinical strategies, *Nat Rev Cancer 3*, 330-338.
[180] Carethers, J. M., Smith, E. J., Behling, C. A., Nguyen, L., Tajima, A., Doctolero, R. T., Cabrera, B. L., Goel, A., Arnold, C. A., Miyai, K., and Boland, C. R. (**2004**) Use of 5-fluorouracil and survival in patients with microsatellite-unstable colorectal cancer, *Gastroenterology 126*, 394-401.
[181] Krawtchenko, N., Roewert-Huber, J., Ulrich, M., Mann, I., Sterry, W., and Stockfleth, E. (**2007**) A randomised study of topical 5% imiquimod vs. topical 5-fluorouracil vs. cryosurgery in immunocompetent patients with actinic keratoses:

a comparison of clinical and histological outcomes including 1-year follow-up, *Br J Dermatol 157 Suppl 2*, 34-40.
[182] Wu, X., He, C., Wu, Y., and Chen, X. (**2016**) Synergistic therapeutic effects of Schiff's base cross-linked injectable hydrogels for local co-delivery of metformin and 5-fluorouracil in a mouse colon carcinoma model, *Biomaterials 75*, 148-162.
[183] Chen, L., She, X., Wang, T., He, L., Shigdar, S., Duan, W., and Kong, L. (**2015**) Overcoming acquired drug resistance in colorectal cancer cells by targeted delivery of 5-FU with EGF grafted hollow mesoporous silica nanoparticles, *Nanoscale 7*, 14080-14092.
[184] Perrett, C. M., McGregor, J. M., Warwick, J., Karran, P., Leigh, I. M., Proby, C. M., and Harwood, C. A. (**2007**) Treatment of post-transplant premalignant skin disease: a randomized intrapatient comparative study of 5-fluorouracil cream and topical photodynamic therapy, *Br J Dermatol 156*, 320-328.
[185] Kim, S. H., and Parquette, J. R. (**2012**) A model for the controlled assembly of semiconductor peptides, *Nanoscale 4*, 6940-6947.
[186] Cai, T. B., Tang, X., Nagorski, J., Brauschweiger, P. G., and Wang, P. G. (**2003**) Synthesis and cytotoxicity of 5-fluorouracil/diazeniumdiolate conjugates, *Biorg. Med. Chem. 11*, 4971-4975.
[187] Sreenivasachary, N., and Lehn, J. M. (**2005**) Gelation-driven component selection in the generation of constitutional dynamic hydrogels based on guanine-quartet formation, *Proc Natl Acad Sci U S A 102*, 5938-5943.
[188] Shao, H., Seifert, J., Romano, N. C., Gao, M., Helmus, J. J., Jaroniec, C. P., Modarelli, D. A., and Parquette, J. R. (**2010**) Amphiphilic Self-Assembly of an n-Type Nanotube, *Angew Chem Int Edit 49*, 7688-7691.
[189] Würthner, F., Thalacker, C., Diele, S., and Tschierske, C. (**2001**) FluorescentJ-type Aggregates and Thermotropic Columnar Mesophases of Perylene Bisimide Dyes, *Chemistry 7*, 2245-2253.
[190] Ouyang, L., He, D., Zhang, J., He, G., Jiang, B., Wang, Q., Chen, Z., Pan, J., Li, Y., and Guo, L. (**2011**) Selective bone targeting 5-fluorouracil prodrugs: synthesis and preliminary biological evaluation, *Bioorg. Med. Chem. 19*, 3750-3756.
[191] Hoffman, A. S. (**2012**) Hydrogels for biomedical applications, *Advanced Drug Delivery Reviews 64*, 18-23.
[192] Mezger, T. G. (**2006**) The rheology handbook: for users of rotational and oscillatory rheometers, *Vincentz Network GmbH & Co KG*.

.